DISSERTATION

TRACKING REACTIVE NITROGEN PLUMES AND THEIR EVOLUTION FROM SATELLITE OBSERVATIONS

Submitted by

Madison J. Shogrin

Department of Atmospheric Science

In partial fulfillment of the requirements

For the Degree of Doctor of Philosophy

Colorado State University

Fort Collins, Colorado

Spring 2026

Doctoral Committee:

Advisor: Emily Fischer

Vivienne Payne
Jeffrey Pierce
Steven Miller
Sheryl Magzamen

ABSTRACT

TRACKING REACTIVE NITROGEN PLUMES AND THEIR EVOLUTION FROM SATELLITE OBSERVATIONS

Satellite remote sensing offers near-continuous global coverage and plays a critical role in addressing observational gaps for many atmospheric trace gases. Reactive nitrogen species are critical in atmospheric chemistry because they drive tropospheric ozone (O_3) formation and contribute to the production of secondary aerosols. This dissertation presents novel satellite-based observations and methodologies for analyzing reactive nitrogen trace gases, specifically Peroxyacyl Nitrates (PANs) and ammonia (NH_3). We investigate the variability in intercontinental air pollution transport of PANs and the chemical evolution of NH_3 within smoke plumes. We introduce new approaches for using multiple satellite products together to isolate enhancements in plumes and extracting information on chemical evolution in the context of highly variable background concentrations. We further develop these methods by implementing a machine learning–based retrieval framework for trace gas observations of NH_3.

In Chapter 2, we leverage global satellite observations of PANs from the Cross-track Infrared Sounder (CrIS) on the Suomi National Polar-orbiting Partnership (S-NPP) satellite to evaluate the seasonal and interannual variations of intercontinental transport in the Northern Hemisphere between 2016 and 2022. We find that April and July are dominant months for transpacific transport of PANs and summer months (June, July and August) are dominant months for transatlantic transport. There is significant interannual variability over the study period during the months where the intercontinental transport of PANs is largest. We use CrIS PANs

combined with NO_2 from the Ozone Monitoring Instrument (OMI) to explore changes to the intercontinental transport of PANs associated with major decreases in precursor emissions in response to COVID-19. CrIS observations indicate statistically meaningful decreases in PANs over regions in both the Pacific and the Atlantic Ocean basins compared to Pre-COVID years 2016-2019; the changes in PANs are smaller than the changes in NO_2. May 2020 CrIS observations indicate PANs (OMI NO_2) declined over the NW Pacific by ~11% (~33%), NE Pacific by ~8% (~15%), USA-Atlantic outflow region by ~4% (~4%), and Atlantic by ~11% (~11%). The largest change in PANs occurred over the NW Pacific in February 2020, where PANs (OMI NO_2) decreased ~16% (~42%) compared to Pre-COVID years. We also use a chemical transport model to simulate PAN changes in response to the pandemic emissions changes and find the model is consistent with the observed changes in PANs. Our observations suggest the values of PANs over the ocean basins have not fully rebounded to Pre-COVID values which is consistent with the trend in tropospheric column NO_2.

Biomass burning is one of the largest natural sources of gas-phase ammonia (NH_3) to the atmosphere which has implications for secondary aerosol formation. In Chapter 3, we use measurements of NH_3 and carbon monoxide (CO) from the Cross-track Infrared Sounder (CrIS) aboard the Suomi-National Polar orbiting Partnership (S-NPP) satellite to investigate the emissions and evolution of NH_3 in smoke plumes. Our analysis focuses on wildfires over the western United States during summer 2018, a period that coincides with the Western Wildfire Experiment for Cloud Chemistry, Aerosol Absorption, and Nitrogen (WE-CAN) aircraft campaign. We present approaches for 1) separating NH_3 enhancements from transient biomass burning events from persistent agricultural hotspots from satellite platforms, and 2) correcting height bias in the standard NH_3 retrievals to improve applicability to lofted wildfire smoke. We

calculate normalized excess mixing ratios (NEMR) of NH_3 with respect to CO within smoke plumes to characterize evolution as the fires evolve in time and the plumes are transported downwind. The calculated NEMRs are also used to track the temporal evolution of NH_3 enhancements near fire centroids over 25 days of burning and to examine their relationship with fire radiative power (FRP). We find higher distributions of NEMRs to be associated with lower FRPs, where median NEMRs > 0.10 are always associated with median FRPs < 50 MW. We incorporate data from the Cloud-Aerosol Lidar and Infrared Pathfinder Satellite Observation (CALIPSO) platform, which enables further interpretation of the height of a smoke plume.

Chapter 4 presents the first application of a machine learning (ML)-based retrieval approach to extend optimal estimation (OE)-based retrievals of NH_3 and CO from CrIS in the context of wildfire smoke analysis. Using this novel dataset, we examine NH_3 enhancements relative to CO in smoke plumes during active fire years, demonstrating the method's ability to capture the evolution of NH_3 within individual plumes. Comparative analysis during the 2018 wildfire season shows qualitative agreement between ML- and OE-based retrievals in isolating smoke plumes and assessing plume characteristics, including NH_3 NEMRs and their decay with plume age. Case studies, such as the Pole Creek Fire in Utah, illustrate this alignment across key metrics. These findings demonstrate the capability of ML-enhanced CrIS retrievals to assess chemical evolution in wildfire smoke, and this ML-based approach offers the potential for significantly more data to be processed and used.

ACKNOWLEDGEMENTS

I would like to thank my advisor, Dr. Emily Fischer, for her unwavering support and mentorship over the past five years. Thank you for always believing in me and challenging me to become a better scientist. I am also deeply grateful to Dr. Vivienne Payne, who has been my mentor since my undergraduate internship. That first internship experience was instrumental in my decision to pursue graduate school, and I feel so fortunate to have had your guidance throughout this entire journey. I am forever grateful to have been shaped into a scientist by these two incredible women—you have taught me so much about what it truly means to be a scientist. I would also like to thank my committee members, Drs. Jeff Pierce, Steve Miller, and Sheryl Magzamen, for their continued support and guidance. Your feedback and encouragement have been invaluable in strengthening the research presented in this dissertation and helping me reach this milestone. I also want to thank Drs. Susan Kulawik and Kazu Miyazaki, who have been integral collaborators during the last five years and on the work presented here.

Grad school is hard, and I would not have made it through without the support from my friends and family. To my friends from CSU, thank you for making my time here unforgettable – Ann Casey Hughes, Marc Alessi, Charlie Connolley, Daniel Hueholt, Nicole June, Olivia Sablan, Emily Lill, Samantha Greeney, Andrew Feder, Megan Franke, Siânin Spur, Ellie Driscoll, and so many others. Thank you to the past and present members of the Fischer Group – especially Kimberley Corwin, who has been my go-to person for science and life advise for these last five years. And to my friends beyond Atmospheric Science, Eleni Vlachos, Madi Martin, and Ali Quinn, and so many others, thank you for always being there for me.

Finally, I want to thank my family for their endless love and encouragement. Thank you for supporting me as I follow my dreams; I truly would not be here without you. To my mom, thank you for always being there and being willing to talk through anything and everything with me. To my dad, thank you for inspiring me to reach this point. It feels especially meaningful to be defending my Ph.D. exactly 28 years to the day after you earned yours—coming full circle in a way that makes this milestone even more special. And to Andrey Marsavin, thank you for always being there for me in every way and for always making me smile.

The following acknowledgements are adapted from the individual chapters of this dissertation. The research presented in Chapter 2 was funded under NASA award no. 80NSSC20K0947 and the research presented in Chapters 3 and 4 was funded under NASA JPL subcontract no. 1693705. Part of this work was carried out at the Jet Propulsion Laboratory, California Institute of Technology, under a contract with the National Aeronautics and Space Administration (80NM0018D0004). We also acknowledge the support of the NASA Atmospheric Composition: Aura Science Team Program (19-AURAST19-0044), Earth Science U.S. Participating Investigator program (22-EUSPI22-0005), ACMAP (22-ACMAP22-0013), and the NASA TROPESS project. We would like to thank Dr. Lok Lamsal for answering questions regarding the NO_2 satellite data and Dr. Karen Cady-Pereira for her contributions to the NH_3 satellite observations.

DEDICATION

I would like to dedicate this dissertation to my corgi Beans (aka Winston). For eleven years, he has been by my side – sitting at my feet during those first-year 2020 Zoom classes and still resting at my toes as I write these final words.

TABLE OF CONTENTS

CHAPTER 1

INTRODUCTION[1]

1.1 INTRODUCTION TO REACTIVE NITROGEN

Reactive nitrogen (N_r), defined as all biologically active, chemically reactive, and radiatively important nitrogen-containing species excluding N_2 and N_2O, encompasses trace gases such as nitrogen oxides ($NO_x = NO + NO_2$), ammonia (NH_3), and peroxyacyl nitrates (PANs; $RC(O)OONO_2$). N_r species enter the atmosphere from direct emissions, and they can also be formed secondarily; anthropogenic activities (e.g., fossil fuel combustion, fertilizer application) and natural processes (e.g., biomass burning, biological nitrogen fixation) are both major sources. Once they are emitted, N_r species can cause a cascade of impacts in the atmosphere and throughout the earth system (Canfield et al., 2010; L. Y. Stein & Klotz, 2016). N_r sources to the atmosphere are largely dominated by emission of NO_x and NH_3 (Galloway et al., 2004). NO_x is rapidly converted to NO_y ($NO_y = NO_x$ + other oxidized N_r) species in the atmosphere, such as PANs or HNO_3 in less than 1 day (Galloway et al., 2004; Seinfeld, 2016). Similarly, NH_3 is rapidly converted to NH_4^+ and removed from the atmosphere through wet and dry deposition, as well as dissolution in precipitation, typically within a few hours to days (Fowler et al., 2013; Schlesinger & Hartley, 1992). N_r compounds are central to tropospheric ozone (O_3) production (D. A. Jaffe & Wigder, 2012) and contribute significantly to secondary aerosol formation (P. Lin et al., 2016; Trentmann et al., 2005). Additionally, N_r deposition to ecosystems drives eutrophication of aquatic systems and soil acidification (Bouwman et al., 1997; X. Chen et al., 2014, p. 201; Pan et al., 2024; Prenni et al., 2014). Over recent decades,

[1] Adapted from the introductions of the three journal articles presented in Chapters 2-4 of this dissertation. See individual chapters for full citations.

anthropogenic N_r emissions have increased substantially, leading to elevated atmospheric concentrations of many reactive nitrogen species (Erisman et al., 2011; E. Li et al., 2024).

1.1.1 Peroxyacyl Nitrates (PANs)

PANs are photochemical pollutants that form in tandem with O_3 under polluted conditions, resulting from the oxidation of non-methane volatile organic compounds (NMVOCs) in the presence of nitrogen oxides ($NOx = NO + NO_2$) (Fischer et al., 2014; Gaffney et al., 1986; Roberts, 2007; Singh et al., 1986, p. 198; Singh & Hanst, 1981). PANs refer to a chemical family that includes propionyl peroxy nitrate (PPN; $CH_3CH_2C(O)OONO_2$), methacryloyl peroxy nitrate (MPAN; $CH_2C(CH_3)C(O)OONO_2$), among others, in addition to peroxy acetyl nitrate (PAN; $CH_3C(O)O_2NO_2$). PAN is the predominant compound in the PANs family, comprising 75–90% of total PANs, followed by PPN (Fischer et al., 2014). As such, most research has focused on PAN. PANs are known to negatively affect human and plant health, functioning as both respiratory and ocular irritants (Altshuller, 1978; Smith, 1965; Vyskocil et al., 1998). Due to their formation via photochemical processes, PANs are frequently used as indicators of atmospheric photochemistry (Rappenglück et al., 2003). Their formation and thermal decomposition influence O_3 levels (Steiner et al., 2010), and PAN concentrations are often utilized to assess regional photochemical activity (Sillman & West, 2009) and the success of O_3 control policies (Gaffney et al., 1989). Notably, PANs exhibit a non-linear response to precursor emissions, and over broad regions of the atmosphere, they can be more responsive to changes in NMVOC emissions than NO_x emissions (Fischer et al., 2014).

The lifetime of PANs against thermal decomposition is highly dependent on the NO/NO_2 ratio and air mass temperature. In the warmer lower troposphere, PANs are relatively short-lived,

with lifetimes on the order of hours at around 20°C but have lifetimes greater than 1 month at cooler temperatures characteristic of the mid troposphere (Honrath et al., 1996). When air masses containing PANs move from polluted continental areas into more remote regions, PANs act as key reservoirs for NO_x, enabling the sustained formation of O_3 in environments where NO_x is scarce (Fischer et al., 2011, 2014; Mena-Carrasco et al., 2009; Zaveri, 2003). Without the influence of PAN chemistry, the global distribution of O_3, particularly in remote regions, would differ substantially (Jiang et al., 2016). Over the past few decades, urban areas across the globe have seen major shifts in NO_x and VOC emissions due to regulatory and socioeconomic changes (Borbon et al., 2013; Georgoulias et al., 2019; Hilboll et al., 2013; Schneider et al., 2015), underscoring the importance of long-term monitoring of photochemically active species in these regions. Although there have been in situ PAN measurements taken in some urban locations and during specific seasons (Gaffney, 1999; Gaffney et al., 1986; G. Lee et al., 2008; J.-B. Lee et al., 2013; Qiu et al., 2019, 2020, 2021; S. X. Wang et al., 2014; G. Zhang et al., 2015; H. Zhang et al., 2014), such observations remain limited with respect to spatiotemporal coverage.

1.1.2 Ammonia (NH_3)

Ammonia (NH_3) plays a critical role in the global nitrogen cycle, influencing air and water quality, ecosystem health, and the climate. NH_3 combines with sulfates and nitric acid to form secondary inorganic aerosols (Behera & Sharma, 2010; Yokelson et al., 2009). These aerosols can make up ~50% of the fine particulate matter ($PM_{2.5}$) mass in many locations (Seinfeld, 2016) and this can have both direct and indirect effects on Earth's radiation budget (Myhre et al., 2013; Paulot et al., 2017), human health (Pope et al., 2009), visibility (Hand et al., 2020), and ecosystem degradation (Benedict et al., 2013; Pan et al., 2021). NH_3 is not directly regulated in the United States, and over the last decade it has become increasingly scrutinized for

its wide-ranging impacts on environmental quality (Shephard & Cady-Pereira, 2015). More than 80% of NH_3 emissions originate from agriculture in the US (T. Butler et al., 2016; Reis et al., 2009), however biomass burning serves as an important natural source (Kopáček & Posch, 2011).

1.2 Sources of Reactive Nitrogen

1.2.1 Urban and Anthropogenic Sources

Over the past two decades, anthropogenic emissions of NO_x and NMVOCs have varied significantly across urbanized regions around the globe (Bauwens et al., 2022; Duncan et al., 2016b; Lamsal et al., 2013, 2015a; Van Der A et al., 2008; Warneke et al., 2012; B. Zhao et al., 2013). As urban populations continue to expand and industrial activity intensifies, cities have become major sources of trace gases that contribute to regional and global changes in atmospheric composition. Emissions from densely populated metropolitan areas play a disproportionate role in shaping the global oxidant budget due to both the volume of pollutants emitted and the efficiency with which they are exported from the boundary layer into the free troposphere (Babatola, 2018; Lawrence et al., 2007; Lelieveld et al., 2015; Pochanart et al., 2004). These exported pollutants can lead to downwind formation of O_3 and particulate matter and influence the global distribution of reactive nitrogen, particularly through reservoir species such as PANs, which enable long-range transport of NO_x. Emissions from megacities impact the global distribution of reactive nitrogen through PANs (T. M. Butler & Lawrence, 2009; Stock et al., 2013), as pollution can be injected into the free troposphere and be transported downwind (Lawrence et al., 2007). Understanding the spatiotemporal distribution of PANs over and

downwind of major population centers is essential for characterizing the global distribution of reactive nitrogen.

1.2.2 Wildfires

Biomass burning is a significant source of greenhouse gases, trace gases, and particulate matter that have global implications for air quality and climate. Wildfires serve as a significant source of N_r to the atmosphere and are the dominant natural terrestrial source of NH_3 (Bouwman et al., 1997; Paulot et al., 2017) and smoke plumes often contain a significant fraction of PANs from rapid formation (J. F. Juncosa Calahorrano, Lindaas, et al., 2021a). N_r emissions from natural biomass burning originate from the nitrogen content within the fuel itself. Natural fires typically do not reach temperatures high enough to produce thermal NO_x through the reaction of atmospheric N_2 and O_2, so fuel-bound nitrogen is the dominant source (Roberts et al., 2020). The amount of reactive nitrogen released therefore varies with fuel type, as different fuel materials contain different levels of nitrogen. Fuel moisture and arrangement can also affect the combustion characteristics and relative emissions of reactive nitrogen compounds (L.-W. A. Chen et al., 2010; Lindaas, Pollack, Garofalo, et al., 2021a; McAllister, 2019). In general, higher nitrogen content in biomass leads to greater emissions of reactive nitrogen species upon combustion (Burling et al., 2011; Coggon et al., 2016a; Kuhlbusch et al., 1991; Stockwell et al., 2014). Combustion efficiency is particularly important in determining the variability of NH_3 and NO_x emissions (Roberts et al., 2020), whereas pyrolysis temperature can be an important driver of variability in the relative emission of other N_r species (i.e., HCN, HNCO, and HONO). Smoldering combustion tends to emit more NH_3 and NO_x whereas flaming combustion tends to emit more NO_x and HONO (Burling et al., 2011; Goode et al., 1999; McMeeking et al., 2009; Roberts et al., 2010; Yokelson et al., 1996, 1997). Flaming combustion is more associated with

higher burning temperatures and greater oxidation of small N-compounds and smoldering combustion is generally more associated with lower burning temperatures and less oxidation. However, the relationship between combustion efficiency and NH_3 emissions can be highly non-linear (Tomsche et al., 2023).

Biomass burning is the primary natural terrestrial source of atmospheric NH_3 (Bouwman et al., 1997; Paulot et al., 2017). Wildfire potential and risk is expected to rise on the global scale, particularly in regions already prone to wildfires (Liu et al., 2010), which will likely drive an increase in NH_3 emissions (Bray et al., 2018, 2021). A significant portion of the reactive nitrogen released in wildfire smoke is in the form of NH_3, it is the third most abundant reactive nitrogen compound emitted in smoke (Lindaas, Pollack, Calahorrano, et al., 2021a; Roberts et al., 2020). As smoke plumes move downwind, the deposited NH_3 serves as a major source of reactive nitrogen to ecosystems that are sensitive to nitrogen inputs (Benedict et al., 2013, 2017; X. Chen et al., 2014; Karlsson et al., 2013; Pan et al., 2021; Prenni et al., 2014).

Over recent decades, advances in satellite remote sensing, atmospheric modeling, and in situ measurement techniques have greatly enhanced our understanding of wildfire emissions and their complex impacts. Human-driven changes in land use, combined with a warming climate, have contributed to an increase in the frequency, intensity, and duration of large wildfires, and subsequently their emissions (Bray et al., 2018). These fires not only degrade local air quality, but these smoke plumes can be transported across vast distances, impacting neighboring continents and global atmospheric composition (Baars et al., 2011; Xian et al., 2013). Smoke plumes from Canadian wildfires have been observed to influence the air quality in Europe (Ansmann et al., 2018; Forster et al., 2001a; Q. Zhang et al., 2025) and similarly plumes from

Siberia have been observed to influence the abundances of trace species over North America (Fischer et al., 2011; D. Jaffe, 2004; Jiang et al., 2016; Johnson et al., 2021).

Biomass burning emissions have historically been challenging to characterize due to the episodic and sporadic nature of fires. Ground-based monitoring networks often lack the spatial and temporal coverage needed to capture these dynamic events, and aircraft campaigns provide a valuable snapshot at specific spaces and times. Satellite observations have contributed to wildfire research by providing near-continuous, large-scale views of smoke distribution and composition. The work presented in this dissertation leverages novel satellite data and analysis techniques to observe both the enhancement of species associated with the long-range transport of smoke plumes and the chemical evolution of reactive trace gases within individual plumes. This dissertation focuses on satellite observations of two reactive nitrogen species: NH_3 and PANs.

1.3 POLLUTION TRANSPORT

The intercontinental transport of air pollution has long been a subject of scientific interest due to its significant impacts on regional air quality, background atmospheric composition, and the global distribution of climate and health-relevant pollutants. Emissions from industrial activity, transportation, agriculture, and biomass burning can be lofted into the free troposphere and transported thousands of kilometers downwind, often far from the source region. In the Northern Hemisphere, long-lived reactive nitrogen species such as PAN play a critical role in this transport, contributing to the redistribution of O_3 and reactive nitrogen across continents. For example, emissions from East Asia and North America have been shown to influence O_3 levels across the Pacific and Atlantic, respectively, with increases in tropospheric O_3 over East Asia since 2005 contributing to elevated O_3 levels in western North America (Creilson et al., 2003; Fischer et al., 2010, 2011; Koike, 2003; Y. Lee et al., 2021; Q. Li et al., 2002; Walker et al., 2010; Wolfe et al., 2007). As global development drives increases in anthropogenic activity and changes in emissions, quantifying and understanding the mechanisms and impacts of pollution transport downwind of pollution source regions becomes increasingly critical for both air quality management and climate mitigation efforts.

1.4 SATELLITE OBSERVATIONS

1.4.1 Observations of PANs

PANs are not typically included in routinely measured ground-based air quality networks so there is no long-term record of in situ observations of PANs in most urban locations (LA is an exception; e.g. Pollack et al., 2013), though a few records from mountain tops and remote areas exist (Fiore et al., 2018; Fischer et al., 2010, 2011; Val Martin et al., 2008). Measurements of

PANs have been included in numerous field campaigns, both ground-based and aircraft, providing a snapshot of PANs at specific times and locations (Lindaas et al., 2019), however, these snapshots are inadequate for diagnosing any large-scale or long-term variability in PANs. PANs have absorption features in the thermal infrared that can be readily measured from space-based spectrometers. Satellite observations of PANs are relatively novel and include nadir-viewing observations from the Tropospheric Emission Spectrometer (TES) (Payne et al., 2014) and from meteorological sounders like the Infrared Atmospheric Sounding Interferometer (IASI) (Franco et al., 2018) and the Cross-track Infrared Sounder (CrIS) (Payne et al., 2022). Early space-based studies leveraged observations from TES to capture plumes associated with boreal fire plumes crossing the Pacific (Fischer et al., 2018; Zhu et al., 2015a, 2017). There have been a few space-based studies assessing the distribution of PANs over the Eastern Pacific (Fischer et al., 2018; Zhu et al., 2015a, 2017), crossing the Pacific (Jiang et al., 2016; Zhai et al., 2024), and over East Asia (Stavrakou et al., 2021), though none from a global perspective. Other space-based studies of PANs focus on enhancements associated with fires (Alvarado et al., 2011; Clarisse et al., 2011; J. F. Juncosa Calahorrano, Payne, et al., 2021) and around megacities (M. J. Shogrin et al., 2023, 2024). Chapter 2 builds on this body of work by proving the first global-scale observations of PANs and quantifying the variability in PANs crossing both the North Pacific and North Atlantic Oceans.

The newest observations of PANs measure all PANs species collectively. Members of the PANs family serve similar functions with respect to atmospheric chemistry. The CrIS observations of PANs utilize the spectral feature centered around 790 cm^{-1} (12.7 micrometers). This spectral feature appears in the infrared spectra for all PAN species at essentially the same frequency, so the CrIS measurements report all PANs (i.e., this includes PPN;

$CH_3CH_2C(O)OONO_2$, MPAN; $CH_2C(CH_3)C(O)OONO_2$, etc.) in addition to PAN; $CH_3C(O)O_2NO_2$. In contrast, the TES observations of PAN use the spectral feature centered around 1150 cm^{-1} (8.7 μm), which occurs in the infrared spectra for just PAN. The CrIS PANs product used in this dissertation utilizes an optimal estimation approach to retrieve profiles of volume mixing ratio (VMR), which are then used to calculate free-tropospheric averages. This product will be further described in the methods of Chapter 2.

1.4.2 Satellite Observations of NH_3

NH_3 is notoriously difficult to measure in situ because it is a very "sticky" molecule that has the ability to readily absorb/desorb from inlet and sampling surfaces (Roscioli et al., 2015), making routine fast measurements difficult. Existing ground-based passive sampling networks provide weekly and bi-weekly averages of NH_3 deposition (Puchalski et al., 2016). NH_3 concentrations have a large spatiotemporal variability due to their relatively short lifetime (~hours to 2 days) (Dammers et al., 2019), posing challenges to these averages and these networks are primarily located in North America, Europe, and China (Van Damme et al., 2015), leaving much of the world under sampled.

Satellite observations of NH_3 bridge the gap left by in situ networks by providing nearly continuous measurements across the entire globe. Similarly to PANs, NH_3 has absorption features in the thermal infrared that can be readily measured from space-based spectrometers. The network of satellites producing observations of tropospheric NH_3 has grown in the last decade with nadir-viewing satellite instruments, such as the Tropospheric Emissions Spectrometer (TES) aboard NASA-Aura (Cady-Pereira et al., 2017; Shephard et al., 2011), the Infrared Atmospheric Sounding Interferometer (IASI) instrument aboard the European Space

Agency's MetOp satellite (Clarisse et al., 2023; Luo et al., 2022), and more recently from the CrIS instrument (Shephard and Cady-Periera, 2015). These nadir observations have been used to quantify NH_3 emissions from agricultural practices (Ding et al., 2024), analyze enhancements associated with urban activities (Cady-Pereira et al., 2017; Cao et al., 2022), and examine NH_3 enhancements from wildfires (Adams et al., 2019; Q. Chen et al., 2025). Chapters 2 and 3 build on this body of wildfire-focused research by examining the chemical evolution of NH_3 relative to CO within wildfire smoke plumes, leveraging densely sampled data that now allow for analysis at the footprint scale, something that was previously limited by coarse observational resolution.

This dissertation focuses on NH_3 measurements from the CrIS instrument aboard the Suomi-National Polar orbiting Partnership (S-NPP) satellite. The CrIS NH_3 retrieval utilizes the 650-1095 cm^{-1} (9.14-15.38 μm) range, as the main NH_3 infrared absorbing spectral region is between 960-970 cm^{-1} (Shephard & Cady-Pereira, 2015). CrIS offers enhancements in space-based observations of NH_3 compared to TES and IASI. The across-track scanning swath of the CrIS instrument provides greater spatial coverage compared to TES, and CrIS has ~4 times less spectral noise in the NH_3 spectral region, enabling CrIS to detect smaller NH_3 concentrations compared to IASI (Shephard & Cady-Pereira, 2015; Zavyalov et al., 2013). This product will be further discussed in the methods section of Chapters 2 and 3.

1.6 Overview of Dissertation Chapters and Goals

This dissertation advances our understanding of N_r species in the atmosphere relevant to pollution transport and chemical evolution in smoke. We aim to gain insight into the key drivers of interannual variability of a reservoir species crossing Northern Hemisphere Ocean basins through first-of-its-kind satellite observations. This dissertation also outlines novel methods for analyzing the chemical evolution of a species with variable background concentrations using

satellite observations, and these methods can be applied to a wide range of chemical species. I also present results formal hybrid satellite retrieval approach that proves promising for the future of satellite data processing.

Chapter 2 is adapted from a manuscript published in the *Journal of Geophysical Research: Atmospheres (M. Shogrin et al., 2026)*. In Chapter 2, I quantify the variability in PANs being transported across Northern Hemisphere Ocean basins using new satellite observations. Chapter 2 asks (1) what are the global spatiotemporal patterns of PANs, particularly over the ocean basins and (2) how did COVID-related changes to anthropogenic emissions and extreme fire seasons manifest in PANs over the Northern Hemisphere Ocean basins? This work builds on an arsenal of previous in situ and modeling studies looking at the transpacific transport of PAN (e.g., Bey et al., 2001; Cooper et al., 2004; Heald et al., 2003; Hudman et al., 2004; Kaneyasu et al., 2000; Kotchenruther et al., 2001; Ridley et al., 1990; Walker et al., 2010), adding the first global-scale observations of this species. This work represents a unique contribution to the existing literature on intercontinental PAN transport by providing the first multi-year, multi-season analysis across both the North Atlantic and North Pacific Oceans. My findings demonstrate the importance of anthropogenic and wildfire emissions in modulating the variability of transported PANs.

Chapter 3 is adapted from a manuscript currently under preparation for submission to *Journal of Geophysical Research: Atmospheres.* In Chapter 3, I use CrIS observations to quantify the evolution of NH_3 in wildfire smoke plumes and I outline methods to separate persistent surface-based emissions from transient plumes. Chapter 3 aims to use CrIS observations to (1) identify individual wildfire smoke plumes, (2) isolate smoke from persistent emissions sources, and (3) quantify the evolution of NH_3 in smoke plumes. This analysis builds

on previous work using CrIS to analyze the chemical evolution of PANs in wildfire smoke (Juncosa Calahorrano et al., 2021). We extend the capabilities of the satellite instrument by applying a similar analysis to a more chemically complex species. To our knowledge, the chemical evolution of NH_3 in wildfire smoke plumes has not previously been examined using satellite observations. Additionally, this work attempts to explain and correct a height bias in the NH_3 CrIS retrievals in wildfire smoke. My findings demonstrate the capability of the CrIS instrument in capturing the chemical evolution of a chemically complex species within a wildfire smoke plume and demonstrate our ability to correct biases of an important species in wildfire smoke plumes.

Chapter 4 is adapted from a manuscript in preparation for submission to the *Journal of Geophysical Research: Atmospheres*. In Chapter 4, I present the first application of machine learning-based retrievals of NH_3 and CO in wildfire smoke plumes by building on the methods outlined in Chapter 3. My primary goal in this chapter is to answer the question, (1) what is the potential for machine learning-based satellite retrievals to expand the scope of NH_3 analysis across fire seasons? My findings indicate an excellent agreement between the more traditional optimal estimation retrieval method and the machine learning approach offering a promising future for the application of machine learning based satellite retrievals for applications to wildfire smoke plumes.

Chapter 5 summarizes my findings from each of the previous chapters and emphasizes high-level takeaways from each study. This chapter also outlines a few possible avenues for future research expanding on the analyses presented in this dissertation.

Chapter 2, with Appendix A as supplementary information is currently published:

Shogrin, M., Payne, V. H., Kulawik, S. S., Miyazaki, K., & Fischer, E. V. (2026). Transport of Peroxyacyl Nitrates (PANs) across Northern Hemisphere Ocean basins from satellite observations. Journal of Geophysical Research: Atmospheres, 131, e2025JD044872. **https://doi.org/10.1029/2025JD044872**

Chapter 3, with Appendix B as supplementary information is in preparation for submission as:

Shogrin, Madison, Payne, V., Kulawik, S., Iacono, M., Corwin, K., Juncosa Calahorrano, J., Pollack, I., Lindaas, J., Campos, T., Flocke, F., Fischer, E., (2025). Evolution of Ammonia (NH_3) in wildfire smoke plumes during the summer of 2018 from space. *In preparation for submission to Earth's Future*

Chapter 4, with Appendix C as supplementary information is in preparation for submission as:

Shogrin, Madison, Payne, V., Werner, F., Kulawik, S., Fischer, E., (2025). Evolution of Ammonia (NH_3) in wildfire smoke plumes from space: insights from a novel machine learning retrieval approach. *In preparation for submission to JGR: Atmospheres*

Chapter 5 summarizes this work with overarching conclusions and looks ahead to some future avenues for this research.

CHAPTER 2

TRANSPORT OF PEROXYACYL NITRATES (PANS) ACROSS NORTHEN HEMISPHERE OCEAN BASINS FROM SATELLITE OBSERVATIONS[2]

2.1 INTRODUCTION

PANs provide a thermally-unstable reservoir for nitrogen oxide radicals that allows NO_x radicals to be transported downwind and impact photochemical oxidation processes far from emission sources (Fischer et al., 2014; Gaffney, 1999; Gaffney et al., 1989; Singh & Hanst, 1981; Singh & Salas, 1983). PANs are formed through the photochemical oxidation of NMCOVs in the presence of NO_x. Thermally unstable in the lower troposphere (lifetimes on the order of 1 hour at 20°C), PANs have lifetimes on the order of 1 month at lower temperatures characteristic of the mid-troposphere (Honrath et al., 1996). PANs formed over a polluted continent can be lofted to the free troposphere and can be transported across ocean basins (Bey et al., 2001; M. Lin et al., 2012; Wolfe et al., 2007). PANs species can result in the formation of O_3 downwind, and knowledge of the spatiotemporal distribution of PANs is vital for understanding the global distribution of tropospheric O_3.

The transport of PANs provides a second pathway, in addition to the direct transport of O_3 itself (M. Lin et al., 2012; L. Zhang et al., 2008), for Asian emissions to influence O_3 levels in North America via transport across the Pacific (Cooper & Parrish, 2004; Fischer et al., 2010; D. Jaffe, 2004, p. 200; Walker et al., 2010; Wolfe et al., 2007; Zhai et al., 2024). Rapid economic development in East Asia at the beginning of the 2000s resulted in a large growth of NO_x and NMVOC emissions (Hu et al., 2022; Huang et al., 2013; Zheng et al., 2018), and while

[2]Adapted from Shogrin, M., Payne, V. H., Kulawik, S. S., Miyazaki, K., & Fischer, E. V. (2026). Transport of Peroxyacyl Nitrates (PANs) across Northern Hemisphere Ocean basins from satellite observations. Journal of Geophysical Research: Atmospheres, 131, e2025JD044872. **https://doi.org/10.1029/2025JD044872**

anthropogenic emissions have leveled off in recent years (Itahashi et al., 2022), pollutants emitted from this region have some of the largest global impacts on oxidant distributions due to efficient mechanisms of export and the sheer magnitude of emissions (Babatola, 2018; Bouarar et al., 2017; Lawrence et al., 2007; Lelieveld et al., 2015; Pochanart et al., 2004). PANs dominate the reactive nitrogen (NO_y) ($NO_y = NO_x + HNO_3 + PANs + HNO_4 + N_2O_5$) budget in the Asian pollution outflow to the free troposphere (Cooper & Parrish, 2004; Koike, 2003). East Asian emissions have produced observable episodes of elevated PANs over the west Pacific (Koike, 2003), eastern Pacific (Zhu et al., 2017) and west coast of North America (Fischer et al., 2010, 2011; Walker et al., 2010; Wolfe et al., 2007). The decomposition of PANs along the western coast of North America has been attributed to increased O_3 levels over the continent (Fischer et al., 2010, 2011; Walker et al., 2010). However, the contribution of Asian pollution to regional surface O_3 levels in North America is still uncertain, as chemical transport models struggle to resolve this transport due to numerical plume dissipation (Rastigejev et al., 2010), and in-situ campaigns offer only limited snapshots in time and space. Recent work demonstrates that satellite observations of PAN provide insight into the impact of transported PAN on O_3 levels over North America (Zhai et al., 2024).

Anthropogenic emissions from North America have similarly been attributed to increases in surface O_3 over Europe (Auvray & Bey, 2005; Creilson et al., 2003; Guerova et al., 2006; Huntrieser et al., 2005; Q. Li et al., 2002). However, unlike the Pacific Ocean basin, transport of PANs across the North Atlantic Ocean has received less attention. Exceptions include the Atmospheric Tomography (ATom) campaign (Payne et al., 2022; Thompson et al., 2022). and the Convective Transport of Trace Gases into the Middle and Upper Troposphere over Europe (CONTRACE) field experiment (Huntrieser et al., 2005). North American emissions of NO_x

have leveled off and began to decrease over the last decades (Duncan et al., 2016a; Jiang et al., 2022; Lamsal et al., 2015b). PANs are an important source of NO_x for the North Atlantic marine boundary layer (Fischer et al., 2014) and PANs account for a considerable share of the total NO_y in the Atlantic upper troposphere (Talbot et al., 1999).

Several key factors influence the variability of observed PANs crossing Northern Hemisphere (NH) ocean basins, including variability in anthropogenic NO_x emissions, biomass burning, synoptic-scale atmospheric flow patterns, and temperature. Variability in biomass burning over boreal forests in Northern Eurasia and North America contributes to the variability in PANs crossing NH ocean basins (Zhu et al., 2015b). Spring and summer fires in Northern Eurasia contribute to elevated PAN over the western USA (Fischer et al., 2010), and Canadian wildfires transport pollutants across the Atlantic into Europe (Forster et al., 2001b; Vaughan et al., 2018). The efficiency of intercontinental transport is modulated by large-scale atmospheric teleconnection patterns, like the Pacific-North American Pattern (PNA) and the North Atlantic Oscillation (NAO). These modes of variability are defined by anomalies in sea-level pressure that influence the strength of air moving between continents. The positive phases are characterized by enhanced westerly flow that can enhance the intercontinental transport of pollutants (Creilson et al., 2003; Lang et al., 2008). Thermal decomposition is the primary sink for PANs, so the lifetime of PANs is strongly linked to air mass temperature. Colder temperatures can extend the lifetime of PANs and enable transport over further distances. Conversely, warmer temperatures accelerate thermal degradation, reducing the potential for large-scale transport.

Variability in the concentrations of PANs is also a function of spatiotemporal trends in precursor emissions (Fischer et al., 2014). While emissions trends have been variable over both

the Eurasian and North American continents in the recent decades, the abrupt halt of commercial activities during the early stages of the COVID-19 pandemic in 2020 reduced global and regional NO_x, carbon dioxide (CO_2), and other trace gases associated with urban activity (Bauwens et al., 2020; Miyazaki, Bowman, Sekiya, Jiang, et al., 2020; Odekanle et al., 2022; Venter et al., 2020). Emissions reductions had variable impacts on secondary species, like PANs and O_3, whose response was more complex (Stavrakou et al., 2021). Shogrin et al. (2024) examines the response of PANs to these reductions over a subset of megacities; here we expand that analysis by exploring changes in the intercontinental transport patterns of PANs during this period.

Numerous in-situ ground-based and aircraft campaigns have focused on tracking reactive nitrogen species crossing the ocean basins, but satellite observations offer the opportunity to provide a fuller picture of the intercontinental pollution transport. PANs have absorption features in the thermal infrared that can be measured from satellite-based spectrometers. Space-based observations of PAN are relatively new and include nadir-viewing observations from the Tropospheric Emission Spectrometer (TES) (Payne et al., 2014) and from meteorological sounders like the Infrared Atmospheric Sounding Interferometer (IASI) (Franco et al., 2018) and CrIS (Payne et al., 2022). Early space-based studies leveraged observations from TES to capture plumes associated with boreal fire plumes crossing the Pacific (Fischer et al., 2018; Zhu et al., 2015b, 2017). There have been a few space-based studies assessing the distribution of PANs over the Eastern Pacific (Fischer et al., 2018; Payne et al., 2017; Zhu et al., 2015b), crossing the Pacific (Jiang et al., 2016; Zhai et al., 2024), and over East Asia (Stavrakou et al., 2021), though none from a global perspective. Other space-based studies of PANs focus on enhancements associated with fires (Alvarado et al., 2011; Clarisse et al., 2011; J. F. Juncosa Calahorrano, Payne, et al., 2021) and around megacities (M. J. Shogrin et al., 2023, 2024). Here we leverage

novel global CrIS observations of PANs between 2016-2022 to present the seasonality, global distribution, and interannual variability of the species in the context of variations in anthropogenic NO_x emissions, biomass burning, teleconnection patterns, and temperature.

2.2 METHODS

2.2.2 CrIS Observations

We use observations of free tropospheric PANs and from the CrIS instrument, a nadir viewing Fourier transform spectroradiometer currently flying on the S-NPP satellite. S-NPP flies in a sun-synchronous orbit with a mean local daytime overpass time of 13:30. The CrIS instrument measures radiances in three spectral bands: 660–1095 cm^{-1} (long-wave), 1210–1750 cm^{-1} (mid-wave) and 2155–2550 cm^{-1} (shortwave). The full-spectral-resolution radiances are supplied on a 0.625 cm^{-1} spectral grid. CrIS instruments are also currently flying on the JPSS-1 and JPSS-2 satellite platforms.

The CrIS PANs dataset used here was produced under the NASA Tropospheric Ozone and Precursors from Earth System Sounding (TROPESS) project (K. W. Bowman, 2023). The dataset consists of single footprint retrievals that used the NASA CrIS full spectral resolution (FSR) v2 L1B dataset (Revercomb & Strow, 2018). More detailed information on the CrIS PANs retrieval algorithm and S-NPP-CrIS validation against aircraft observations can be found in Payne et al., (2022). The CrIS PANs product validation efforts suggest a single sounding uncertainty of ~0.08 ppbv that reduces with averaging to an approximate lower limit of 0.05 ppbv, demonstrating the ability of CrIS to capture variation in the "background" PANs over remote regions, notably over the ocean (Payne et al., 2022). The sensitivity of the retrievals peaks in the free troposphere (~680 hPa) and decreases near the surface. This analysis uses the column average PANs volume mixing ratio (VMR) between 825 and 215 hPa. CrIS retrievals of

PANs have roughly 1 degree of freedom for signal (DOF), so this product does not include information about the vertical distribution of PANs in the atmosphere. Thus, throughout the paper, given the focus on intercontinental transport over the Pacific and Atlantic Oceans, we refer to PANs in the free troposphere or column. The spectral feature utilized for CrIS PANs retrieval is centered at 790 cm^{-1}, which is an infrared feature that appears in the spectra of all PANs at essentially the same frequency. CrIS measurements therefore include all PANs species in addition to PAN, though PAN is typically the most dominant species (Roberts, 2007). While the CrIS retrieval captures total PANs (including PAN, PPN, MPAN, etc), we expect that the majority of PANs will be in the form of PAN based on observational constraints. Over the Pacific in spring and in urban influenced areas, available in situ observations indicate that PPN is the next most abundant PAN, but the ratio between PPN and PAN is typically 0.1 - 0.15 (Roberts et al., 2004; G. Zhang et al., 2015). PANs in the Atlantic outflow during summer are likely influenced by isoprene chemistry, and thus the PANs measurements during this time represent a mixture of PAN, PPN and MPAN. Prior in situ observations in this region indicate that MPAN can be ~25% of PAN abundances (Roberts et al., 2007).

We use a subsampled batch of S-NPP CrIS PANs observations between January 2016 and December 2022, yielding between 3000-4000 observations per day globally (K. W. Bowman, 2023). Data are missing over all locations between April and August 2019. In late March 2019, there was a failure of the Side 1 electronics for the midwave spectral band of SNPP-CrIS and TROPESS processing was halted at this time. A switch was made over to the Side 2 electronics at the end of June 2019. TROPESS processing was resumed in August 2019. Our analysis focuses on the spatiotemporal variability of CrIS PANs globally and in four

Northern Hemisphere Ocean regions to analyze changes in intercontinental transport in response to changes in precursor species.

2.2.3 Satellite Observations of Tropospheric NO_2

We use Level 3 (L3) tropospheric NO_2 column measurements from the NASA Aura Ozone Monitoring Instrument (OMI) and the European Space Agency's TROPOspheric Monitoring instrument (TROPOMI) aboard Sentinel-5P satellite across 2016-2022 to contextualize PANs observations amid emissions reductions in 2020. OMI NO_2 is primarily used to identify months with anomalously low tropospheric NO_2 columns associated with the COVID-19 pandemic (2020), relative to the pre-COVID period (2016–2019). We use the Quality Assurance for Essential Climate Variables (QA4ECV) L3 OMI NO_2 product described in Boersma et al. (2018). TROPOMI NO_2 tropospheric column data is primarily used to examine post-COVID values in relation to the 2020 anomalies. We use the TM5-MP-DOMINO operational version of the monthly mean L3 data from January 2019 and December 2022. The TROPOMI NO_2 OMI NO_2 retrievals apply similar approaches within the QA4ECV project (Boersma et al., 2018; Van Geffen et al., 2022), giving consistent reprocessing for NO_2 among instruments (van Geffen et al., 2022). However, it would not be expected that the values would be the same given differences in instrumentation, orbit altitude, and retrieval algorithm inputs (van Geffen et al., 2022). Both OMI and TROPOMI NO_2 tropospheric column data are provided on a global 0.125° x 0.125° grid and can be found on the TEMIS database.

2.2.4 Model Sensitivity Studies

To quantify the relative contributions of different NO_x sources to the interannual variability of PANs observed by CrIS, we conducted sensitivity simulations using the state-of-

the-art global chemical transport model MIROC-CHASER (Chemical Atmospheric General Circulation Model for Interdisciplinary Research on Climate for Study of Atmospheric Environment and Radiative forcing) (Sekiya et al., 2018; Sudo et al., 2002; Watanabe et al., 2011). The model simulates detailed chemical and physical processes in both the troposphere and stratosphere, encompassing 92 chemical species and 262 reactions, with a horizontal resolution of 1.125°. We employ this model to isolate NO_x changes only.

As input for the simulations, we used NO_x emissions constrained by satellite-based NO_2 retrievals from OMI, provided by the Tropospheric Chemistry Reanalysis version 2 (TCR-2; Miyazaki, Bowman, Sekiya, Eskes, et al., 2020). We compared simulations using 2020 emissions with those using business-as-usual (BAU) emissions, which were constructed for 2020 based on 2015–2019 emission trends (Miyazaki et al., 2021), to estimate the response of PANs to the NO_x emission reductions associated with the COVID-19 lockdowns. Reasonable agreement between simulated PAN and observed PAN from aircraft and TES satellite observations are shown in Miyazaki, Bowman, Sekiya, Eskes, et al. (2020).

2.3 Results and Discussion

2.3.1 Global Distribution of PANs

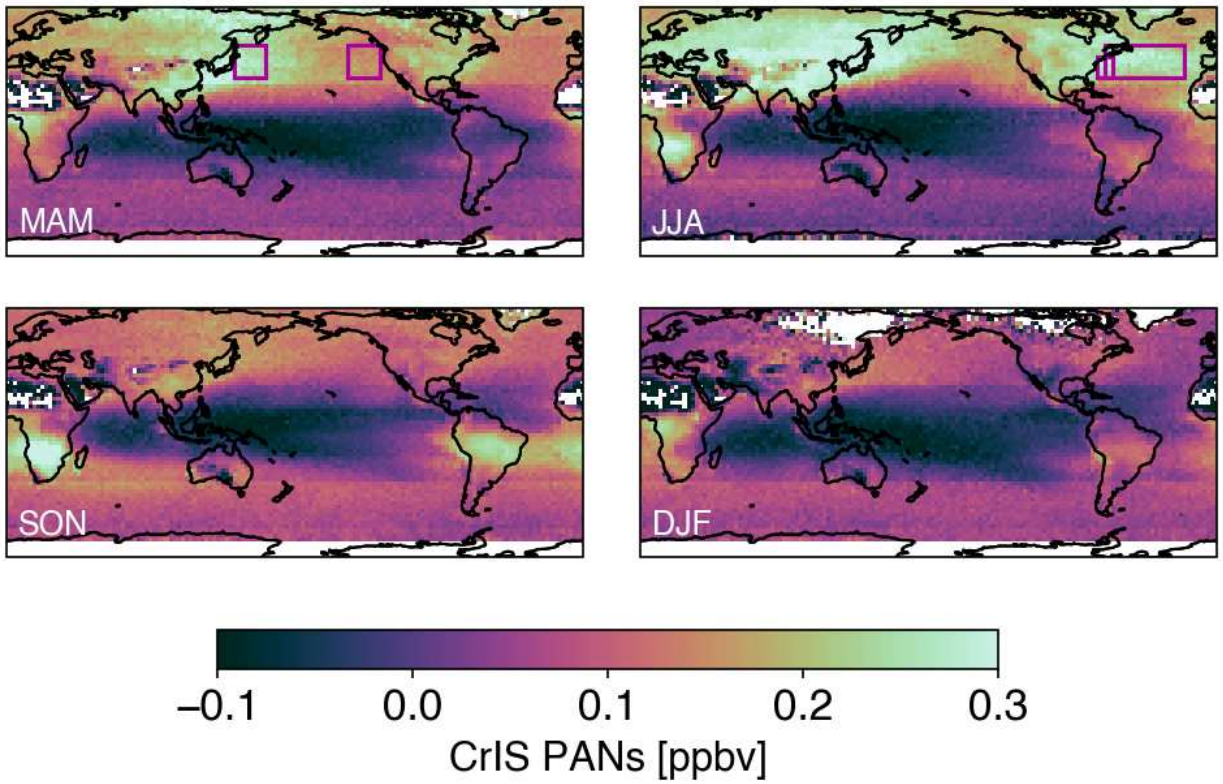

Figure 2.1: CrIS observations of seasonal mean free tropospheric PANs from January 2016 - December 2022 separated by season. Data has been gridded into 2.5° x 2.5° boxes. Colored boxes denote spatial extents of ocean basin boxes.

The seasonal maximum in the northern hemisphere (NH) free tropospheric PANs observed by CrIS is NH spring (March through May) and summer (June through August; Figure 2.1). A springtime maximum has been observed at high altitude mountain top observatories (Fiore et al., 2018) and at remote FTIR stations (Mahieu et al., 2021). The springtime maximum previously observed at the surface in the NH has been attributed to photochemical activity and longer lifetime of PANs against thermal decomposition (Brice et al., 1988; Fischer et al., 2014; Penkett & Brice, 1986). Model simulations suggest this consistent springtime maximum in the lower atmosphere (< 6 km) is largely a feature of remote regions (Fischer et al., 2014), but models fail to capture its magnitude (Mahieu et al., 2021). Seasonal peaks in spring, summer or

fall have been observed over urban areas (J.-B. Lee et al., 2013; M. J. Shogrin et al., 2024). Elevated free tropospheric PANs, such as observed by CrIS, are primarily attributable to air masses transported from the polluted boundary layer rather than the formation of PANs in the free troposphere (Pandey Deolal et al., 2013).

CrIS measurements indicate elevated PANs over the Arctic during spring and summer months. This pattern has been historically attributed to the transport of pollution from the midlatitudes (Moxim et al., 1996). Additionally, fires in northern latitudes further contribute to elevated concentrations of PANs over the northern polar region (Fischer et al., 2014, 2018).

NH free tropospheric PANs continue to stay elevated through the summer months and reach a seasonal peak over many regions (Figure 2.1; JJA panel). Photochemical activity stays high following the spring, but warmer summer temperatures lead to more thermal decomposition of PANs (Brice et al., 1988). Northern hemisphere wildfire activity enhances concentrations of PANs through the summer (Fischer et al., 2018). It is likely that PANs are higher aloft (e.g., Figures 2 and 3 in Fischer et al. (2014)) as temperature in the free troposphere stays cool despite warmer lower tropospheric temperatures in the summer months. As described in Section 2.2, our observations receive most of their signal from the free troposphere. Lightning and convection also support higher production of PANs aloft in summer months (Hudman et al., 2007).

The Southern Hemisphere (SH) also exhibits a seasonal peak in PAN concentrations during the austral spring months (September through November). Evidence of transcontinental transport from Africa to Australia and from South America to Africa is observed in CrIS data (Figure 2.1c; SON panel). Previous studies attribute the observed springtime PAN maximum between 0-35°S to seasonal biomass burning over central Africa, convective transport of polluted boundary layer air to the upper troposphere, and lightning (Moore & Remedios, 2010; Moxim &

Levy, 2000). Where data is available, urban centers in the SH typically experience a seasonal peak in the austral spring months (Shogrin et al., 2024). PANs remain elevated over many NH urban areas through the autumn months (Figure 2.1c; SON) and some areas experience a secondary seasonal maximum at this time (J.-B. Lee et al., 2013; M. J. Shogrin et al., 2024).

The SH background PANs continue to be elevated during the austral summer months (December-February), though to a lesser degree than the elevated summertime levels of the NH. Elevated PANs over central Africa are aligned in time and location with seasonal burning (Duncan et al., 2003). Elevated wintertime PANs are observed over northern hemisphere urban regions (Figure 2.1d; DJF).

2.3.2 Seasonal Variability of PANs over Northen Hemisphere Ocean Basins

We focus our remaining analysis on four sectors (boxes in Figure 2.1) across the Northern Hemisphere Ocean basins. These locations were selected to represent areas impacted by the import and export of PANs between the Eurasian and North American continents. Small shifts in the positions of these boxes do not impact our conclusions. The Northwestern Pacific box (NW Pacific) is located just east of Japan to capture the PANs exported from the Eurasian continent and into the Pacific. The Northeastern Pacific box (NE Pacific) aims to represent pollutant plumes that cross the Pacific and could enter North America. The boxes over the Pacific basin were informed by Zhai et al. (2024). The box located off the coast of North America (USA-Atlantic outflow) aims to capture PANs outflowing from North America. The final box is located across the Atlantic basin (Atlantic) and aims to capture PANs entering Europe.

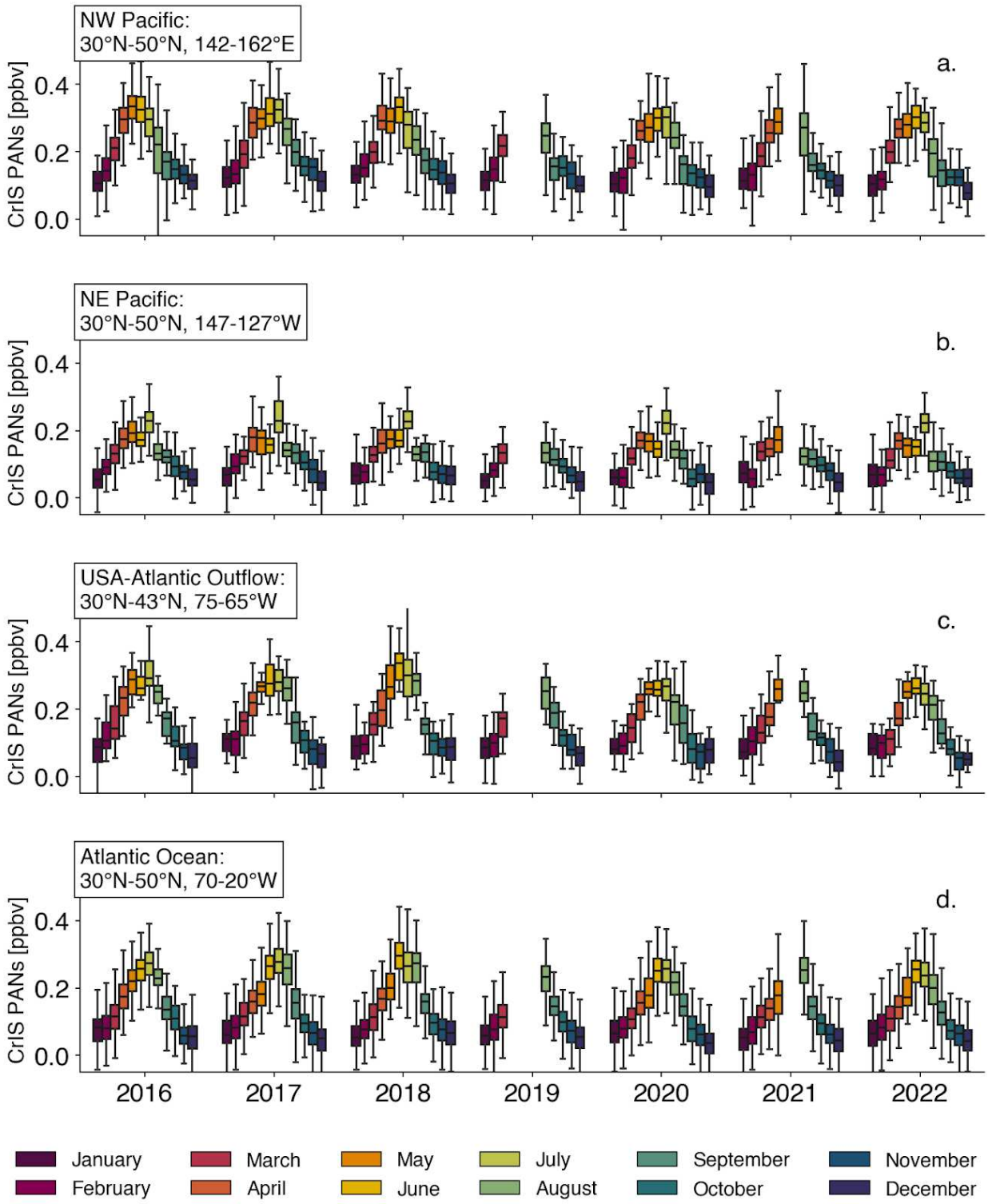

Figure 2.2: Monthly mean distribution of gridded CrIS tropospheric mean PANs in the regional boxes shown in Figure 2.1. The extent of the boxes represents the 25th and 75th percentile, the median is shown by the line in the center, and the extents of the whiskers represent the 5th and 95th percentile. Outliers in data are not shown.

Figure 2.2 displays the distribution of PANs over each ocean basin box considered. The NH spring and summer months are the seasonal maxima for PANs over the Pacific (Fig 2.2a and 2.2b), displaying the importance of this time for transpacific transport of PANs. In the NW Pacific free troposphere, the seasonal maximum occurs in April or May (Figure 2.2a), with PAN levels remaining elevated (> 0.2 ppbv) through August. This region serves as a key pathway for pollutant outflow from East Asia, and there is an extensive literature base on this topic (Fischer et al., 2010, 2011; Hudman et al., 2004; Kotchenruther et al., 2001; Ridley et al., 1990; Roberts et al., 2004; Wolfe et al., 2007; Zhai et al., 2024; Zhu et al., 2015b). Emissions from East Asia have some of the largest impacts on global pollutant burden, in part due to the efficient mechanisms of pollutant outflow (Babatola, 2018; Lelieveld et al., 2015; Pochanart et al., 2004). Through most of the year, cold dry air from Siberia converges with warm Pacific air resulting in active cyclogenesis over coastal East Asia (Pochanart et al., 2004; Stohl, 2001). Cyclones move off the coast and travel to higher altitudes and latitudes, creating an efficient pathway for rapid export of pollutants eastward over the Pacific (Pochanart et al., 2004). Deep convection becomes more important in the summer months and facilitates continental outflow over the ocean (Pochanart et al., 2004).

The CrIS observations confirm that the summer months in the NH are also a crucial time for transcontinental transport, marked by seasonal maxima in mean PANs over both the Atlantic and Pacific regions (Figure 2.2). In the free troposphere, PANs concentrations over the Atlantic reach their seasonal maximum in June, remaining elevated through September. During the rest of the year (September through May), PANs fall below 0.2 ppbv. Previous measurements in the Atlantic troposphere have identified similar seasonal patterns in NO_y species (Val Martin et al.,

2008). The seasonal maximum in PANs over the NW Pacific continues through July (Figure 2.2a).

Over the NE Pacific, concentrations of free tropospheric PANs peak in July, consistent with findings from TES data (Zhu et al., 2015). Additionally, our measurements indicate some interannual variability in the concentrations of PANs over both ocean basins, discussed in the following subsection.

2.3.3 Interannual Variability of PANs

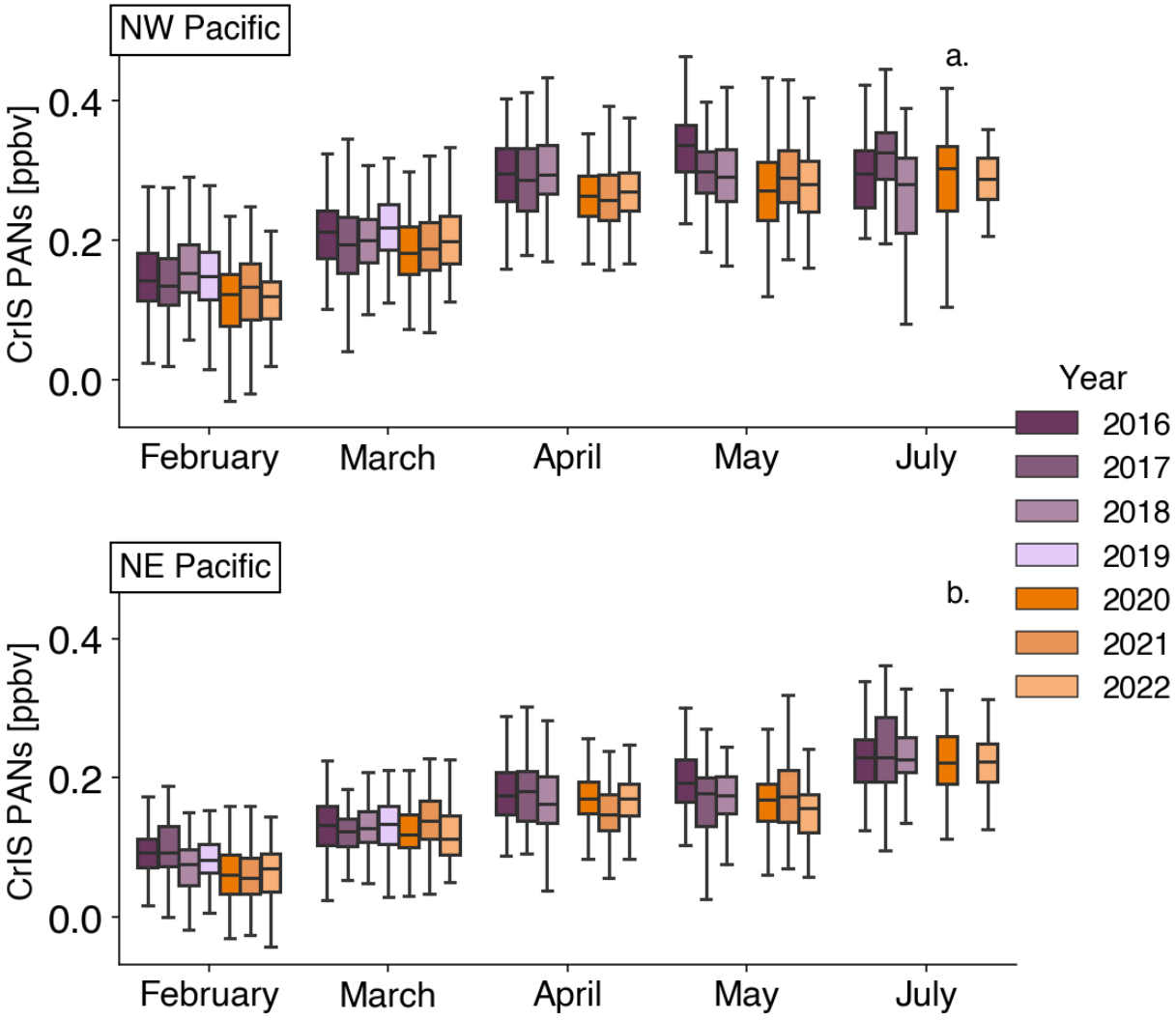

Figure 2.3: CrIS PANs gridded monthly mean distribution within the respective boxes denoted in Figure 2.1. The months shown are the months with interannual variability over the Pacific Ocean basin boxes. Hue difference represents pre-COVID and post-COVID time periods. The extent of the boxes represents the 25th and 75th percentile, the median is shown by the line in the center, and the extents of the whiskers represent the 5th and 95th percentile. Outliers in data are not shown.

In this section, we explore a subset of months with higher levels of interannual variability across both ocean basins and the primary factors influencing this variability. February through May experienced the most interannual variability through the seven years of CrIS data over the Pacific. The distribution of monthly averaged CrIS free tropospheric PANs over both Pacific boxes for these four months are presented in Figure 2.3. The most notable deviation across all

months occurs in 2020 (dark orange in Fig 2.3) in association with precursor emissions changes in response to COVID-19. Decreases in PANs over East China have been documented from IASI observations in both February and May of 2020 in comparison to 2019 values (Stavrakou et al., 2021). Across every month over the NW Pacific, there is a step down in mean free tropospheric PANs during 2020 compared to the distributions of previous years. To evaluate interannual differences in CrIS PANs, we conducted a one-way ANOVA with post hoc pairwise comparisons across three defined periods: pre-COVID, COVID, and post-COVID for all four ocean boxes. This analysis assesses whether the distributions of PANs values differ significantly between periods and individual years independent of each temporal grouping. From this pairwise ANOVA test, 2020 over the NW Pacific is statistically different from all pre-COVID years, but post-COVID years (2021-2022) are not statistically different from 2020. The same is true over the NE Pacific, except that 2018 does not differ from 2020-2022 (See Appendix A tables for Pacific p-values values). Concentrations do not rebound back to pre-pandemic levels through 2022. The NE Pacific follows a similar pattern; however, the changes are less significant here than over the NW Pacific. We quantify the uncertainty in median values using a nonparametric percentile bootstrapping approach for February-May. We estimate the 95% confidence intervals for monthly medians range 0.043 - 0.35 ppbv and the widths of the confidence intervals range 0.013 - 0.043 ppbv in the Pacific. In the NW Pacific, interannual median differences (0.003 - 0.054 ppbv) exceed the widths of the confidence intervals, consistent with results from the ANOVA testing, indicating statistically and practically meaningful interannual differences. Interannual changes in the NE Pacific are smaller (0.002 - 0.033 ppbv) than those in the NW and are generally comparable to the confidence interval widths. While our ANOVA testing indicates significant changes in some years (particularly in 2020), the magnitude of these changes relative

to the measurement uncertainty is small, so interannual variations in the NE Pacific should be interpreted cautiously.

The response in PANs to changes in precursor species is highly location-dependent given the complexity of PANs chemistry and the non-linear response of PAN to changes in precursors. For example, the concentration of PANs over urban Beijing, China, increased significantly in February 2020 (Qiu et al., 2020; M. J. Shogrin et al., 2024) and this has been attributed to alterations in precursor emissions as well as anomalous meteorological conditions that favored enhanced photochemical activity (Qiu et al., 2020). The concentration of PANs over Tokyo, Japan did not experience a significant change as emissions in Tokyo during the lockdown period (April 2020) did not change significantly compared to pre-lockdown levels (Shogrin et al., 2024). PANs and O_3 experienced similar directional responses to COVID-related emission reductions over many megacities (Shogrin et al., 2024). Despite localized increases or lack of changes, several studies report a net decrease in O_3 during 2020 (Miyazaki et al., 2021; Ziemke et al., 2022) and O_3 did not recover to pre-COVID levels as of 2021 (Ziemke et al., 2022). Figure 2.3 suggests the concentrations of PANs also do not recover to 2019 levels over either Pacific box across these months.

Air mass temperature impacts the spatiotemporal abundances of PANs as the lifetime of PAN predominantly depends on thermal decomposition. To probe this potential source of variability, we analyze 2 m air temperature, 850 hPa air temperature, and 500 hPa air temperature for February-May over both Pacific boxes using MERRA-2 Reanalysis monthly mean product (Global Modeling and Assimilation Office (GMAO), 2015). We find that temperature fluctuations between the years were likely not a dominant factor in PAN variability over either Pacific boxes, as temperatures were either unchanged or changed in a direction that

would dampen changes to PANs. For example, decreases in PANs during May 2020 over both NW and NE Pacific boxes were accompanied by lower 500 hPa temperatures, which would increase the lifetime of PANs.

CO distributions across the two ocean boxes between February and May do not follow a similar pattern to PANs (see Appendix A Figure A1.1). VIIRS active fire counts and VIIRS fire radiative power (FRP) over East Asia (land east of 110°E) show no significant correlation with PANs over the Pacific boxes during these months, suggesting that biomass burning did not drive the observed variability in early spring. For instance, both April and May 2020 experienced elevated CO over this area (Appendix A Figure A1.1) which may have masked declines in PANs driven by reductions in anthropogenic NO_x emissions. Distributions of PANs and CO more closely align in summer months, especially in July, when enhanced fire activity is often observed over Siberia. This is consistent with previous findings that the variability of PANs over the Pacific in summer is sensitive to biomass burning emissions.

The Pacific-North American Pattern is a large-scale teleconnection pattern with two modes characterized by pressure oscillations around the Aleutian islands and North American Southwest. The positive phase of the PNA features enhanced westerly flow across the Pacific and can be associated with more efficient pollution transport from the Eurasian continent (Feng et al., 2016; Lang et al., 2008). Median PANs in March over the NW Pacific had a significant positive correlation with PNA index value (Pearson's $r = 0.78$; $p = 0.03$), so March NW Pacific PAN variability was likely partially driven by variability in the PNA. Correlations with the PNA during other months over the NW Pacific were not significant (February: $r = -0.50$; $p = 0.25$; April: $r = 0.18$; $p = 0.69$; May: $r = -0.37$; $p = 0.41$) and there were no significant correlations

over the NE Pacific. The phase of the PNA also has implications for the fate of PANs over the North American continent, as the phase of the PNA can alter temperature.

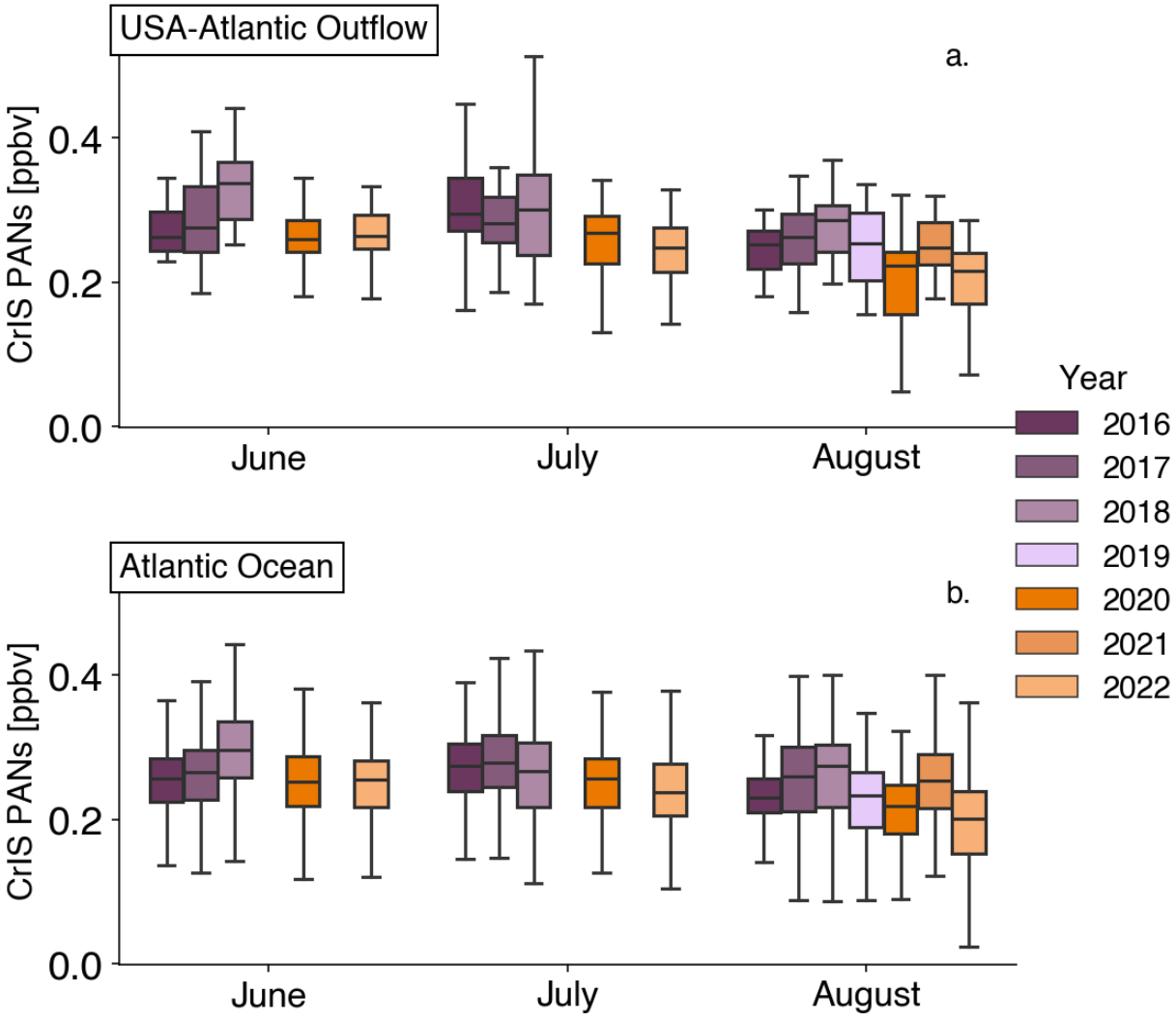

Figure 2.4: CrIS PANs gridded monthly mean distribution in respective latitude/longitude boxes shown in Figure 2.1. The months shown are months with interannual variability in the Atlantic Ocean basin boxes in Figure 2.2. Hue difference represents pre-COVID and post-COVID time periods. The extent of the boxes represents the 25th and 75th percentile, the median is shown by the line in the center, and the extents of the whiskers represent the 5th and 95th percentile. Outliers in data are not shown.

The seasonal maximum for PANs crossing the Atlantic Ocean occurs during the NH summer months, June through August and these are also the months that CrIS detects the most Atlantic interannual variability (Figure 4). Over both the Atlantic Ocean and USA-Atlantic outflow region, the concentration of PANs have a clear increase between 2016-2018 in June and a stark decrease in 2020, with no rebound in 2022. P-values for statistics across all years can be found in Appendix A. Across all months, there is a statistically meaningful difference between pre-pandemic and post-pandemic years over both Atlantic boxes (t-test: USA-Atlantic outflow; $p = 5.4e\text{-}9$, Atlantic Ocean $p = 1.7e\text{-}30$). CO abundances over these Atlantic boxes follow a very similar pattern to PANs (see Appendix A Figure A1.3) in July and August, so interannual variability in the influence of North American biomass burning on these regions of the atmosphere is likely a key driver in the interannual variability in PANs during these months. Applying a bootstrapping approach to June-August, the 95% confidence intervals for monthly medians range 0.18 to 0.334 ppbv and the widths of the confidence intervals from 0.012 - 0.074 ppbv. In the USA-Atlantic Outflow box, interannual median differences are generally comparable (0.002 - 0.044 ppbv) to the widths of the CIs, suggesting some year-to-year differences may be meaningful, but overall interannual variations are modest relative to the uncertainty. In the larger Atlantic Ocean box, the interannual differences are slightly larger (0.009-0.046 ppbv), yet still mostly within the CI range, indicating that interannual variations should be interpreted cautiously, particularly for smaller changes.

The North Atlantic Oscillation (NAO) can be an important factor influencing the amount of pollutants transported from North America to Europe. The NAO influences the strength and direction of westerly winds and the location of storm tracks across the North Atlantic. The positive phase of the NAO is characterized by faster and more efficient westerly movement and

is thus associated with increased transport of North American pollutants (Creilson et al., 2003; Guerova et al., 2006). The interannual variability of PANs crossing the Atlantic appear to be influenced by the variability in the NAO. For example, lower values of PANs are observed for all summer months in 2016, and the NAO was in a negative phase at this time. Conversely, elevated values of PANs were observed across the summer months of 2018, and the NAO was in a positive phase at this time, and this period marked the highest NAO index values for the seven years (see Appendix A Figure A1.4). Variability in 2020-2022, however, is not dominated by the NAO, as the magnitude of NAO index values are lower and month-to-month variability of phase is higher compared to the pre-COVID time period. More discussion of the variability over the post-COVID time period is included in the following section.

Interannual fluctuations in temperature were likely a partial driver of variability over the two Atlantic regions. For example, lower median PAN values over both regions in August 2019 and 2020 were accompanied by higher 850 hPa and 500 hPa temperatures (~2K higher). Satellite-derived tropospheric NO_2 columns lacked significant interannual fluctuations over summer months. For example, lower values of PANs in June and August 2020 corresponded to higher tropospheric NO_2 values from both OMI and TROPOMI compared to previous years. However, variability in anthropogenic NO_x emissions over the Atlantic is more apparent during the spring months of 2020 and this will be explored further in the following sections.

2.3.4 COVID-19 Related Observed NO_2 Perturbations

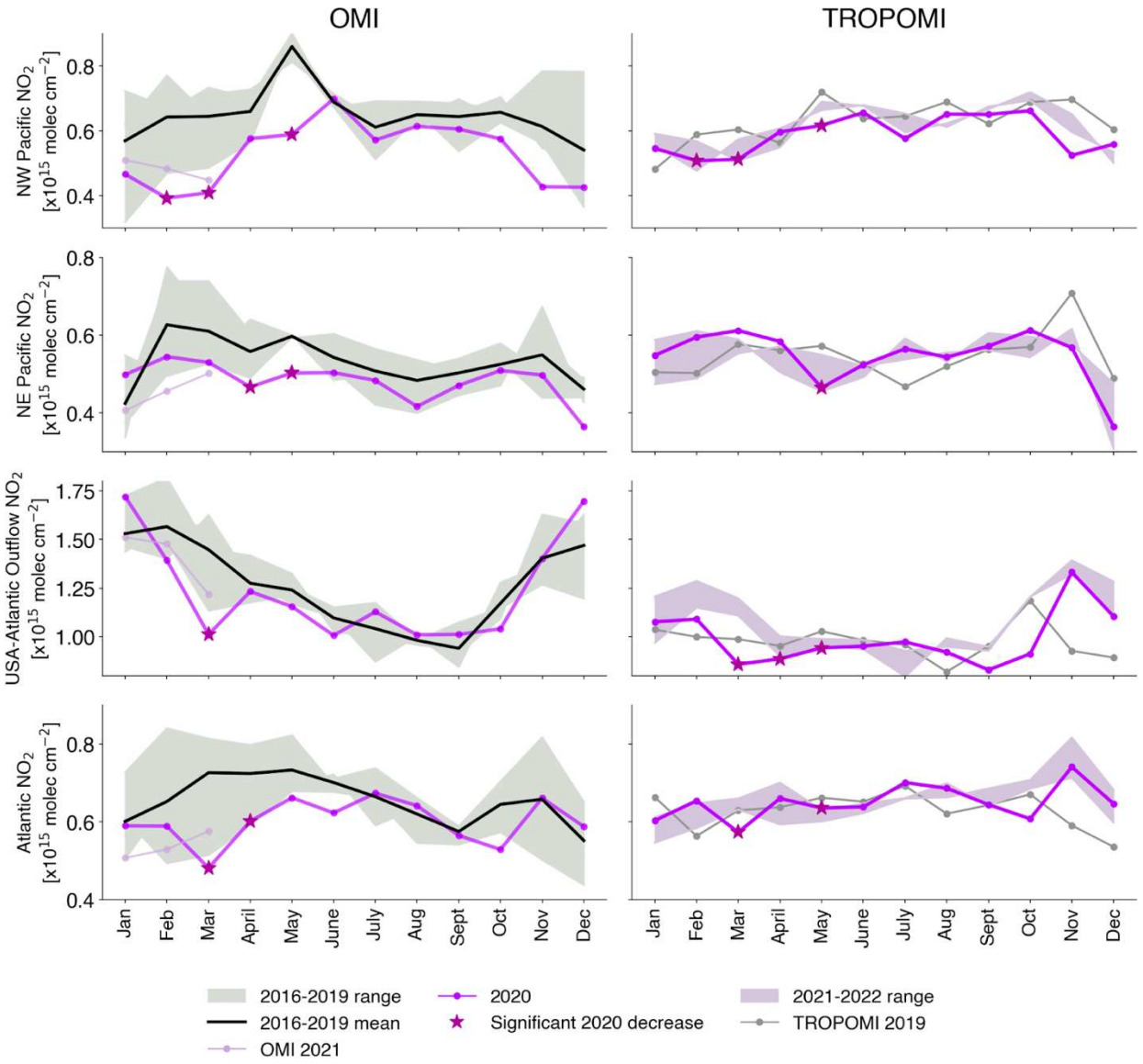

Figure 2.5: Mean tropospheric column NO_2 over the 4 ocean basins (NW Pacific, NE Pacific, USA-Atlantic outflow, Atlantic) from OMI (left) and TROPOMI (right). OMI contains measurements from January 2016 through March 2021 and TROPOMI contains measurements from January 2019 through December 2022. Purple line is 2020, bold black line is the mean of Pre-COVID values, grey shading is the range of Pre-COVID values, light purple line is OMI 2021 values, light purple shading represents the range of post-COVID values, the grey line is 2019. Purple stars on the OMI side represent months where 2020 was >15% less than the mean of pre-COVID values (black line). Purple stars on the TROPOMI side represent spring months of 2020 that were significantly lower than 2019 values.

COVID perturbations to monthly mean NO_2 columns are detectable over all Northern Hemisphere Ocean basin boxes from both OMI and TROPOMI during different months throughout 2020, with the largest changes in the spring months. Changes over the Pacific are more pronounced than those in the Atlantic, where monthly mean OMI (TROPOMI) NO_2 decreased ~16% (~19%) over the NW Pacific and ~11% (11%) over the NW Atlantic in March of 2020 compared to 2019, and monthly mean OMI (TROPOMI) NO_2 decreased ~34% (16%) over the NW Atlantic and ~5% (16%) over the NW Atlantic in May of 2020 compared to 2019. This 2020 perturbation is more apparent when pre-COVID years (2016-2019; bold black line in Fig. 2.5) are grouped; OMI NO_2 decreased by ~37% over the NW Pacific and ~30% over the NW Atlantic during March 2020 compared to prior years. The perturbation to tropospheric column OMI (TROPOMI) NO_2 is greater over the NW Pacific than the NE Pacific, where NO_2 only decreased ~16% (~20%) over the NE in May compared to 2019. Changes in NO_2 column amounts occurred in spring months across both the Atlantic and Pacific, with May experiencing the largest change in the Pacific and March experiencing the largest change in the Atlantic across both OMI and TROPOMI datasets. Monthly mean tropospheric column HCHO remains relatively unchanged between the two periods (not shown), though a strong HCHO signal over the oceans is not expected due to the typically low vertical column abundance of HCHO in remote marine environments.

2.3.5 COVID-19 Related Observed Perturbations to PANs

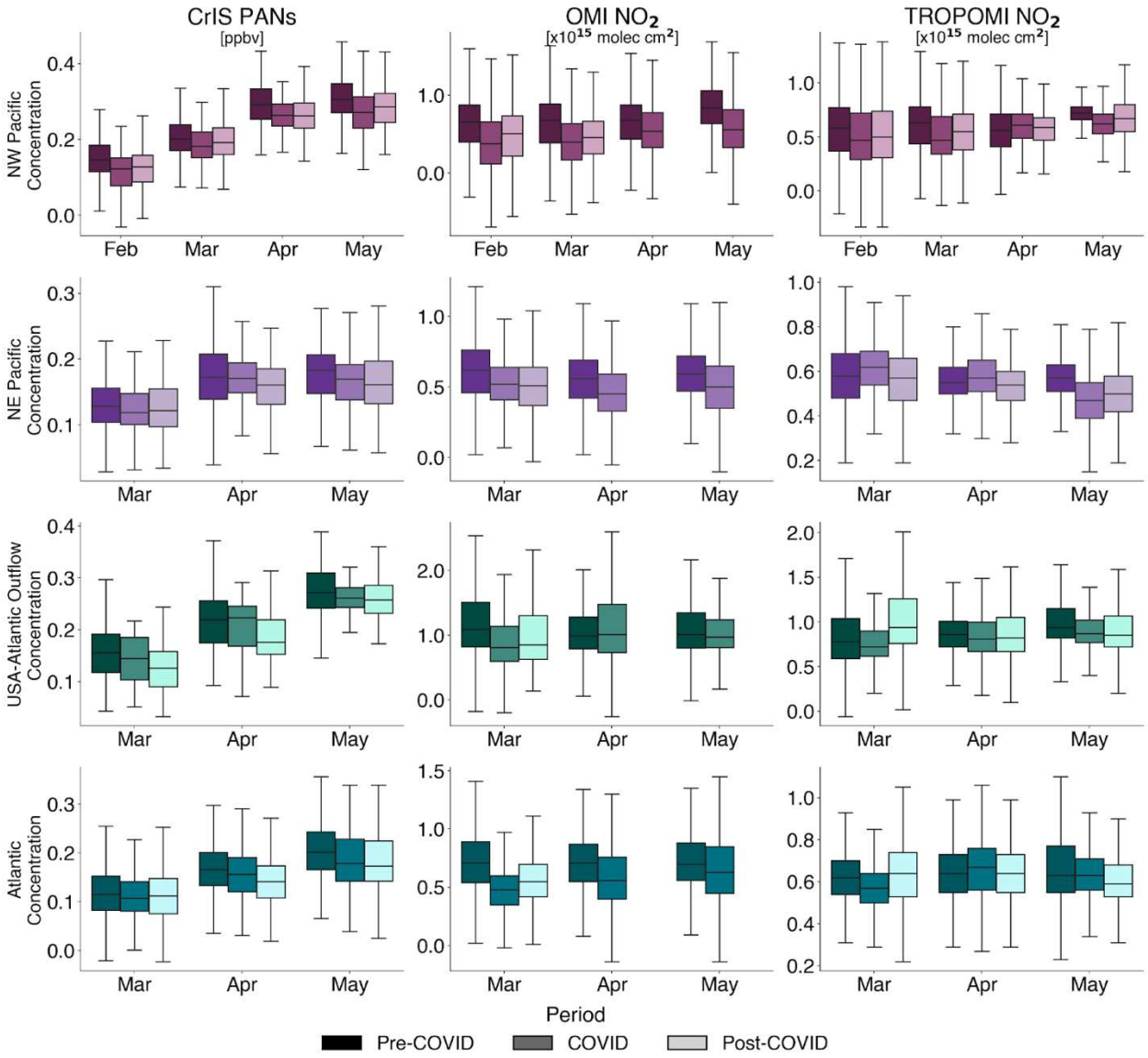

Figure 2.6: CrIS PANs, OMI NO_2, and TROPOMI NO_2 distributions in each ocean basin box for 3 periods: pre-COVID (deep hue; 2016-2019 for CrIS and OMI; 2019 for TROPOMI), COVID (moderate hue; 2020), and post-COVID (pale hue; 2021-2022 for CrIS and TROPOMI; 2021 for OMI). Months included here have been chosen based on NO_2 declines in 2020 from Figure 2.5. Hue differences denote different ocean basin boxes and color value denotes different periods. UNITS: CrIS PANs [ppbv], OMI and TROPOMI NO_2 [x10^{15} molecules cm^{-2}].

Changes to monthly mean free tropospheric PANs are most apparent over the NW Pacific. Changes across February through May in 2020 are statistically different from pre-COVID values (Mann-Whitney u-test, $p < 0.05$). We conduct a Mann-Whitney U-test across the

different time periods to assess whether distributions of PANs in 2020 were significantly different from pre-COVID and post-COVID values. A Mann-Whitney U-test is well-suited for this analysis as it does not assume the underlying distribution is normally distributed. We have used this test to verify similar changes to PANs during COVID in megacities in Shogrin et al. (2024). Free tropospheric PANs were most impacted in February 2020, where PANs decreased ~16% in 2020 compared to pre-COVID years. February 2020 experienced the largest decline in tropospheric column OMI NO_2 in this region, where tropospheric NO_2 decreased by ~42% compared to Pre-COVID years. May 2020 experienced the second largest decline in PANs, (~11%), followed closely by March 2020 (-10%). OMI (TROPOMI) NO_2 declined ~33% (~14%) in May and ~41% (~25%) in March 2020. The change in CrIS PANs in 2020 was small compared to the change in tropospheric column NO_2 from both instruments. Median MERRA-2 500 hPa temperature was higher in March 2020 (~4 K difference) compared to Pre-COVID years, making thermal decomposition more rapid, which could have amplified some of the decline in PANs from perturbed NO_x emissions The distribution of PANs over the NW Pacific in 2020 shifted towards lower values and there were fewer retrievals with PANs mixing ratios over 0.3 ppbv. Post-COVID values of free tropospheric PANs and tropospheric column NO_2 experience a small rebound, however, do not fully bounce back to Pre-COVID values across all months. This incomplete rebound is evident in the median (interquartile range) values when comparing the pre-COVID, COVID, and post-COVID distributions from February-May: PANs: 0.230 (0.17-0.23), 0.218 (0.15-0.27), 0.223 (0.16-0.28) ppbv and OMI NO_2: 0.72 (0.48-0.93), 0.47 (0.24-0.73), 0.48 (0.24-0.71) $x10^{15}$ molecules cm^{-2}. It should be noted that NO_x emissions changes unrelated to COVID-19 could have also contributed to observed changes across the time period.

The NE Pacific experienced a statistically meaningful change in free tropospheric PANs only in May (-8%; p= 0.02), in synch with TROPOMI NO_2 observing decreases, while OMI observes decreases across March through May (OMI includes more years in 'pre-COVID' population). The change in NO_2 from both OMI and TROPOMI over this region was much less than that over the NW Pacific, changing by -16%, -15%, -20% (TROPOMI: 7%, 4%, -18%) in March, April, and May respectively, which is expected given the lower magnitude of values in this region. MERRA-2 500 hPa temperatures over this region were overall lower than pre-COVID years, slowing PAN thermal decomposition in comparison. There were no significant correlations between observed NE Pacific PANs and the PNA index during these months.

NO_2 changes over these months are less pronounced over the Atlantic regions compared to the Pacific. There was a decrease to tropospheric NO_2 observations in March and May, and April to a lesser degree. The most pronounced decrease in OMI NO_2 to both Atlantic regions occurred in March 2020, though this was not accompanied by a statistically meaningful change in CrIS PANs. MERRA-2 500 hPa temperature was higher during 2020 compared to pre-COVID years (~2 K median difference), so this should have contributed to faster PAN thermal decomposition in the regions. No significant correlations between PANs and the NAO index exist during spring months. Significant decreases to free tropospheric PANs occurred over the larger Atlantic region in April (p=0.02) and May (p=0.0). Values of both PANs and NO_2 rebound slightly in the post-COVID period, however, not to the Pre-COVID level. Post-COVID CrIS PANs in April continue to decrease in post-COVID years over both Atlantic boxes despite TROPOMI NO_2 remaining relatively unchanged between periods over the outflow region and slightly decreased over the Atlantic region. The incomplete rebound is evident in the median (interquartile range) values when comparing pre-COVID, COVID, and post-COVID for March-

May: PANs: 0.157 (0.11-0.20), 0.148 (0.11-0.19), 0.143 (0.11-0.18) ppbv and OMI NO_2: 0.71 (0.55-0.88), 0.55 (0.39-0.73), 0.55 (0.43-0.70) x10^{15} molecules cm^{-2}. A summary of PANs changes across ocean basins is shown in Table 2.1.

Summary Table of Interannual Variability of PANs Across Four Ocean Basins

	W Pacific	E Pacific	W Atlantic	Larger Atlantic
Climate patterns				
PNA	Strong positive correlation in March ($r = 0.78$). Other months were not significantly impacted	No significant correlation in any months	–	–
NAO	–	–	Positive NAO phase correlates with higher PANs and negative phase correlates with lower PANs during summer months	
500 hPa Temp 850 hPa Temp	Higher in March 2020; could have reduced PAN lifetime and contributed to lower observed PANs	Lower in May 2020; could dampen the impact of anthropogenic emissions changes	Higher in March 2020, lower in April and May 2020	No major changes
Biomass Burning Proxies				
VIIRS fire Hotspots	Positive relationship between the number of fire hotspots in East Asia and PANs over the Pacific PANs in July		Positive relationship between the number of fire hotspots over North America and PANs in summer (JJA)	
CrIS CO	Positive relationship with CO and PANs; strongest in July		Positive relationship between CO and PANs; strongest in JJA	
Anthropogenic Emissions (COVID-19)				
OMI NO_2	Largest observed COVID decrease across all areas in spring (Feb-May) 2020	Largest decrease in April and May 2020	Largest decrease in March 2020	Largest decrease in March and April
TROPOMI NO_2		Largest decrease in May 2020	Largest decrease in March-May 2020	Largest decrease in March and May 2020

Table 2.1. Summary table of the factors influencing the interannual variability of PANs across the four ocean boxes.

2.3.6 Simulated COVID-19 Perturbations

Basin	Month	BAU [pptv]	2020 [pptv]	% change
NW Pacific	April	324.3	311.9	-3.8%
NW Pacific	May	234.5	227.2	-3.1%
NE Pacific	April	140.6	136.1	-3.2%
NE Pacific	May	144.7	141.5	-2.2%
NW Atlantic	April	275.9	260.1	-5.7%
NW Atlantic	May	290.1	272.9	-5.9%
Atlantic	April	213.9	204.1	-4.6%
Atlantic	May	227.4	218.5	-3.9%

Table 2.2: PAN concentrations (in ppt) at 700 hPa over the four ocean regions during April and May 2020 simulated by MIROC-CHASER. The BAU column indicates PAN concentrations under business-as-usual (BAU) NO_x emissions, while the 2020 column shows PAN concentrations based on actual 2020 NO_x emissions. The % change column presents the percent difference between the two values (2020 – BAU).

As a further assessment of the impact of precursor emission changes during the pandemic-induced economic shutdowns on PAN concentrations, we conducted simulations using the global chemical transport model MIROC-CHASER. The simulations conducted here are to isolate the impact of NO_x emissions only. Two emissions scenarios were considered: a "business as usual" (BAU)" case, in which 2020 emissions were projected assuming no Pandemic occurred, and a "2020" scenario, based on actual emissions estimated for 2020 (Miyazaki et al. 2022). By comparing these scenarios, we isolated the response of PANs to reduced NO_x emissions. More detailed analysis of PAN variability in future studies will require accounting for changes in VOC emissions during the lockdown, which remain difficult to quantify globally due to available observational constraints and associated uncertainties.

Table 2.2 summarizes the simulation results. In agreement with satellite observations, PAN concentrations decreased across all ocean regions in both April and May 2020 in response to reduced NOx emissions, and the simulated changes are generally smaller than the observations. The magnitude of the PAN reduction varies by region and month, with larger PAN reductions in April than May, except over the NW Atlantic. The response of PAN was notably greater for PAN than that of O_3 (not shown). Averaged over the four regions, April had a higher magnitude of change than May for PAN (-4.3% vs -3.8%) and the opposite is true for O_3 (-2.5% vs -2.9%). Among the four regions, the NW Atlantic exhibited the largest PAN decrease corresponding to NOx reductions in both months, followed by the NW Pacific in May and the larger Atlantic basin in April. PAN concentrations are higher over the two areas representing continental outflow (i.e., the NW Pacific and NW Atlantic) than the NE Pacific and larger Atlantic basin.

2.4 CONCLUSIONS

We show the first global-scale observations of PANs between 2016-2022. We use CrIS to analyze the spatiotemporal variability of PANs globally, with a focus on Northern Hemisphere Ocean basins. We probe interannual variability of PANs crossing ocean basins in the context of four main factors: variability in temperature, synoptic-scale flow patterns, variability in biomass burning, and changes to anthropogenic NO_x emissions in the context of the COVID-19 pandemic. Different factors are important for the variability in the intercontinental transported PANs at different times.

1. Global background PANs have seasonal maxima in spring months, MAM for the Northern Hemisphere, and SON for the Southern Hemisphere. PANs continue to stay elevated through the respective hemisphere's summer months.

2. There are distinct seasonal cycles of PANs over each Northern Hemisphere Ocean basin area. Spring and summer months are important for the transpacific transport of PANs and summer months are critical for the transatlantic transport of PANs.

3. CrIS observations reveal interannual variability in PANs over each ocean basin, particularly during the respective seasonal maxima. Over the Pacific, this variability is primarily attributed to NOx emissions, while variability over the Atlantic is more strongly influenced by interannual differences in wildfire activity and fluctuations in the NAO index. Year-to-year variations in monthly mean temperatures likely confound the influence of anthropogenic NO_x on PANs across all regions, apart from March 2020—

when anomalously high temperatures may have enhanced the observed decrease in PANs associated with reduced anthropogenic NO_x emissions.

4. Substantial reductions in tropospheric column NO_2 were observed over Northern Hemisphere Ocean basins during spring 2020, coinciding with COVID-19-related economic shutdowns. Both CrIS observations and model simulations show decreases in PANs during this period. The Northwest Pacific exhibited the most pronounced decrease in both PANs and NO_2 from satellite data across multiple months. The Northeast Pacific and North Atlantic basins also experienced notable reductions, particularly in May 2020, though the magnitude was smaller than over the Northwest Pacific. Additionally, PANs over the North Atlantic were also significantly reduced in April, supported by both satellite observations and model simulations. The relative decreases in NO_2 exceeded those in PANs across all basins, reflecting the nonlinear relationship of NO_2 emissions and PAN formation.

In summary, we present the first global observations of PANs, which reveal clear seasonal cycles and complex interannual variability driven by numerous factors. While the satellite observations of PANs do not provide vertically resolved information, models and available aircraft observations suggest that the transport of PANs across these ocean basins occurs primarily in the free troposphere. In order to understand surface level impacts of this pollution transport, further investigation of PANs profiles over the receptor regions would be desirable. In addition, further investigation on the quantitative impacts of biomass burning, temperature, and emissions variability would be valuable, particularly through the use of tagged tracers in chemical transport

models to track the sources and fates of PANs crossing ocean basins. We leave these as challenges for future investigations. This study highlights the ability of CrIS observations to detect variability in PANs crossing the oceans and these observations can further our understanding of pollution transported between continents.

2.5 Data Availability Statement

The Summary Product of the TROPESS CrIS PANs L2 reanalysis stream used in this study are available online through the Goddard Earth Science Division and Information Services Center (NASA GES DISC) (Bowman et al., 2023). Reanalysis data used in the model simulations are also available through the NASA GES DISC (Miyazaki, Bowman, Sekiya, Eskes, et al., 2020). We acknowledge the free use of tropospheric NO2 column data from the OMI (Boersma et al., 2017) and TROPOMI (Van Geffen et al., 2022) sensors from www.temis.nl.

CHAPTER 3

EVOLUTION OF AMMONIA (NH_3) IN WILDFIRE SMOKE PLUMES DURING THE SUMMER OF 2018 FROM SPACE[3]

3.1 INTRODUCTION

Biomass burning is the largest terrestrial source of gas-phase NH_3 to the atmosphere (Bouwman et al., 1997; Paulot et al., 2014). On a global scale, the potential for wildfires is projected to increase, especially in locations that already have a propensity for fire activity (Liu et al., 2010), and increased wildfire activity would lead to an increase in NH_3 emissions from biomass burning (Bray et al., 2018, 2021). NH_3 makes up a large fraction of the emitted reactive nitrogen in smoke (Lindaas, Pollack, Garofalo, et al., 2021a; Roberts et al., 2020). NH_3 in smoke is an important source of reactive nitrogen to sensitive ecosystems as NH_3 deposits from the plume traveling downwind (Benedict et al., 2017; X. Chen et al., 2014; Karlsson et al., 2013; Prenni et al., 2014).

Emissions of reactive nitrogen (N_r), defined as all nitrogen-containing compounds excluding N_2 and N_2O, from biomass burning originate from nitrogen present within the fuel itself. Since natural wildfires generally do not reach high enough temperatures to generate thermal NO_x via the reaction between atmospheric N_2 and O_2, the combustion of fuel-bound nitrogen remains the predominant source of N_r (Roberts et al., 2020). The quantity of N_r released is therefore influenced by the nitrogen content of the biomass, which varies by vegetation type. Additionally, fuel characteristics such as moisture content and structural arrangement impact combustion dynamics and, consequently, the emissions of reactive nitrogen species (L.-W. A.

[3] Adapted from a manuscript in preparation for submission: Shogrin, Madison, Payne, V., Kulawik, S., Pollack, I., Lindaas, J., Campos, T., Fischer, E., (2025). Evolution of Ammonia (NH_3) in wildfire smoke plumes during the summer of 2018 from space. *In preparation for submission*

Chen et al., 2010; Lindaas, Pollack, Garofalo, et al., 2021b; McAllister, 2019). Overall, fuels with higher nitrogen concentrations tend to emit more reactive nitrogen when burned (Burling et al., 2011; Coggon et al., 2016b; Kuhlbusch et al., 1991; Stockwell et al., 2014). The distribution of NH_3 emissions are sensitive to combustion efficiency, with smoldering phases typically emitting more NH_3 than flaming phases (Q. Chen et al., 2025; Lindaas, Pollack, Calahorrano, et al., 2021b; Roberts et al., 2010; Yokelson et al., 1996, 1997). However, the connection between combustion efficiency and NH_3 emissions is often complex and non-linear (Tomsche et al., 2023).

Fires are a major source of NH_3, but their sporadic nature can pose challenges for the existing ground-based passive sampling networks. These networks provide weekly and bi-weekly averaged NH_3 deposition, which provides an excellent baseline of general patterns; it is difficult to extract the source of deposited NH_3. Additionally, these networks are primarily concentrated in North America, Europe, and China (Van Damme et al., 2015), leaving much of the world undersampled giving large uncertainties in the spatiotemporal distribution of reactive nitrogen. Satellite observations of NH_3 bridge this gap by providing nearly continuous measurements close to fires where logistical constraints are larger. Furthermore, there is a lack of information about the vertical distribution of NH_3 in the atmosphere that satellite retrievals cannot yet supplement, so a limited number of in situ aircraft measurements and space-based LiDAR data helps to fill this gap.

We use CrIS observations to analyze the evolution of NH_3 in wildfire smoke plumes during summer 2018. We present a novel approach to isolate in-plume NH_3 from persistent agricultural sources, enabling calculation of a dilution-correction NH_3 enhancement with respect to carbon monoxide (CO) across space and time. Complimentary LiDAR data from the Cloud-

Aerosol Lidar and Infrared Pathfinder Satellite Observation (CALIPSO) platform enables further interpretation of the CrIS NH_3 enhancement by providing information about the vertical distribution of smoke. Our work provides new insights into the NH_3 evolution in smoke plumes and how NH_3-enhancements evolve in time. The methods applied here can be generalized to multiple parameters to advance space-based analysis of plume chemistry.

3.2 METHODS

3.2.1 CrIS Observations

We use daytime observations of tropospheric NH_3 and from the CrIS instrument, a nadir viewing Fourier transform spectroradiometer currently flying on the Suomi-National Polar orbiting Partnership (S-NPP) satellite and on the JPSS satellite systems. S-NPP flies in a sun-synchronous polar orbit with mean local daytime overpasses around 13:30. The CrIS instrument measures radiances in three spectral bands: 660-1095 cm^{-1} (long-wave), 1210-1750 cm^{-1} (mid-wave) and 2155-2550 cm^{-1} (shortwave). Full spectral-resolution radiances are supplied on a 0.625 cm^{-1} spectral grid.

The CrIS NH_3, CO, PANs datasets used here were produced under the NASA Tropospheric Ozone and Precursors from Earth System Sounding (TROPESS) project and were processed to temporally compliment the data from the WE-CAN aircraft campaign (Kulawik & Payne, 2025). This data provides single-pixel S-NPP-CrIS CO, NH_3, O_3, methanol (CH_3OH), temperature, PANs, H_2O, HDO, and methane (CH_4) for July 24, 2018 through September 13, 2018 over the western United States (35°-40°N, 127°-101°N). More detailed information on the CrIS NH_3 retrieval algorithm can be found in (Shephard & Cady-Pereira, 2015) and validation against FTIR measurements in (Dammers et al., 2017) The CrIS CO algorithm is described in Fu et al., (2016) and the validation is demonstrated in (Worden et al., 2022). CrIS is most sensitive

to NH_3 around 850-750 hPa and has on average 1 Degree of Freedom (DOF) for signal, meaning the product lacks information on the vertical distribution of NH_3 in the atmosphere (Shephard & Cady-Pereira, 2015). The sensitivity of CrIS to CO is more widespread, having ~2 DOFs on average and peaking in the mid-to-upper troposphere above ~700 hPa (Fu et al., 2016a). We use a tropospheric average of CO between 908-215 hPa and a lower tropospheric average of NH_3 between 908-510 hPa, slightly different levels were used due to differences in the vertical grid and peak sensitivity of the different retrievals. We use co-located CrIS retrievals of CO to account for dilution when investigating the evolution of NH_3 enhancements in these plumes. In cases where CO alone is insufficient to distinguish individual smoke plumes, particularly under widespread smoke conditions, we leverage CrIS retrievals of PANs to aid in plume isolation, as CrIS is sensitive to PANs in individual smoke plumes (J. F. Juncosa Calahorrano, Payne, et al., 2021).

3.2.2 Calculating NH_3 enhancements over Variable Background

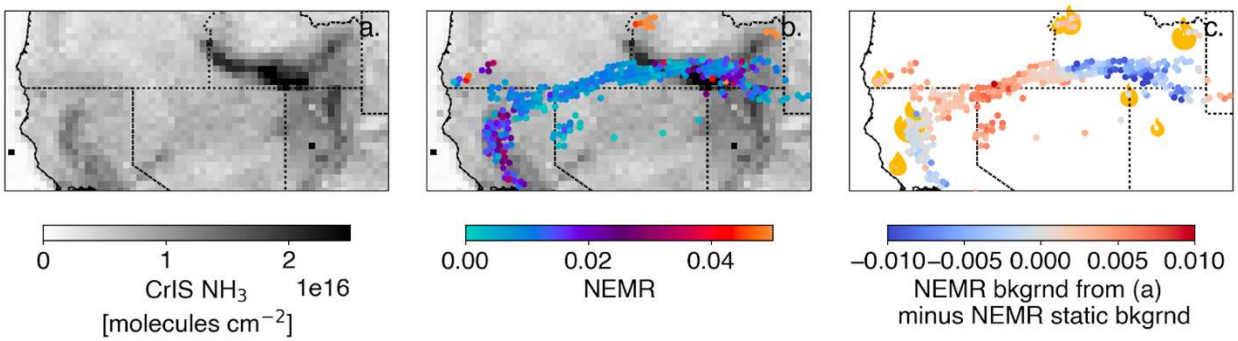

Figure 3.1: (a) Estimated non-smoke background NH_3 from July 24 to September 13, 2018, calculated using standard TROPESS retrievals where tropospheric CO < 100 ppbv, gridded at 0.25° × 0.25°. (b) NH_3 NEMR using variable background values from (a). (c) Error in any NEMR resulting from assuming a static background: the difference between the NEMR calculated using the background NH_3 value from (a) and the NEMR calculated using a static background value of 1e16 molecules cm^{-2} with VIIRS fire hotspots are overlaid as orange icons, sized by relative fire radiative power (FRP).

Wildfire smoke in the western United States frequently intersects regions with substantial agricultural emissions, making it challenging to isolate the contribution of biomass burning to observed NH_3 enhancements. Accurately characterizing the chemical evolution of NH_3 within smoke plumes using satellite observations therefore requires careful separation of fire-related signals from elevated background levels associated with agricultural activity. Figure 3.1a shows an estimate of the "smoke-free" NH_3 background derived from CrIS retrievals over a portion of the western United States. Distinct regions of elevated background NH_3 are evident, particularly in areas linked to intensive agricultural practices, such as the Snake River Valley in Idaho.

The normalized excess mixing ratio (NEMR), or the enhancement ratio, enables comparison of the concentrations of pollutants within a smoke plume while accounting for dilution. The excess mixing ratio in a plume is calculated as the mixing ratio of species X in plume minus the mixing ratio of species X in background air, and it is expected to decrease with plume age due to dilution for primary species (Yokelson et al., 2013). We account for physical dilution of the plume by normalizing by a relatively long-lived primarily emitted tracer species, here CO, giving a normalized excess mixing ratio. This approach enables the investigation of NH_3 evolution within smoke plumes from the perspective of chemical loss within a single plume and comparison between plumes. Thus, a decrease in the NEMR would indicate chemical loss. Here, we calculate the NEMR using the below equation:

$$NEMR = \frac{NH_{3_{retrieval}} - NH_{3_{background}}}{CO_{retrieval} - CO_{background}}$$

Where the $CO_{background}$ = 1.4e18 molecules cm^{-2} and NH_3 background is equal to the value in Figure 3.1a. Background NH_3 is estimated using all retrievals where tropospheric CO is < 100 ppbv (Figure 3.1a; full domain background can be found in Appendix B).

In order to perform this analysis from satellite data, we needed to isolate a given smoke plume. We restrict our analysis to retrievals where CO > 2e18 molecules cm^{-2} and where free tropospheric CrIS acyl peroxy nitrates (PANs) > 3e15 molecules cm^{-2}. This filtering better identifies discrete plumes, where NEMR calculations are most appropriate, from dilute mixed-aged smoke. We also remove a small number of retrievals where retrieved NH_3 < background NH_3 and retrievals located directly above active fires. It is common to use CO to dilution-correct in situ measurements in biomass burning plumes (e.g., Lindaas et al., 2021; Yokelson et al., 2013), but there are few examples of using this approach from space. Juncosa Calahorrano et al., (2021) applies this approach to PANs in plumes using fixed values for background of both CO and PANs. Following this approach, a fixed background value for NH_3 (1e16 molecules cm^{-2}) was initially applied to estimate NH_3 NEMRs from satellite observations and Figure 3.1c shows the difference between this approach and the NEMR shown in Figure 3.1b. However, NH_3 is more spatially heterogeneous than PANs and is directly emitted by agricultural sources. Positive values in Figure 3.1c denote regions where using a static background overestimates the NEMR, as the static value used exceeds the actual background. Negative values in Figure 3.1c denote regions where a static background is too low and the resulting NEMR is an overestimate (i.e., the Snake River Valley, Idaho). Figure 3.1b shows that the NEMR values have a slight increase over Southeastern Idaho (Snake River Valley), likely influenced by the presence of fresh smoke from localized fire activity, as VIIRS active fire detections indicate several small fires in the region (Figure 3.1c).

3.2.3 CrIS Retrieval Height Bias Correction

The thermal infrared radiances observed by CrIS are more sensitive to changes in atmospheric NH_3 aloft than they are to similar changes at the surface. An enhancement in the

NH_3 volume mixing ratio (VMR) within a layer at an altitude of a lofted smoke plume results in a stronger radiance response than to the same increase confined at the surface. The TROPESS retrieval framework assumes a prior shape of the NH_3 profile that peaks near the surface, so retrievals of NH_3 in lofted smoke plumes are often an overestimate of the column-average measurements of NH_3. We report these values as the standard observations.

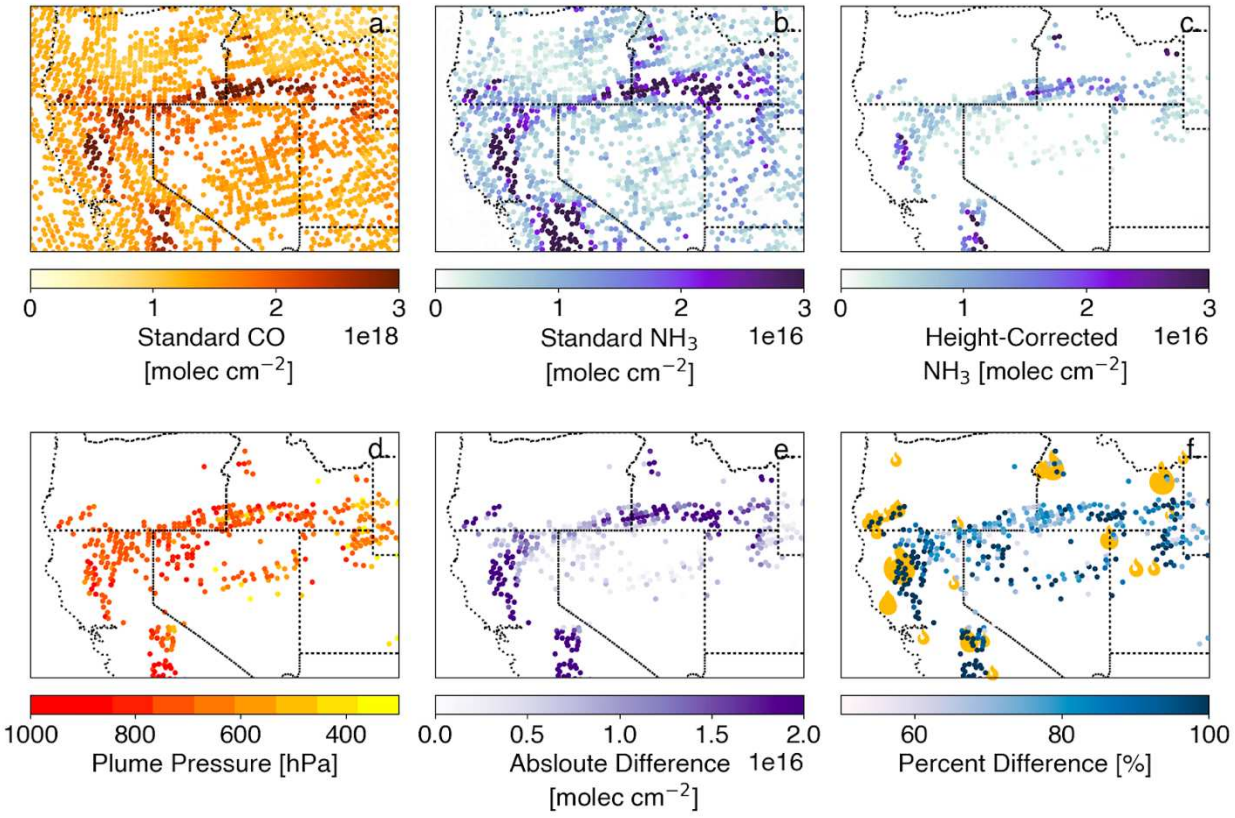

Figure 3.2. (a) CrIS column CO from standard TROPESS files, (b) CrIS column NH_3 from standard TROPESS files, (c) CrIS column NH_3 after a height correction has been applied to the standard retrieval, (d) the estimated plume pressure based on the shape of the CO profile (e) the absolute difference between the standard and height-corrected NH_3 columns (b and c), and (f) the percent difference between the two NH_3 columns with daily VIIRS fire hotspots are overlaid as orange icons, sized by relative fire radiative power (FRP).

We use observations of co-measured CO to estimate and apply a correction factor to the standard NH_3 measurements. The TROPESS CrIS CO retrievals contain up to 2 degrees of freedom for signal in the troposphere, so the CrIS CO products do contain some limited

information about plume altitude. Figure 3.2a shows the CrIS CO total column from the standard TROPESS files. We use the TROPESS CrIS CO profiles to provide an estimate of the NH_3 profile shape within the smoke plume. We performed additional forward model runs for CrIS soundings in fire plumes (designated as XCO > 100 ppbv for the CO column; capturing the most concentrated plumes; Figure 3.2c-f), assuming an NH_3 profile that follows the shape of the CO retrieved profile. We use the following ratio as a correction factor applied to the standard TROPESS NH_3 retrievals within smoke plume:

$$ratio\ plume = \frac{\text{amount } NH_3 \text{ needed to generate observed radiance with CO profile shape}}{\text{amount } NH_3 \text{ needed to generate observed radiance with } NH_3 \text{ profile shape}}$$

Then we multiply the standard TROPESS column NH_3 by this ratio to obtain a height-corrected NH_3 column value. Figure 3.2 displays the standard TROPESS products and height-corrected NH_3 values, plume pressure as calculated during the height correction, and metrics of difference between the two NH_3 columns. We find this height correction reduces the column NH_3 by approximately 50-80% over the most concentrated areas of the plume, excluding the near-fire source and Snake River Valley (Figure 3.2e). The CO provides information on the potential bias in the publicly available standard NH_3 product when applied to lofted smoke plumes.

We apply and note this height-correction in analyses that consider the full plume extent. However, the correction is not applied where analysis relies on retrievals near the fire centroid (e.g., section 3.3.2 *Near-field Evolution of the Fire Centroid across the Wildfire burning cycle*), where strong convective updrafts dominate plume structure. These areas, along with areas associated with major agricultural emissions (i.e., the Snake River Valley, ID) are evident in Figure 3.2f where the height correction implies greater than a 100% change (dark blue) from the standard product. In the near-source regions, rapid vertical transport and highly variable plume

dynamics make this type of correction inappropriate. Areas with strong surface NH_3 signals from agricultural emissions are similarly unsuitable for this correction, which biases the vertical weighting toward aloft NH_3 at the expense of high surface concentrations.

For the analysis in this chapter, we used both height-corrected and uncorrected VMR values for ammonia because this is a novel product which would require reprocessing data; so it is important to document the effect of this correction.

During this reprocessing three additional values were added to the carbon monoxide products to improve the ability to interpret data: a) plume temperature: temperature weighted by carbon monoxide values (in layers greater than 100 ppbv), b) plume altitude (AGL and ASL): altitude at the maximum carbon monoxide VMR, and c) plume pressure: the pressure at the maximum carbon monoxide VMR (shown in Figure 3.2d).

3.2.4 Other Satellite Datasets

We use observations of active fire hotspots from the Visual Infrared Imaging Radiometer Suite (VIIRS) aboard the S-NPP satellite to locate active fires and assess their relative fire radiative power (FRP). The VIIRS 375m active fire product is provided by the Fire Information for Resource Management Systems (FIRMS) (https://doi.org/10.5067/FIRMS/VIIRS/VNP14IMGT_ NRT.002). We use daytime observations with high and nominal confidence for all figures apart from the analysis in Section 3.3.2, where daytime retrievals with only high confidence are used. FRP represents the instantaneous radiative energy that is released from actively burning fires. In general, larger values of FRP are often associated with larger fires with hotter burning temperatures, which would often be characterized as more flaming combustion. However, some nuance is needed in the interpretation of FRP, as

the Planck function is highly non-linear around 3.9 microns (the band used for active fire detection) in its response to hot objects so a sub-pixel scale small and hot fire can yield a FRP that is similar to a sub-pixel scale larger and cooler fire. FRP has been related to the rate of biomass consumption (Kaufman et al., 1998) and thus is used to estimate the rate of emissions from satellite observations (Griffin et al., 2024; Ichoku & Kaufman, 2005; Stockwell et al., 2014).

We leverage observations of the aerosol Vertical Feature Mask (VFM) from the Cloud-Aerosol Lidar with Orthogonal Polarization (CALIOP) aboard the Cloud-Aerosol Lidar and Infrared Pathfinder Satellite Observation (CALIPSO) platform to assess the vertical distribution of smoke in the atmosphere. CALIPSO was launched in 2006 and flew in the NASA A-train, a constellation of satellites flying in a sun-synchronous polar orbit with a ~13:30 Local Time (LT) ascending node overpass time, until 2020 when it was dropped in orbit to the C-train along with CloudSat until it was decommissioned in 2023 (NASA, 2025). We use the L2 VFM version 4-51 data product (Winker, 2023) for two days coinciding with CrIS detections of wildfire plumes, July 27 and August 3, 2018. CALIPSO Lidar observations enable further interpretation of CrIS NH_3 smoke enhancements, discussed further in Section 3.3.3.

It should be noted that all satellite observations used in this study were taken at ~13:30 local time, which precedes the typical diurnal peak in fire activity (~15:00 local time. Although a 13:30 overpass is more representative of daily fire activity than a morning observation, it fails to capture the period of maximum fire intensity and plume injection, as intensity and boundary-layer depth are still increasing at this time. As a result, the most extreme smoke injection heights are likely missed, and this analysis should be interpreted as conservative relative to the daily peak in fire activity.

3.2.5 In situ NH_3 and CO Observations during WE-CAN

The CrIS dataset coincides with the Western wildfire Experiment for Cloud chemistry, Aerosol absorption, and Nitrogen (WE-CAN) that sampled numerous wildfire smoke plumes in the summer of 2018. Full details on the WE-CAN can be found in (J. F. Juncosa Calahorrano, Lindaas, et al., 2021b). WE-CAN in situ measurements can provide additional context to the CrIS measurements including approximate altitudes for dense portions of the smoke plumes and details about the NH_3 and CO measurements can be found in Pollack et al. (2019) and Lebegue et al. (2016), respectively. The NSF/NCAR C-130 sampled smoke plumes in a pseudo-Lagrangian fashion, resulting in multiple transects across the plume. In situ NH_3 NEMRs decayed strongly during WE-CAN as discussed by (Lindaas, Pollack, Calahorrano, et al., 2021a), which focused largely on the fresher portion of the plumes (0-5 hours downwind). We focus the results and discussion on several additional plumes including a plume sampled on July 26 from the Carr Fire. The Carr fire ignited on 23 July and burned through 229,651 acres before containment on 30 August (Wikipedia, n.d.-a), smoke plumes on August 2 and 3rd from the Mendocino Complex, and an isolated plume from the Pole Creek Fire (September 13, 2018). This last plume was not sampled by WE-CAN but offers an example of an isolated plume without the complexity of surrounding smoke or agricultural emissions.

3.3 RESULTS

3.3.1 Evolution of NH_3 in Individual Smoke Plumes

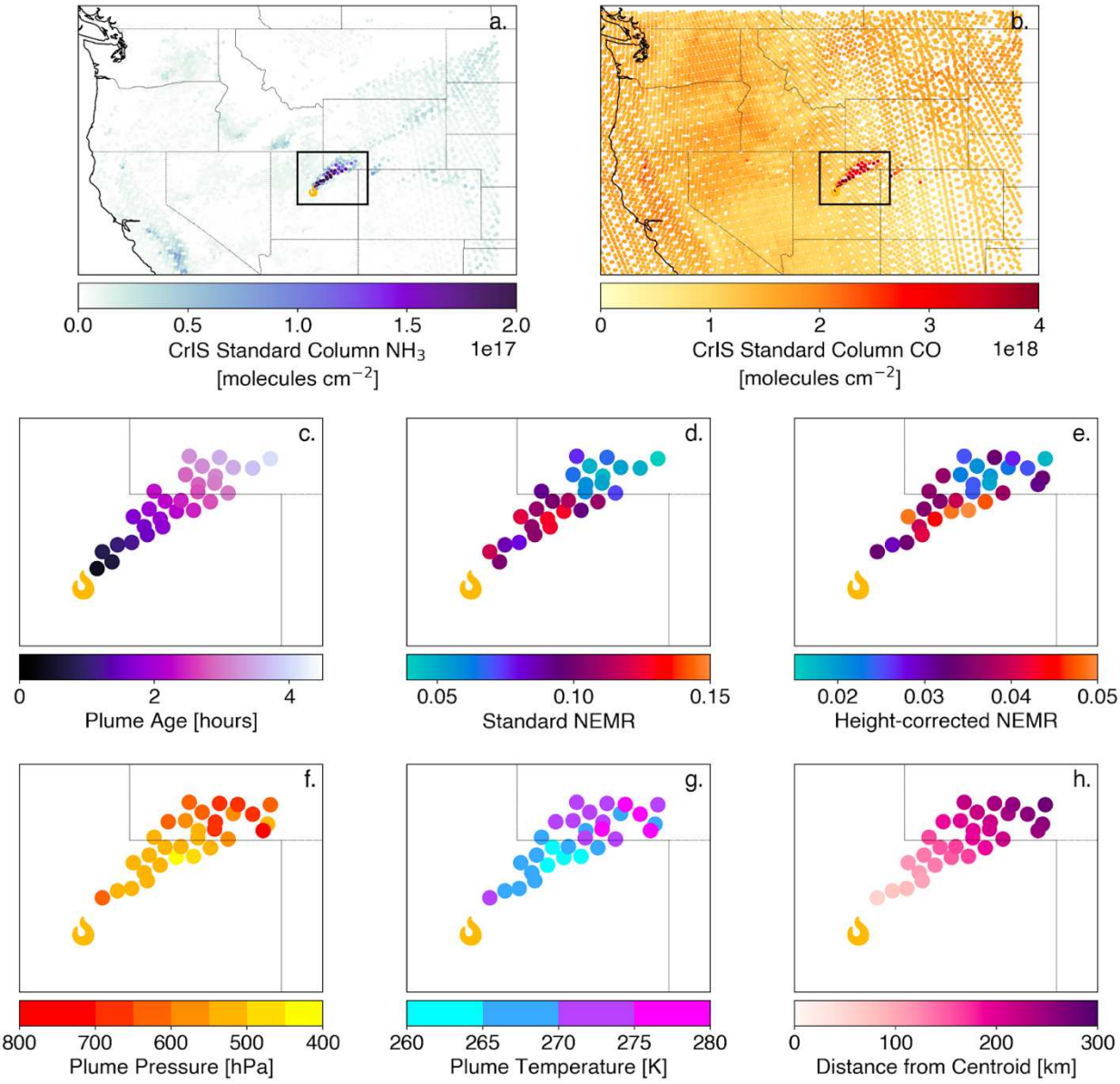

Figure 3.3: (a) CrIS column NH_3 and (b) column CO retrievals from September 13, 2018. Black boxed region in (a) and (b) denotes region plotted in (c-h). (c) Pole Creek Fire plume isolated by using points where column CO > 2e18 molecules cm^{-2}. Plume age assigned to each CrIS footprint assuming a mean wind speed of 19 m/s (Juncosa Calahorrano et al., 2021). The location of the fire centroid is shown by the orange icon. (d) NH_3 Normalized Excess Mixing Ratio (NEMR) calculated using the standard NH_3 retrievals. (e) NH_3 NEMR for height-corrected retrievals. (f) Plume pressure in [hPa], (g) plume temperature in [K] from the height-corrected retrievals, and (h) distance from the fire centroid in [km].

Figure 3.3 presents CrIS NH_3 (Figure 3.3a) and CO (Figure 3.3b) for the Western U.S. on September 13, 2018. The isolated and concentrated plume is from the Pole Creek Fire in Utah, and this plume has previously demonstrated the ability of CrIS to capture the chemical evolution

of PANs in a smoke plume from space due to the isolation of the plume, high wind speeds, and high within-plume concentrations (Juncosa Calahorrano, Payne, et al., 2021) The Suomi-NPP overpass sampling of the plume occurred ~3.6-4.6 hours after the plume became visible from GOES-16 (Juncosa Calahorrano, Payne, et al., 2021). The plume does not cross a large area of variable background NH_3 concentrations. Figures 3.2a and 3.2b highlight the isolation of the Pole Creek Fire plume.

Figure 3.3c presents the estimated plume age of each CrIS footprint in the isolated fire plume; the plume was isolated using retrievals where column CO > 2e15 molecules cm^{-2} and age was calculated assuming a mean wind speed of 19 m/s (Juncosa Calahorrano, Payne, et al., 2021). Figure 3.4d presents the NEMR values for each CrIS footprint before applying the height correction and Figure 3.4e presents the NEMR values for each CrIS footprint after the height correction has been applied. There are some differences between the two, notably the scale of the height-corrected NEMR is almost half that value when this calculation is performed without the correction using the standard NH_3 retrievals highlighting the likely overestimation of in-plume NH_3 in these retrievals. Figures 3.3f-h present the plume pressure, temperature, and distance from the fire centroid of each CrIS footprint, respectively, calculated during the height-correction. Examination of the standard NH_3 NEMR (Figure 3.4d) could suggest that the observed decrease reflects progressive partitioning of NH_3 into the particle phase as the plume ages roughly 150 km downwind from the fire centroid; however, concurrent plume temperature estimates indicate that the plume may not have been cold enough to make this process thermodynamically favorable based on prior analyses of in situ measurements of other plumes during WE-CAN (Lindaas et al., 2021). Rather, it is more likely that the variability in NEMR with plume age reflects temporal changes in emissions at the fire source, such that smoke emitted

~4 hours prior to the CrIS overpass contained less NH_3 than smoke emitted ~2 hours prior to the observation. Applying the height-correction to the Pole Creek plume suggests that the observed variability in NH_3 NEMR may reflect the evolution in NH_3 emissions by the fire rather than chemical loss of NH_3 in the plume.

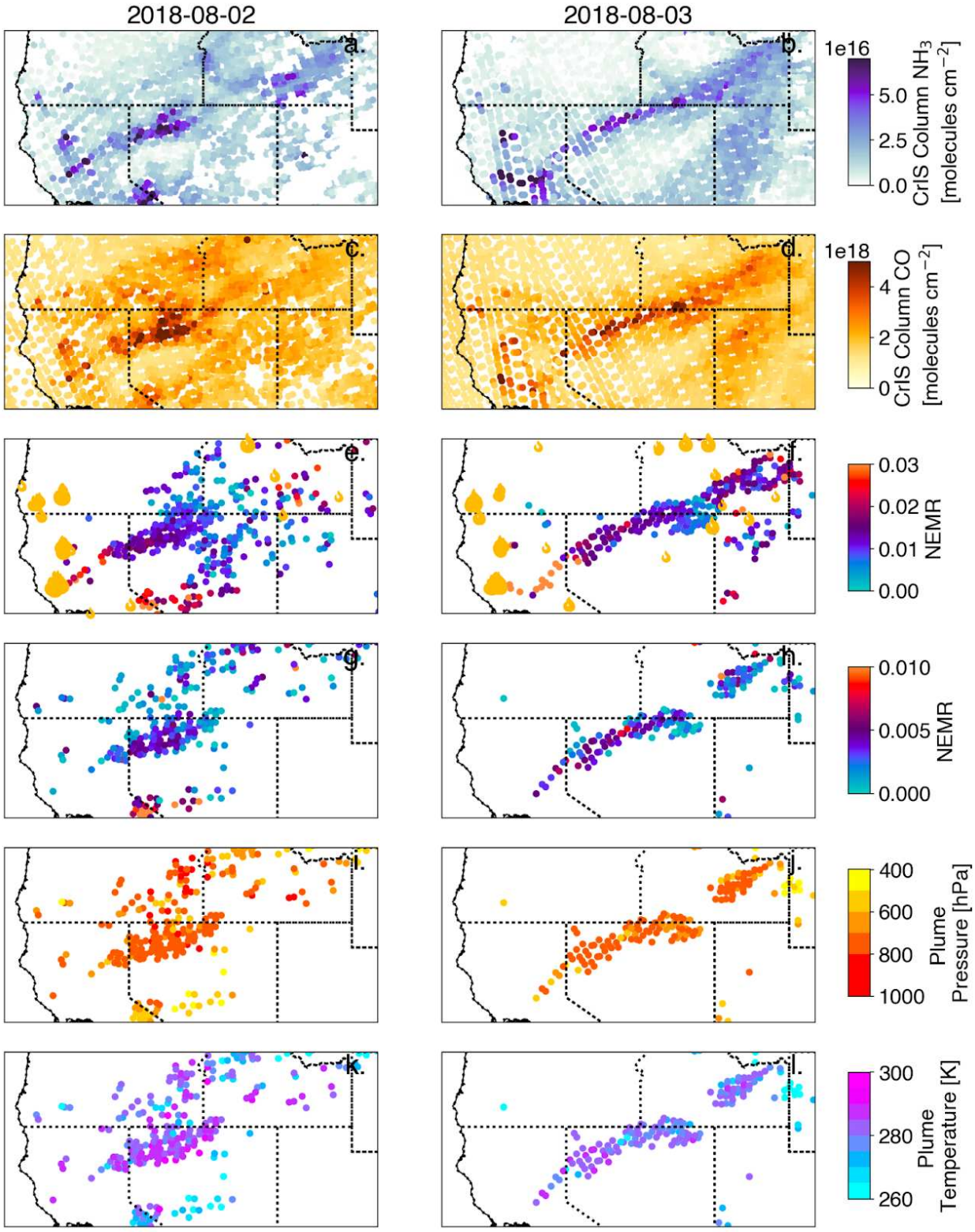

Figure 3.4: (a, b) CrIS standard column NH_3 for (a) August 2 and (b) August 3. (c, d) Corresponding CrIS standard column CO for the same dates. (e, f) NH_3 normalized excess mixing ratios (NEMRs) for isolated smoke plumes calculated using the standard NH_3 retrievals. Plume regions were identified based on thresholds of column CO > 2e18 molecules cm^{-2} and

column PANs > 3e15 molecules cm^{-2} for the Mendocino Complex smoke plume. VIIRS active fire detections are shown as orange icons, sized by relative FRP. (g, h) Height-corrected NH_3 NEMRs for isolated smoke plumes where XCO > 100 ppbv for the column. (i, j) Plume pressure and (k, l) plume temperature calculated during the height correction.

The Mendicino Complex provides a longer case study of aging than the Pole Creek Fire plume and demonstrates some of the challenges associated with such extended analyses. Figure 3.4 presents CrIS retrievals of NH_3 (Figure 3.4a-b) and CO (Figure 3.4d-e) for August 2 and 3, 2018 when the Mendocino Complex Fire experienced significant growth. The Mendocino Complex Fire was a large complex of wildfires that burned for three months and consumed over 400,000 acres. August 2 and 3 experienced >30,000 acres of growth each day (~70,000 acres total). The smoke plumes are evident in visible imagery from these days as the smoke travels eastward out of Northern California and is highlighted by the elevated levels of NH_3 and CO in Figure 3.4a-d crossing northern Nevada and Idaho. Figure 3.4 also demonstrates the ability of CrIS to track plumes over the course of multiple days; smoke emitted on August 2nd continues to be discernible in the CrIS data on August 3rd. The NEMR values for each CrIS footprint along the isolated plumes are shown for August 2nd (Figure 3.4e) and August 3rd (Figure 3.4f). The NEMR (Figure 3.4e) calculated with the standard NH_3 retrievals decreases with distance from the Mendocino fire centroid, and this is most obvious across both days west of the Nevada-Utah border (~114°). Figure 3.4g presents the height-corrected NEMR and Figure 3.4i shows the corresponding plume pressure and Figure 3.4k shows the plume temperature. Unlike Figure 3.4e, the height-corrected NEMR does not appear to decline with westerly advection. Figures 3.3i and 3.3k suggest little variability in pressure and temperature in this plume. The height-corrected data shows that NH_3 in wildfire smoke plumes may travel great distances without undergoing chemical loss.

On August 3rd, smoke traveled in a concentrated, thick plume until it dissipated over southeastern Idaho (Figure 3.4f). The NEMR values exhibit a modest increase as the plume advects into Idaho, likely reflecting contributions from locally emitted fresh smoke. VIIRS active fire detections reveal numerous smaller fire sources in the region (Figure 3.4f), which are co-located with areas of elevated NEMR within the plume. This portion of the plume is further explored with the CALIOP LiDAR in Section 3.3.3. Figure 3.4h presents the height-corrected NEMR values and the corresponding plume pressure and plume temperature are shown in Figures 3.3j and 3.3l. Similarly to August 2, variability in the height-corrected NEMR roughly follows variability in plume pressure and temperature, or lack thereof. The Mendocino Complex plumes display the far-reaching impacts of NH_3 traveling in wildfire smoke plumes.

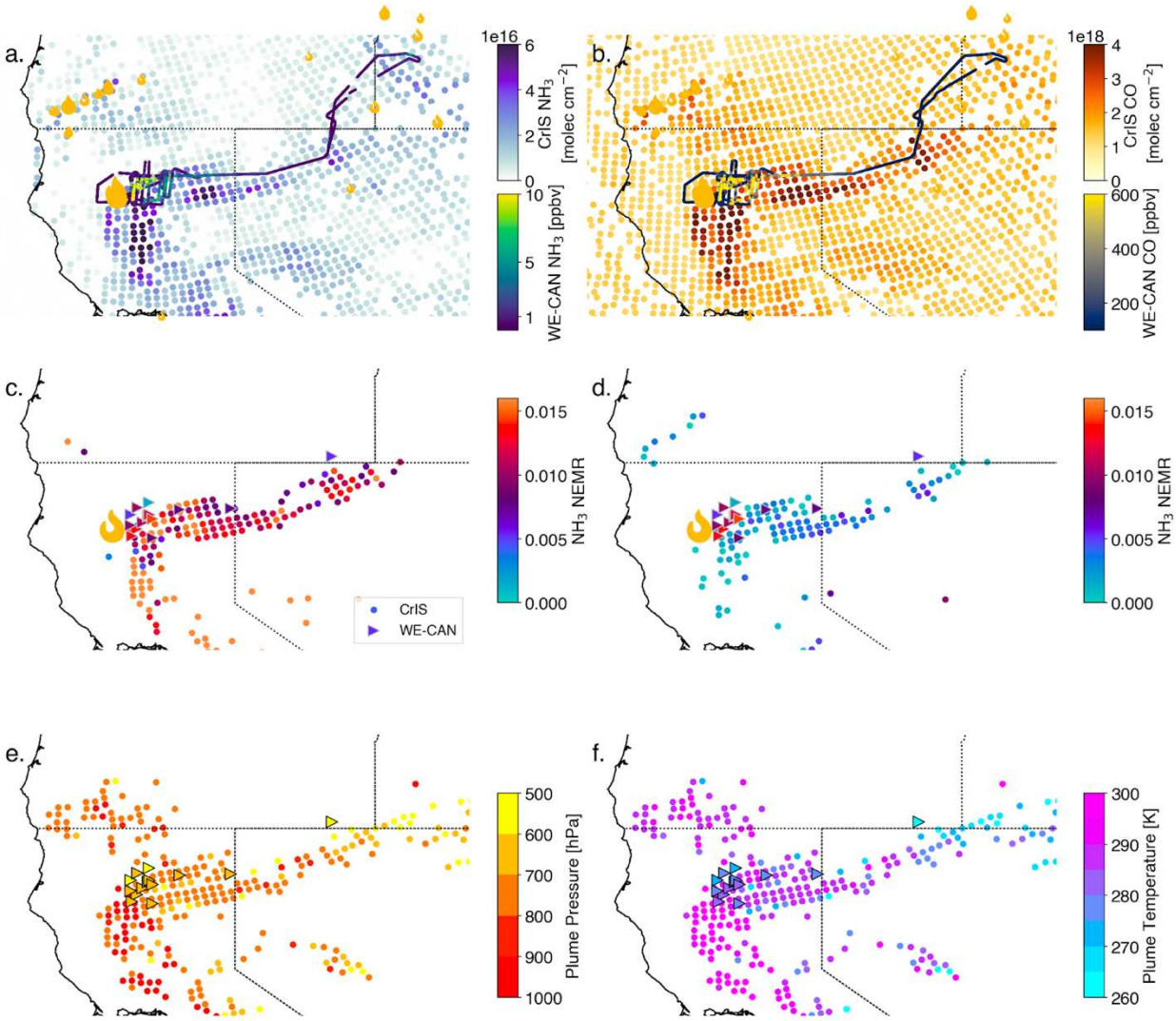

Figure 3.5: (a) NH_3 on July 26 from both in situ airborne and standard product satellite observations. The CrIS column mean tropospheric NH_3 is plotted as background (blue - purple scale) and the WE-CAN NH_3 observations are overlaid (the color of the aircraft line). VIIRS fire hotspots are shown as orange icons, sized by their relative FRP. (b) CO on July 26 from both in situ airborne and satellite observations. The CrIS column mean tropospheric CO is plotted as background, and the WE-CAN CO observations are overlaid. (c) NH_3 NEMR f CrIS data (circles; units: [molecules cm^{-2}/molecules cm^{-2}) and WE-CAN (triangles; units: [ppbv/ppbv]) for the Carr Fire plume isolated where column CO > 2e18 molecules cm^{-2}. CrIS data shown as circles; aircraft data as triangles. Carr Fire location is indicated by VIIRS hotspots. (d) NH_3 NEMR from height-corrected CrIS data (circles; units: [molecules cm^{-2}/molecules cm^{-2}]) and WE-CAN (triangles; same as in (c)). NH_3 NEMR from CrIS (orange circles) and WE-CAN (triangles, colored by C-130 altitude), binned by plume age. (e) Plume pressure from CrIS (circles) and WE-CAN (triangles) and (f) plume temperature from CrIS (circles) and WE-CAN (triangles) calculated as a step in the height-correction process.

The Carr Fire plume offers the opportunity to compare plume evolution from both airborne and satellite perspectives. Figure 3.5 presents standard retrieved NH_3 from CrIS (Figure 3.5a) and CO (Figure 3.5b) from CrIS and the aircraft. These measurements are not perfectly aligned in time; the aircraft observations were collected a couple of hours later (satellite overpass ~13:30 LT {~19:30-20:30 UTC}; research flight: 20:19 - 02:09 UTC). Despite this temporal offset, general spatial enhancements in NH_3 and CO are roughly co-located between the satellite and aircraft observations.

Figure 3.5c-d presents the values of the NH_3 NEMR from both measurements; where Figure 3.5c contains standard CrIS data and Figure 3.5d contains the height-corrected data. In general, the distribution of WE-CAN NEMR values declines with distance from the fire centroid and this is vaguely visible in Figure 3.5c. The scale of the NEMR calculated using the height-correction is much smaller than shown in Figure 3.5c, reflecting the overestimation in NH_3 prior to performing the correction. and Figure 3.5d shows relatively little variability in the NH_3 NEMR across most of the plume with deviations in the height-corrected NEMR largely coincident with changes in plume thermodynamic conditions (Figure 3.5e-f). In the CrIS measurements, elevated temperatures and pressures near the Carr Fire centroid correspond to some of the lowest NEMR values observed in Figure 3.5d. Visible imagery suggests that smoke accumulated within the Sacramento Valley over multiple days, allowing portions of the plume to remain close to the surface where loss of NH_3 is possible via deposition to the surface.

It is likely that there is smoke at multiple altitudes downwind of the fire toward the east, as the WE-CAN pressure measurements indicate higher altitudes (~500 hPa) of smoke near the fire source than CrIS (~900 hPa). WE-CAN sampled the smoke during a period of rapid fire

growth, and the smoke injection altitude likely rose rapidly between the CrIS overpass time and the aircraft observations. Further downwind, near the Nevada-Idaho border, both plume pressure and temperature are lower across both measurements, coinciding with a reduction in height-corrected NEMR. Under these conditions the partitioning of NH_3 into the particle phase becomes thermodynamically favorable, providing a potential explanation for the observed decline in NEMR. WE-CAN and CrIS temperature and pressure measurements show more agreement further from the fire centroid (Figure 3.5e-f) and it should be noted that the WE-CAN observations were later in the day with a higher injection height providing an explanation to the lower temperature and pressure aircraft measurements compared to the satellite.

3.3.2 Near-field Evolution of the Fire Centroid across the Wildfire burning cycle

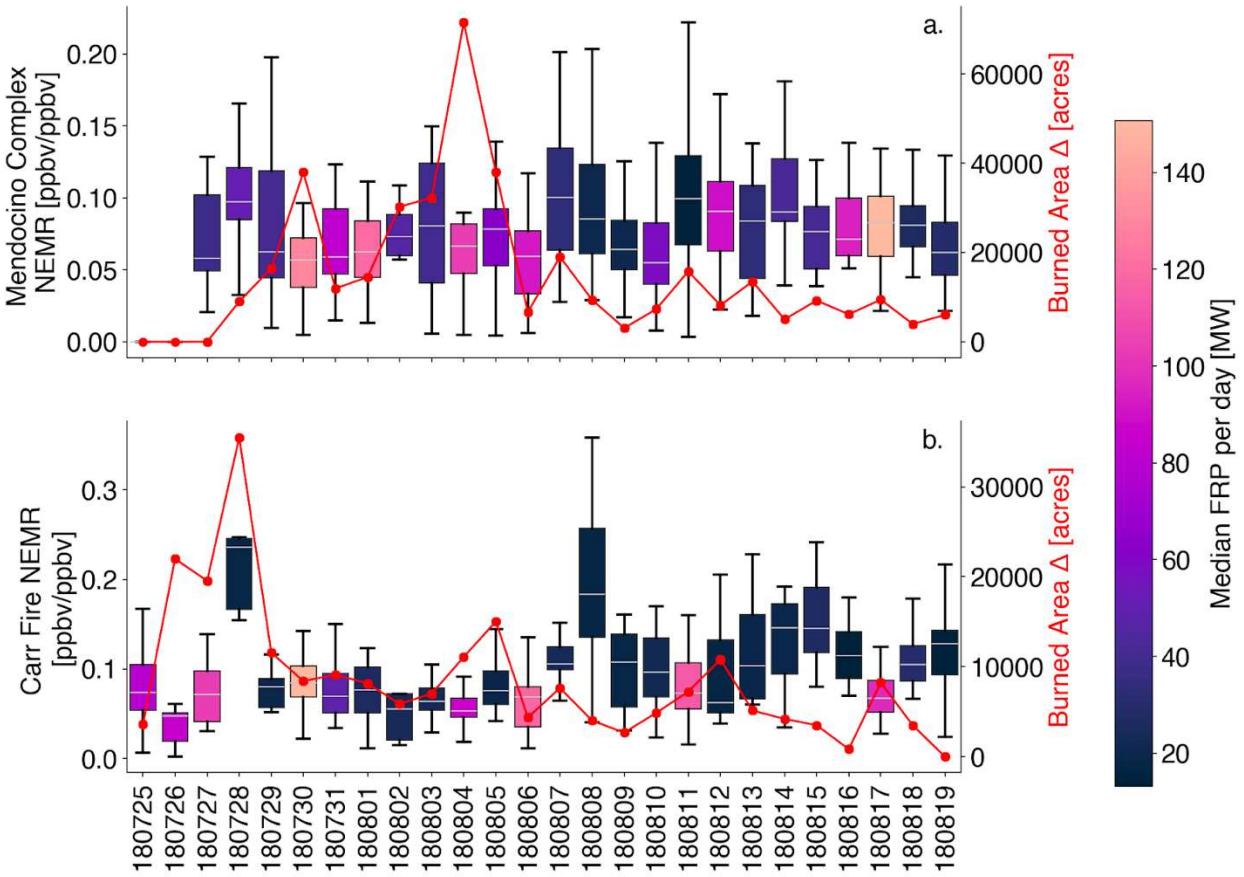

Figure 3.6: Distributions of CrIS NH_3 NEMR [ppbv/ppbv] values for Mendocino Complex fires (a; 38.24°N, 40.25°N, -123.9°W, -121.9°W) and Carr Fires (b; 40.6°N, 41.6°N; -122.6°W, -121.6°W) colored by the median VIIRS FRP value per day [using only high confidence retrievals]. The silver line represents the median value. The red lines represent the respective burned area difference from the previous day (Wikipedia, n.d.-b, n.d.-a).

Northern California experienced an extreme fire season in 2018 (Brown et al., 2020) and this provides an opportunity to examine relationships between large long-burning wildfires and NH_3 NEMRs from space. The Carr and Mendocino Complex fires burned for 1.5 and 3 months, respectively, which resulted in smoke transported within and out of Northern California (Casey et al., 2021; Mueller et al., 2020). The Carr Fire burned between 23 July - 30 August and the Mendocino Complex Fire burned between 27 July - 18 Sept (Wikipedia, n.d.-b, n.d.-a). We estimate that smoke contributed to ~70% of the NH_3 observed over Northern CA and NV and

~50% of NH_3 over the Snake River Valley, ID based on satellite measurements (Appendix B Figure A2.2).

The evolution in wildfire-driven enhanced NH_3 from space can give insight to the temporal evolution of NH_3 enhancements near the fire centroid across the active burning period. To characterize the near-source region we define a rectangular area originating near the fire centroid and oriented along the down-wind direction of the plumes. This area is meant to capture freshly emitted smoke in close proximity to the fire centroid. There is some spread in NEMR values within this rectangular area, but robust patterns exist within the distributions of NEMRs. Figure 3.6 presents the distributions of NEMR values within these boxes for the Mendocino Complex Fire (Figure 3.6a) and the Carr Fire (Figure 3.6b). Across both fires, higher values of VIIRS median daily FRP are associated with lower distributions in NEMR, where days with median NEMRs > 0.10 are always associated with FRPs < 50 MW across both fires. A similar relationship exists between NEMR and fire pixel brightness temperature (I-5 channel brightness temperature of fire pixel), where higher values of brightness temperature are always associated with lower distributions of NEMR values (Figure A2.3 in Appendix C).

Days with more active fire growth (i.e., peaks in burned area difference; red line in Figure 3.6) are often associated with lower NEMR distributions. This relationship is more pronounced for the Mendocino Complex Fire. For example, the day with the highest growth (August 4th; Figure 3.6a) was associated with a higher median FRP value (~100 MW) and a lower distribution of NEMR values (median: ~0.06). Conversely, many days without large active growth (ex: August 8th; Figure 3.6a) were associated with lower median FRP values (~20 MW) and a higher distribution of NEMR values (median: ~0.075). The most rapid growth for the Carr Fire occurred during the first few days of burning (Lareau et al., 2018), and this relationship

between burned area, FRP, and NEMR is most evident during July 25-27 (Figure 3.6b). July 26 was characterized by rapid vertical development and a destructive fire-generated vortex where surface wind speeds exceeded 64 m/s, equivalent to an EF-3 tornado (Lareau et al., 2018). July 25-27 had higher relative daily median values for FRP (and brightness temperature; Appendix B Figure A2.3) associated with some of the lowest distributions of NEMR values across the shown period. However, July 28th serves as an exception to this rule, where a peak in Carr Fire burned area difference was associated with a low FRP (~20 MW) and high NEMR distribution (median:~0.23) (Figure 3.6b). This day exhibited pervasive smoke across the northwest coast, with contributions from numerous active fires (including the Mendocino Complex), making it difficult to attribute enhancements directly to the Carr Fire alone.

There are notable differences between the NEMR and FRP relationships for the Carr versus Mendocino Complex Fires. The Carr Fire burned for 35 days and reached a final burn area of 229,651 acres and the Mendocino Complex Fire burned for 55 days and reached a final burn area of 459,123 acres (Wikipedia, n.d.-c). While these were both massive fires, Figure 5 highlights some differences between them. The Carr Fire (Figure 3.6b) overall had higher distributions of NEMR values and lower median FRP values (this is also true for brightness temperature) than observed in the Mendocino Complex Fire (Figure 3.6a). The peaks of burned area difference for the Mendocino Complex are nearly twice the magnitude as they are for the Carr Fire (~71’000 vs ~35’000 acres). These discrepancies likely reflect differences in burning conditions between the two fires. The Mendocino Complex Fire burned for longer and consumed a larger area than the Carr Fire, which is consistent with its larger FRP values, as fire growth is often associated with higher FRPs.

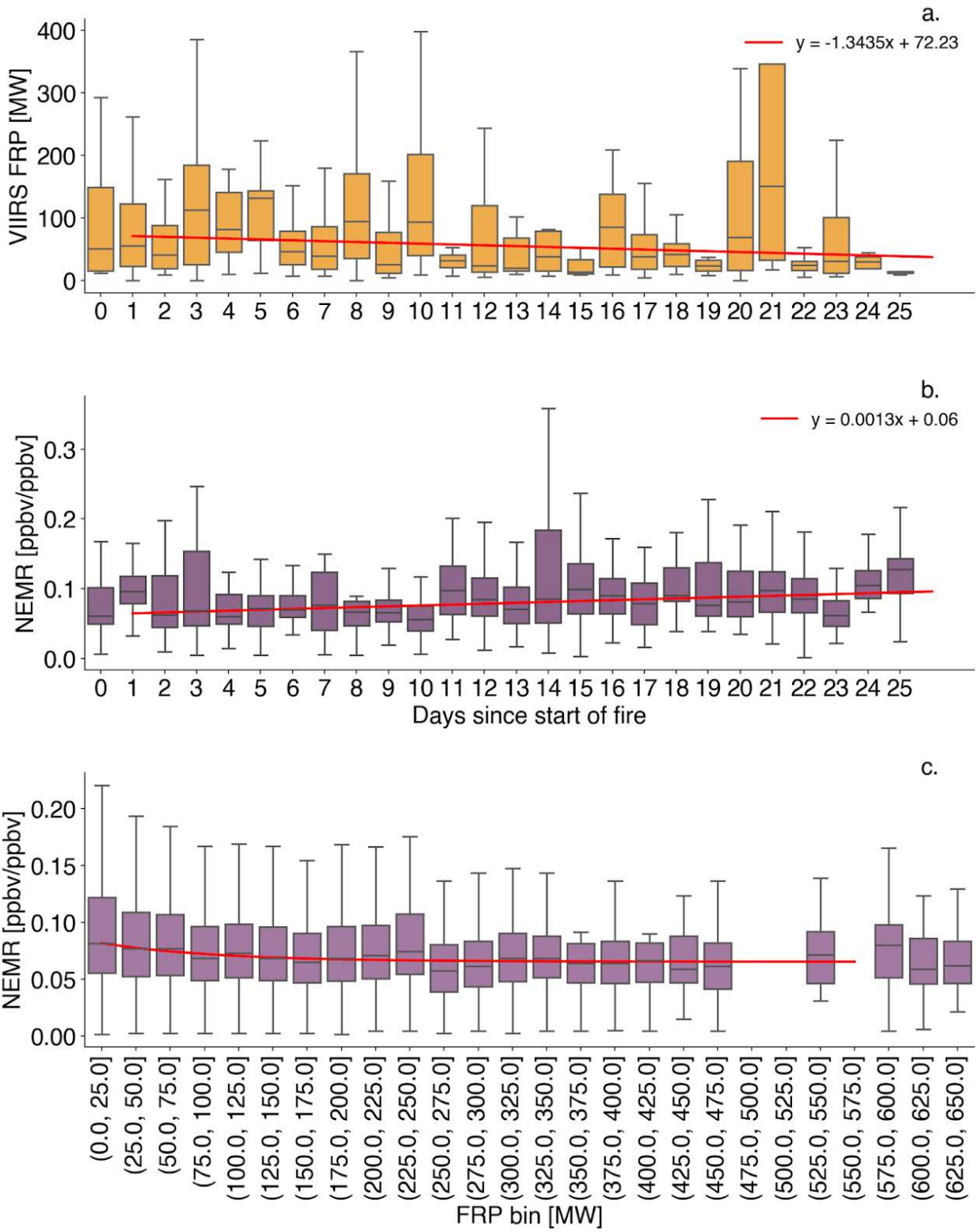

Figure 3.7: Combined Carr and Mendocino values. (a) Distributions of values of VIIRS FRP across the burning periods for the two fires. The red line represents a linear regression based on the median of each distribution. (b) Distributions of values of CrIS NH_3 NEMR across the burning periods for the two fires. The red line represents a linear regression based on the median

of each distribution. Day 0 represents July 25th for the Carr Fire and July 27th for the Mendocino Complex Fire. (c) Distributions of NH_3 NEMR values for binned FRP values across the burning periods for both fires. The red line represents an exponential fit based on the medians estimated using the scipy.optimize.curve_fit function in Python.

Figure 3.7 presents combined NH_3 NEMR and FRP values from both fires. Figure 3.7a displays the evolution in the distributions of daily median FRP values from the Carr and Mendocino Complex Fires. During 25 days of active burning, the distributions of FRPs declined as the fires approached containment. Figure 3.7b shows the temporal evolution of CrIS NH_3 NEMR distributions across the fire's active burning lifetime. The distributions of NH_3 NEMR tend to increase slightly with time, in contrast to FRP, as burning conditions shift from a more flaming, fresh fire to more smoldering conditions. The relationship between FRP and NH_3 NEMR is shown in Figure 3.7c, where the highest distributions of NEMRs are associated with the lowest bins of FRP values across both fires.

3.3.3 Insights from CALIPSO for Interpreting Plume Evolution

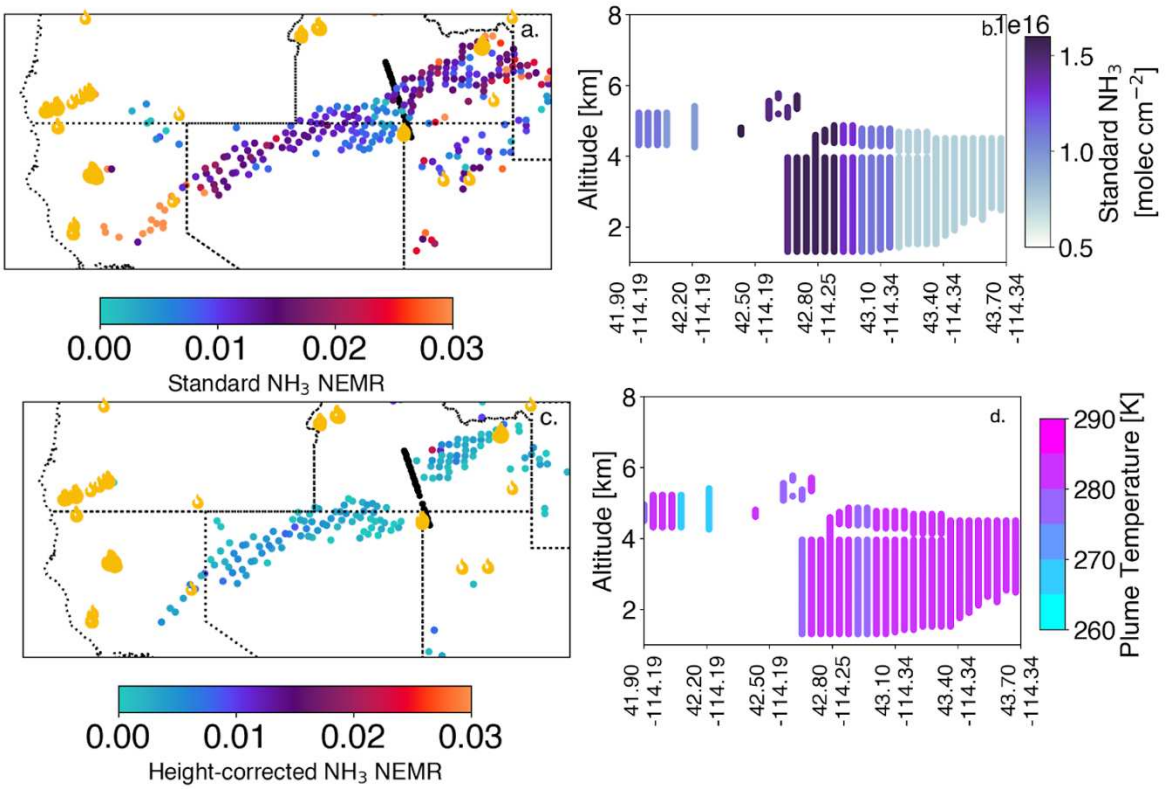

Figure 3.8. (a) CrIS standard NH_3 NEMR values for the August 3, 2018 smoke plume emanating from the Mendocino Complex Fire. VIIRS active fire detections are shown as orange markers, scaled by FRP. The CALIPSO track intersecting the plume is shown in black. (b) CALIPSO smoke profile along the track in (a), colored by collocated CrIS standard column NH_3 [molecules cm^{-2}]. (c) same as (a) but showing the height-corrected NH_3 NEMR for the same day. (d) same as (b) but showing the collocated plume temperature estimated during the height correction.

Figure 3.8 displays a smoke plume for August 3 (Mendocino Complex) using the standard NH_3 product and the height-corrected NH_3. This plume serves as a good example of long-range transport of a California wildfire plume from the perspective of the evolution of in-plume enhanced NH_3. Overlapping smoke sources and vertical mixing can complicate the interpretation of trace gas enhancements in satellite observations. This figure also highlights the difficulty of integrating different datasets, as CALIPSO's narrow ground track and 16-day repeat cycle result in extremely sparse spatial sampling, such that the revisitation likelihood or

intersecting a dense smoke plume relevant for our analysis very low; additionally, the overpass analyzed here occurs over a region with very high background NH_3 emissions associated with agriculture, further complicating a multi-dataset analysis of this plume. Figure 3.8a presents the NEMR values in each CrIS footprint for the isolated Mendocino Complex Fire plume on August 3, 2018, and serves as an example of the complexity of interpreting the chemical evolution of plumes using satellite data alone. Figure 3.8b shows the CALIOP profile for the portion of this plume highlighted by the black line denoting the CALIPSO ground-track in Figure 3.8a. The CALIPSO aerosol profile has been colored by the closest standard CrIS NH_3 value (calculated using a k-d tree in latitude longitude space) and highlights the presence of a smoke plume at roughly 1-4.5 km. The CALIPSO overpass occurs over the Snake River Valley; an area with exceptionally high surface NH_3 emissions and thus is a location not ideally suited for applying the height-correction. Figure 3.8c shows the height-corrected NH_3 NEMR for this plume, where height-corrected NH_3 coincident with the CALIPSO ground track had been filtered out as the CO did not meet the heavy-smoke criteria, and further highlights the difficulty in integrating datasets. Figure 3.8d presents the plume temperature, calculated during the height-correction retrieval, for the footprints associated with the CALIPSO track. Satellite estimates of plume temperature are similar to those measured during WE-CAN at a similar plume altitude (Juncosa Calahorrano et al., 2021). The CALIPSO lidar data enables us to note the vertical location of the smoke column, and the location of the CALIPSO smoke column roughly agrees with our estimation based on the CrIS CO profile shape.

Figure 3.8a-d provides insight into the vertical distribution and NH_3 enhancement characteristics of the Mendocino Complex Fire plume on August 3, 2018, and the potential

influence of nearby smaller fires on observed NH_3 enhancements. Figure 3.8b shows a CALIPSO-observed smoke layer at 4.5-5.5 km in the more southern portion of the overpass and a smoke layer at 1-4.5 km in the more northern portion of the overpass. VIIRS active fire detections show numerous smaller fires around the Snake River Valley that are co-located with higher values of NH_3 NEMR in Figure 3.8a. The lower level (1-4.5 km) smoke in the CALIOP aerosol profile north of 42.6°N is likely more influenced by these smaller, local fires given the lower altitude of the smoke and higher relative NH_3 NEMR values.

3.4 SUMMARY & IMPLICATIONS

Here we develop methods for using satellite observations to investigate NH_3 in wildfire smoke plumes from satellite observations. Our analysis focuses on summer 2018, coinciding with in situ observations of wildfire smoke plumes from the WE-CAN field experiment. We demonstrate the ability of the CrIS instrument to observe enhancements of NH_3 in smoke plumes despite its major stationary sources. We investigate an anticipated height-bias in CrIS data by comparing the original forward model run of data to an additional forward model run designed to mitigate this bias.

1. Given the large agricultural sources of NH_3 in rural regions during the warm season, we present an approach to estimate the smoke-enhanced NH_3 while accounting for the spatial heterogeneity in NH_3 associated with persistent (non-wildfire) surface sources. We derive a "smoke-free" NH_3 grid using retrievals where tropospheric CO < 2e18 molecules cm^{-2} and we assign a value to each satellite footprint. We find this method produces normalized excess mixing ratio (NEMR) values that better reflect our expectations of the evolution of NH_3 in wildfire smoke plumes based on prior work.

2. The thermal infrared radiances measured by CrIS are more sensitive to changes in atmospheric NH_3 aloft than they are to similar changes at the surface, so the standard CrIS TROPESS NH_3 measurements represent an overestimate of NH_3 in lofted smoke. We use co-measured CO to correct this overestimate and we estimate the height-corrected NH_3 values to be roughly 50-80% lower than the standard NH_3 over the densest

portion of smoke plumes measured in the afternoon during an extreme fire season.

3. CrIS detects evolution in smoke-enhanced NH_3 in plumes that have been transported for several hours to days downwind from wildfires. We find that variability in the NH_3 NEMR can reflect both chemical evolution in a smoke plume and the temporal variability in NH_3 emitted by the fire.

4. Wildfires in the western U.S. often burn for days to weeks and over the lifecycle of the fire its burning conditions often dramatically shift. We examine the NH_3 NEMRs over the Carr and Mendocino Complex Fires for ~1 month of burning. We find a relationship between the distribution of near-fire-centroid NEMRs and daily median FRPs, where higher values of FRP are associated with lower NH_3 NEMRs.

5. When overlaps occur, combined information from CALIPSO and CrIS should enable further interpretation of the behavior of NH_3 in wildfire plumes.

In summary, we present approaches to examine the chemical evolution of a reactive species (NH_3) in individual smoke plumes from space. Our work demonstrates the ability of the CrIS instrument to observe chemical loss of NH_3 in wildfire smoke plumes and these methods can likely be applied to other species with both stationery and wildfire sources.

3.5 Data Availability Statement

CALIPSO data: NASA/LARC/SD/ASDC. (n.d.). CALIPSO Lidar Level 2 Vertical Feature Mask (VFM), V4-51 [Data set]. NASA Langley Atmospheric Science Data Center DAAC. Retrieved from https://doi.org/10.5067/CALIOP/CALIPSO/CAL_LID_L2_VFM-Standard-V4-51

VIIRS: NRT VIIRS 375 m Active Fire product VNP14IMGT distributed from NASA FIRMS. Available online https: //earthdata.nasa.gov/firms (last access: August 2021), https: //doi.org/10.5067/FIRMS/VIIRS/VNP14IMGT_NRT.002 (LANCE FIRMS, 2021b).

CrIS WE-CAN observations: This is a special (non-operational) TROPESS processing to process all pixels of CrIS within a spatial-temporal box and is found here: https://zenodo.org/records/17065859.

CHAPTER 4

EVOLUTION OF AMMONIA (NH_3) IN WILDFIRE SMOKE PLUMES FROM SPACE: INSIGHTS FROM A HYBRID OPTIMAL ESTIMATION AND MACHINE LEARNING RETRIEVAL APPROACH

4.1 INTRODUCTION

As mentioned in Chapter 1, biomass burning is the primary terrestrial source of atmospheric ammonia (NH_3). Chapter 4 follows Chapter 3 in discussing NH_3 in wildfire smoke plumes.

Reactive nitrogen (N_r = all N-containing species apart from N_2 and N_2O) emissions from natural biomass burning originate from the nitrogen content within the fuel itself. Natural fires typically do not reach temperatures high enough to produce thermal NO_x through the reaction of atmospheric N_2 and O_2, so fuel-bound nitrogen is the dominant source (Roberts et al., 2020). The amount of reactive nitrogen released therefore varies with fuel type, as different fuel materials contain different levels of nitrogen. Fuel moisture and arrangement can also affect the combustion characteristics and relative emissions of reactive nitrogen compounds (L.-W. A. Chen et al., 2010; Lindaas, Pollack, Garofalo, et al., 2021b; McAllister, 2019). In general, higher nitrogen content in biomass leads to greater emissions of reactive nitrogen species upon combustion (Burling et al., 2010; Coggon et al., 2016b; Kuhlbusch et al., 1991; Stockwell et al., 2014). Combustion efficiency is particularly important in determining the variability of NH_3 emissions (Roberts et al., 2020). Smoldering combustion tends to emit more NH_3 than flaming combustion (Lindaas, Pollack, Calahorrano, et al., 2021a; Roberts et al., 2020; Yokelson et al., 1996, 1997). However, the relationship between combustion efficiency and NH_3 emissions can be highly non-linear (Tomsche et al., 2023).

These satellite instruments take near-continuous observations of the entire globe, amounting to a massive amount of data to be processed and converted into NH_3 measurements. The NASA TROPESS project generates consistent, long-term records of various trace gases, including NH_3 and CO (Bowman et al., 2021). The TROPESS project builds on the TES legacy by applying a unified optimal estimation (OE) (Rodgers, 2000) algorithm across multiple satellite platforms. TROPESS emphasizes uncertainty characterization, and consistency between datasets and platforms (K. W. Bowman et al., 2006; Fu et al., 2016a). However, due to computational constraints, less than 2% of the available CrIS CO and NH_3 soundings are currently processed, leaving substantial gaps in potential global trace gas monitoring (Werner et al., 2025).

While machine learning (ML) offers powerful capabilities for atmospheric retrievals, its current limitations in uncertainty quantification and diagnostic outputs present challenges for broader adoption in remote sensing applications. ML models have the ability to efficiently learn complex nonlinear relationships within atmospheric science; however, limitations exist in terms of explainability and uncertainty quantification that have hindered its broader use in remote sensing (Tyralis & Papacharalampous, 2024). Traditional OE retrieval methods provide additional key diagnostic information (e.g., averaging kernels, degrees of freedom, error covariance, etc), along with the retrieval, but ML methods currently lack diagnostic analogues (Werner et al., 2025). Diagnostic information supplementing each retrieval is critical for data assimilation and model-observation comparisons (Jones et al., 2003; Miyazaki et al., 2015).

Here we present the use of a novel CrIS ML-based retrieval approach of NH_3 and CO in wildfire smoke plumes. This novel ML-based retrieval approach is a hybrid of OE and ML retrievals, leveraging the respective strengths of each. The hybrid retrieval framework uses a set

of the OE retrievals as a training dataset and as a source of physically meaningful priors. The ML-based algorithm then "fills in the gaps" left by OE, bridging observational gaps left by the current processing limits. This hybrid approach provides an interpretable pathway for the integration of machine learning into operational remote sensing processing and is further described in (Werner et al., 2025). A handful of studies have looked at NH_3 emissions and their evolution in biomass burning plumes using in situ sampling (Adams et al., 2019; Lindaas, Pollack, Calahorrano, et al., 2021a; Lindaas, Pollack, Garofalo, et al., 2021b; Tomsche et al., 2023). We have shown that OE satellite observations can extend the number of biomass burning plumes that can be analyzed using satellite observations in Chapter 3. Here we explore how these methods can be applied to a novel ML-based dataset and how ML-based datasets can be used to expand the current satellite dataset.

4.2 METHODS

4.2.1 TROPESS Data

We use observations from the CrIS instrument, a nadir viewing Fourier transform spectroradiometer currently flying on the Suomi-National Polar Orbiting Partnership (S-NPP) satellite and on the JPSS satellite systems, providing data continuity well into the 2040s. CrIS provides measurements of Earth view interferograms at 30 cross-track positions, each consisting of a 3 × 3 array of fields of view (FOVs), with each FOV measuring 15 km in diameter at nadir. S-NPP and the JPSS satellites fly in a sun-synchronous polar orbit with mean local daytime overpass around 13:30. CrIS provides calibrated Level 1B radiances in three spectral bands: 660-1095 cm^{-1} (long-wave), 1210-1750 cm^{-1} (mid-wave) and 2155-2550 cm^{-1} (shortwave). The CrIS instrument provides full spectral resolution radiances on a 0.625 cm^{-1} spectral grid.

TROPESS trace gas retrievals are provided on a reduced horizontal grid of 0.8° (Fu et al.,

2016b, 2018, 2019) that is based on the TES L2 processing algorithm (K. W. Bowman et al., 2006) and uses the OE retrieval approach (Rodgers, 2000). TROPESS retrievals of both CO and NH_3 are processed routinely and are available in the NASA GES DISC. Validation of TROPESS CO can be found in Worden et al. (2022) and validation of TROPESS NH_3 can be found in (Dammers et al., 2017). This study utilizes single-FOV CrIS-MUSES retrievals from the TROPESS forward stream (K. Bowman, 2021b, 2021a; K. W. Bowman, 2021b, 2021a).

4.2.2 Machine Learning Model

A full machine learning model has been developed, trained, and evaluated to simultaneously predict a variety of TROPESS variables using observed CrIS radiances and geolocation data as inputs and is fully described in (Werner et al., 2025). Briefly, the model takes 3 features as input: CrIS radiances at a specified wavenumber, the sensor viewing angle, and the surface altitude. These input features are represented as matrices, where each element $f^s_{1\text{-}3}$ corresponds to one of the N samples. The ML model then maps these features to a set of output labels ($\boldsymbol{L}_{1\text{-}3}$). The output labels are also structured as matrices and contain elements $l^s_{1\text{-}3}$ for each individual sample, denoted by s=1…N for the CrIS column. Output labels include: the CO or NH_3 column concentration, total column retrieval error, and the column averaging kernel at ~511 hPa (Werner et al., 2025).

The ML model developed in (Werner et al., 2025) is a feedforward artificial neural network (ANN), which maps the input to the output through several hidden layers. Each hidden layer contains a large number of interconnected neurons. The exact model structure and settings are determined through processes that are described in (Werner et al., 2021, 2023). The model training was done using Keras library for Python (v 2.10.0) (Chollet, 2015) with TensorFlow (v 2.10.0) as the backend (Abadi et al., 2016).

Specific features used for the CO and NH_3 models include radiances at all 2224 spectral channels for CO and NH_3, the field of view (FOV) index, latitude and longitude of each sample, UTC time, the day/night flag, the sensor viewing angle, the day of the year, and the TROPESS sub column a priori values (Werner et al., 2025). This yields an output matrix consisting of 24 predicted variables for each species, including: the sub column concentrations, column averaging kernels, and sub column retrieval errors. For the data used here, the model training was performed on a high-performance computing cluster and took ~10 days to converge to a solution of the 12,000,000 model weights (Werner et al., 2025).

4.2.3 Other Satellite Data

We use observations of active fire hotspots from the Visual Infrared Imaging Radiometer Suite (VIIRS) aboard the S-NPP satellite to locate active fires and assess their relative fire radiative power (FRP) in the same way as in Chapter 3. See section 3.2.2 for details about how VIIRS fire data were used in this analysis.

4.2.4 Normalized Excess Mixing Ratio (NEMR) calculations

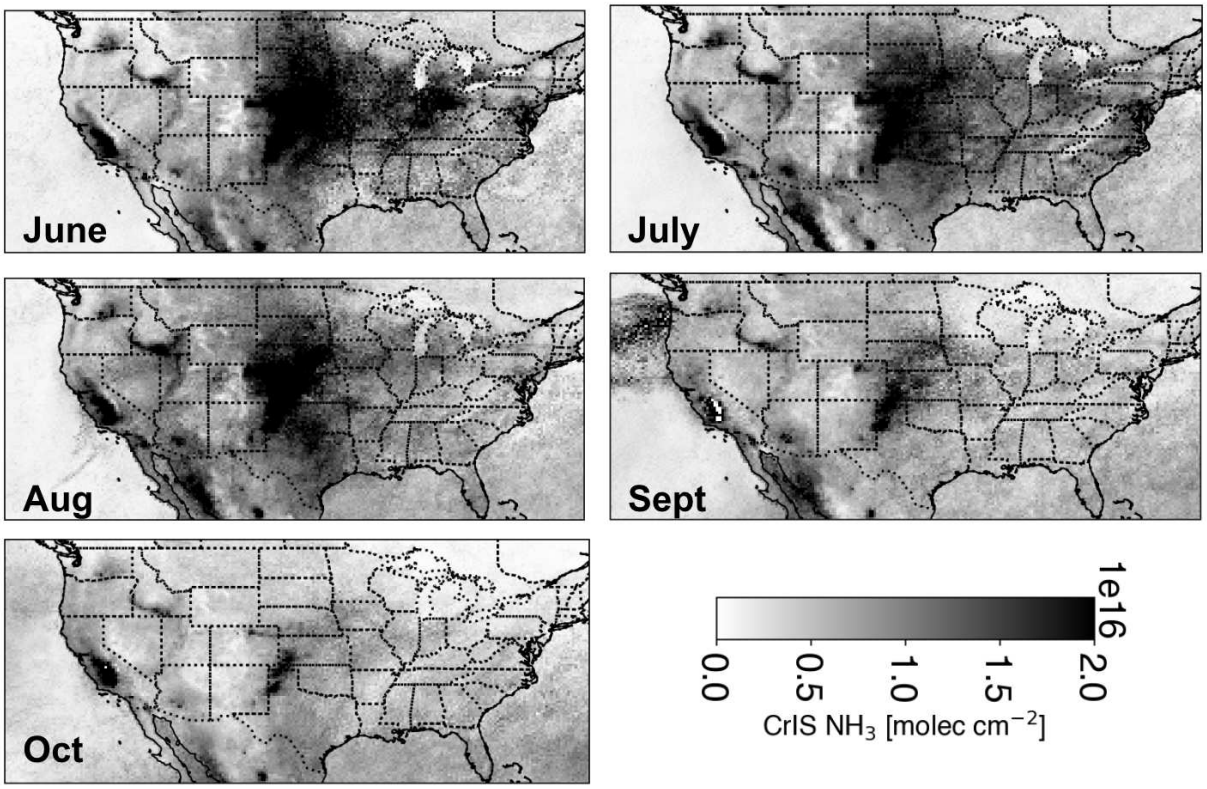

Figure 4.2: Estimated non-smoke background NH_3 from June through October 2020, calculated using retrievals where the CrIS-ML tropospheric column CO < 1.8e18 molecules cm^{-2}, gridded at 0.25° x 0.25° for June through October.

To evaluate the chemical loss of NH_3 in a smoke plume, we use the normalized excess mixing ratio (NEMR), or the enhancement ratio described in Section 3.2.3.

To calculate the NEMR using satellite observations, we follow the approach described in Chapter 3. We use a static CO background of 1.8e18 molecules cm^{-2}. This CO background represents the highest approximate value of CO in the "smoke-free" ML retrievals in the study area. This threshold was selected based on consistency with expected smoke features from OE-based retrievals and validated by confirming that plume isolation for 2018 events closely matched the results reported in Chapter 3. The background NH_3 is estimated using all retrievals where tropospheric column CO < 1.8e18 molecules cm^{-2} and we separate these background estimates by month. This approach, however, is not perfect and these background grids are not

completely free of the influence of smoke as exemplified by September in Figure 4.2, where enhanced NH_3 is observed off of the NW coast associated with smoke. Thus, these grids likely overestimate the true smoke-free average NH_3. This conservative approach means that NEMR calculations will only be positive for well-defined concentrated discrete smoke plumes.

Discerning the evolution of NH_3 in biomass burning plumes from satellite observations depends on our ability to isolate smoke plumes from elevated regions of NH_3 associated with agriculture. Figure 4.2 presents an estimate of no/low smoke NH_3 background from the CrIS ML-approach retrievals for the contiguous United States (CONUS) for five months, June through October. For all months, there are few regions that stand out with persistently high NH_3 (e.g., the Snake River Valley, ID; Central Valley, CA, among others), and all of these areas are home to concentrated agricultural activities, either animal husbandry or crop production. There is also seasonality variation in NH_3 concentration evident in Figure 4.2. NH_3 volatilization from manure/urine has a strong temperature dependence, and both the environmental conditions and management practices influence how much NH_3 is volatilized from fertilizer application and this has been observed in prior satellite datasets (R. Wang et al., 2021). We use the month of August as a conservative approach to removing the persistent agricultural source of NH_3 embedded in the retrievals from our calculations of NEMR for all figures. The NH_3 hotspot around the central US is highest in June and there are many hotspots along the eastern US that peak in July. The hotspot around the Snake River Valley, ID peaks in August. In general, the background across the entire US peaks in August (Figure 2.2b), so using August as the background, or using a mean containing August, is thus the more conservative approach in estimating the background no/low smoke NH_3. An estimate of the mean NH_3 per surface type on a monthly basis (Appendix C Figure A3.1-3) and we find croplands, temperate/sub-polar grasslands, tropical/sub-tropical

broadleaf deciduous forests, urban buildup, and tropical/subtropical grasslands to have the highest mean background NH_3 concentrations. However, from this analysis we find that using land classification alone is insufficient to completely estimate NH_3 background value distributions per land cover type because this product does not include information about animal feeding lots, which are a significant source of NH_3. Animal feeding lots are likely grouped in with croplands and grasslands.

4.3 Results and Discussion

4.3.1 Comparing Machine Learning and Optimal Estimation-based approaches

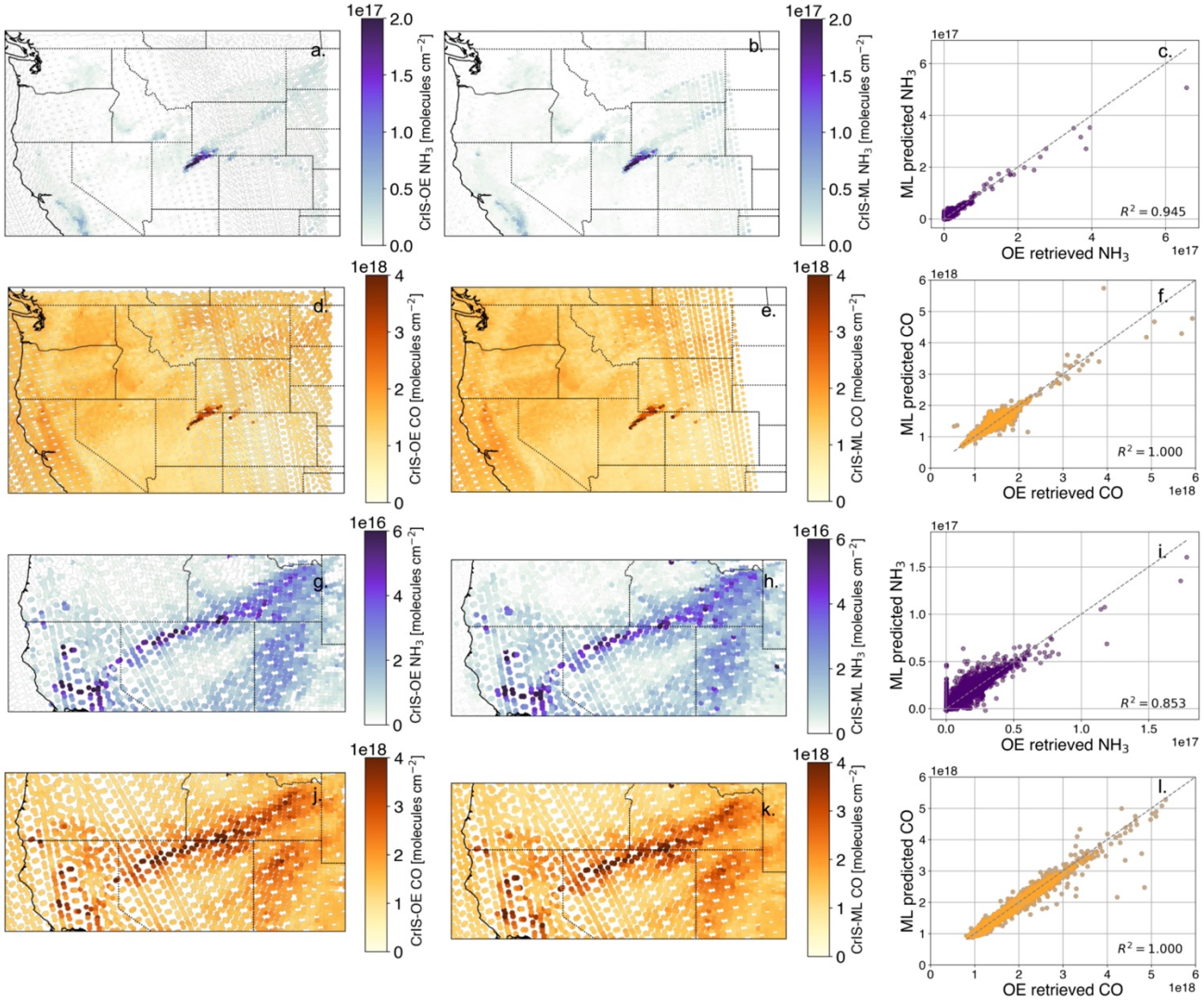

Figure 4.3: CrIS optimal estimation-based retrieval results (a, d, g, j), machine learning-based retrieval results (b, e, h, k), and scatter plots comparing the two approaches (c, f, i, l). (a-f) highlights the Pole Creek Fire plume on September 13, 2018 (35°N, 50°N, 125°W, 100°W). (g-l) highlights the Mendocino Complex Fire plume on August 3, 2018 (38°N, 45°N, 125°W, 110°W).

To evaluate consistency between retrieval methods, we compare NH_3 and CO features derived from ML-based and OE-based retrievals. Figure 4.3 presents maps and scatter plots from the S-NPP platform and shows that large-scale spatial patterns in both gases qualitatively agree across the two approaches. A similar comparison exists for the JPSS-1 platform (not shown), and we find the ML-based retrieval from JPSS-1 to be identical to the S-NPP retrieval, so we choose

to only show the S-NPP comparison here. For the ML-based retrieval, we only use daytime values where the quality flag is ≥ 0.8, denoting "there are features outside the training range, but within the extended range". We present tropospheric column values for both NH_3 and CO. For comparison, we use daytime-only OE-based retrieval footprints where the quality flag is good, and we show total column averages.

The consistency between ML-based and OE-based retrievals of NH_3 and CO for the Pole Creek Fire is illustrated by Figure 4.3, highlighting the agreement in large-scale features and downwind dilution patterns within the smoke plume, further emphasized by Figures 4.3c and 4.3f, where r^2 values between the predicted ML and retrieved OE NH_3 and CO are 0.94 and 1.0, respectively. A clear plume associated with the Pole Creek Fire in Utah (September 13, 2018) is visible in both Figures 4.3a and 4.3b. The overall large-scale features of NH_3 on this day qualitatively match between retrieval approaches, further reflected in the high r^2 values. Within the wildfire smoke plume, a clear decrease in NH_3 concentrations is observed with increasing distance from the fire centroid. The two maps in Figure 4.3a and 4.3b also show elevated NH_3 in the Snake River Valley, ID and San Joaquin Valley, CA. Similar to NH_3, the large-scale features of CO match between the retrieval approaches. Figures 4.3c and 4.3d display a similar comparison as Figures 4.3a and 4.3b, but for CO. The decrease of CO with distance as the plume dilutes with non-plume (background) air is also evident in the Pole Creek Fire plume in both the ML-based and OE-based retrievals.

While the Pole Creek Fire represents the most ideal comparison case because of the isolated nature of the plume, the ML- and OE-based retrievals are also qualitatively very similar on more complex days with multiple or extended smoke plumes. Figures 4.3g-l present a comparison of retrieval methods applied to August 3, 2018. On this day, the Mendocino

Complex Fire produced a plume that extended over a much larger spatial extent, crossing many state boundaries. The plume overlapped other regions with dilute smoke. In both NH_3 (Figure 4.3e-f) and CO (Figure 4.3g-h), the large-scale enhancements match between retrieval methods and the decay of in-plume NH_3 and CO concentrations with distance match between the methods. The correlations between methods for NH_3 is lower than that of the Pole Creek day, where $r^2 = 0.85$. The almost perfect correlation between the ML and OE approaches for CO is also evident for a larger sample of data, as shown in Werner et al., 2025.

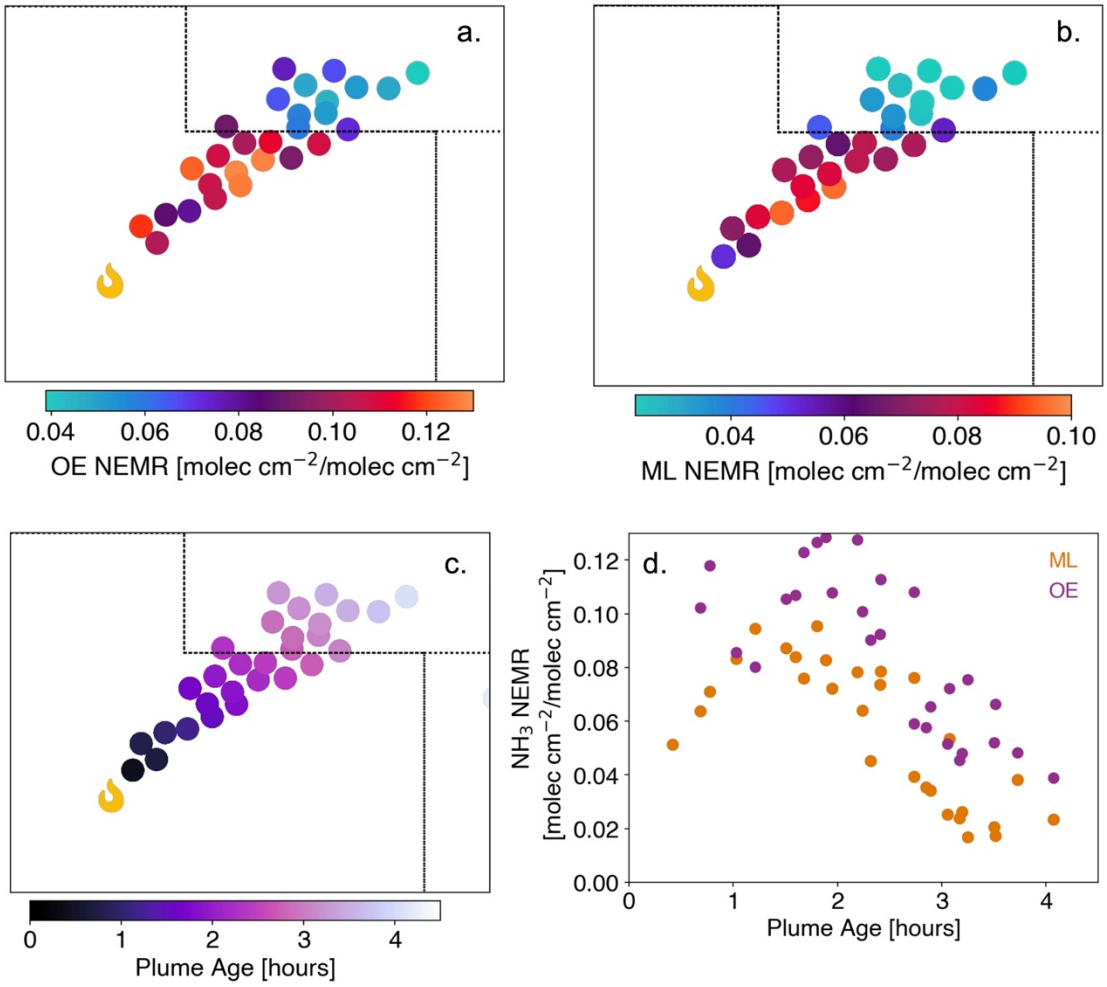

Figure 4.4. Comparison of S-NPP OE (a) and S-NPP ML (b) for the isolated Pole Creek Fire Plume, UT on Sept 13, 2018. Plume includes CrIS footprints where column CO > 2e18 molecules cm^{-2}. Panels a and b show the NEMR per CrIS footprint for the OE and ML approaches, respectively. Panel c shows approximate plume age per CrIS footprint calculated as in Chapter 3. Panel d shows how NEMR changes with plume age from the ML (orange) and OE (purple).

The Pole Creek Fire plume provides an opportunity to quantify the relationship between NH3 and other trace gases within 0 - 4 hours of transport time given its isolation (low background non-plume abundances) and high in-plume concentrations. This plume has already been used to demonstrate the ability of CrIS to detect the chemical loss of PANs and NH_3 on the scale of hours within a concentrated plume (Juncosa Calorrano et al., 2021; Shogrin et al., 2025).

We leverage this plume to compare the ML-based and OE-based approaches to evaluate the rate of loss of NH_3 in the plume.

We observe a decline of NH_3 NEMR with plume age from both retrieval approaches for the Pole Creek Fire smoke plume, and the relative rates are similar. Figure 4.4 presents a comparison of the NEMR for the S-NPP OE-based retrieval (Figure 4.4a) and the ML-based retrieval (Figure 4.4b) for the isolated Pole Creek plume on September 13, 2018. The plume was isolated using only retrievals where tropospheric column CO > 2e18 molecules cm^{-2} across both retrievals. The plume ages were calculated using a mean wind speed from Juncosa Calahorrano et al. (2021). For the NEMR calculation, in the OE-based retrieval we use a dynamic NH_3 background based on an estimate of "smoke-free" NH_3 described in Shogrin et al., 2025 and a CO background of 1.8e18 molecules cm^{-2}. In the ML-based approach, for simplicity of comparison, we estimate the NH_3 and CO background values based on the average values in the vicinity around the plume from Figure 4.3b and 4.3c; these values are ~3e16 molecules cm^{-2} and ~9e17 molecules cm^{-2}, respectively. Figure 4.4d presents the change in NEMR with plume age for both retrieval approaches. While both approaches show a general decline in NEMR with increasing plume age, the values from the ML-based retrieval tend to be lower than those in the OE-based retrieval. This is also reflected in the color bars of Figures 4.4a and 4.4b. The Pole Creek Fire plume interacted with complex terrain as it ascended and descended over the Uinta Mountains (J. Juncosa Calahorrano et al., 2026). This means that the fresher portions of the plume over Utah were located at a higher altitude than the portions of the plume to the northeast over WY. This likely introduces some height biases. The subsequent analysis instead focuses on a plume that did not interact with complex terrain, providing a clearer example of the dataset in application.

4.3.2 Machine Learning-based Plume Evolution in Individual Smoke Plumes

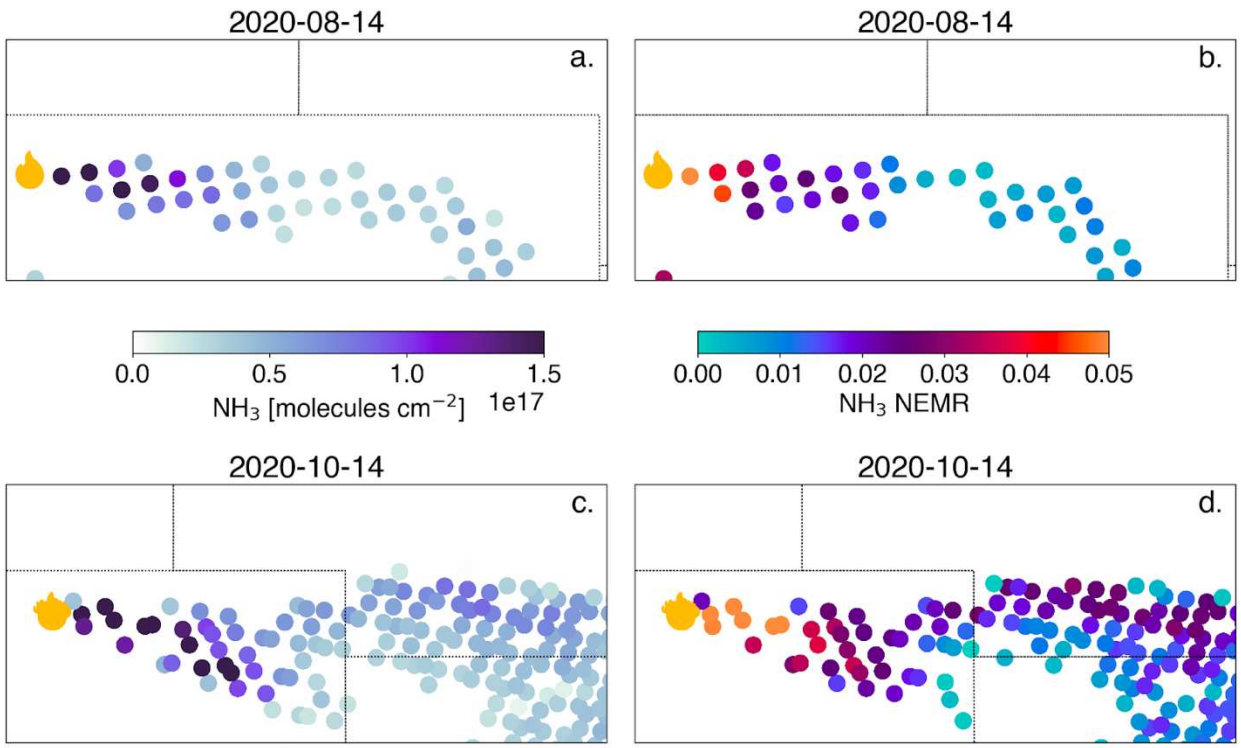

Figure 4.5: CrIS ML-based NH_3 smoke enhancements from two days of burning of the Cameron Peak fire in Northern Colorado. (a) CrIS ML-based NH_3 for the Cameron Peak Fire plume on August 14, 2020, and (b) NH_3 NEMR for August 14, 2020. (c) same as (a) but for October 14, 2020, and (d) same as (b) for October 14, 2020. Plumes have been isolated where CrIS ML-based CO > 2e18 molecules cm^{-2}.

The Cameron Peak Fire provides a valuable case study for analyzing the CrIS ML-based observations of smoke-enhanced NH_3, as its prolonged duration and multiple days of well-defined plumes offer favorable conditions for satellite-based analysis. Additionally, the smoke plume was emitted from mountainous terrain but then dispersed over the eastern Colorado plains. Thus, we anticipate less complexity in interpreting NH_3 and NH_3 NEMR values. The Cameron Peak Fire is, to date, the largest wildfire in Colorado history. Cameron Peak began on August 13, 2020, and burned for 112 days until it reached full containment on December 2, 2020. The fire

burned 208,663 acres through Arapaho and Roosevelt National forests in Larimer and Jackson Counties and through Rocky Mountain National Park. The fire exhibited rapid and sustained growth over its duration, driven by high temperatures, low humidity, and persistent high winds, with gusts reaching up to 80 mph during September and October (Wikipedia, n.d.-a). These conditions, combined with the presence of extensive drought-stricken vegetation and thousands of acres of dense beetle-kill forest, created highly flammable fuel beds.

Figure 4.5 presents two days of burning of the Cameron Peak fire, August 14 and October 14, 2020. These days were both characterized by extensive fire growth and visible smoke plumes from visible satellite imagery (VIIRS). Both smoke plumes have been isolated using only smoke-impacted retrievals (tropospheric column CO > 1.8e18 molecules cm^{-2}). We show plumes from the same fire on two different days; however, stronger 700 hPa winds on October 14 resulted in more efficient plume transport and a greater spatial extent (Figure 4.5c), whereas weaker 700 hPa winds on August 14 kept the plume largely confined within Colorado (Figure 4.5a). August 14, 2020 marked the first full day of active burning for the Cameron Peak Fire and was characterized by rapid expansion, with the fire growing from ~ 2,200 to 4,600 acres by 19:00. Figure 4.5a shows the CrIS ML-based retrieval of the fire plume on this date, with each CrIS footprint colored by predicted NH_3.

Figures 4.5c and 4.5d similarly present the CrIS-ML predicted NH_3 and NH_3 NEMR, respectively, for October 14, 2020. On this date, after 62 days of burning, the Cameron Peak Fire became the largest wildfire in Colorado history (Haggard & Paul, 2020). Rapid fire growth occurred throughout the day, with an overnight expansion of 30,000 acres, the most significant increase since early September (not shown), where the fire grew by 70,000 acres in 2 days. Easterly winds and rapid fire growth produced expansive smoke plumes visible across northern

Colorado visible in satellite imagery. As in Figure 4.5a, Figure 4.5c shows a pronounced decrease in NH_3 and Figure 4.5d shows a similar decrease in NH_3 NEMR with increasing distance from the fire source. October 14 had substantially more smoke-impacted retrievals downwind than August 14, reflecting generally smokier conditions and broader plume extent. While the NH_3 NEMR calculation method accounts for spatial variability in non-fire NH_3 emissions, the CrIS instrument lacks vertical profile information, with peak sensitivity in the lower to mid-troposphere. As a result, in regions with elevated surface NH_3 this NEMR calculation method can still induce some error, as there are many stationary agricultural NH_3 emissions in Eastern Colorado and western Nebraska.

4.4 Summary & Conclusions

We present the first analysis of novel ML-based retrievals for CrIS NH_3 and CO. Our analysis utilizes these novel retrievals to quantify the NH_3 enhancement with respect to CO in wildfire smoke plumes during an active fire year. We show the evolution of smoke-enhanced NH_3 in numerous individual smoke plumes from the ML-based data, and this work lays the groundwork for future analysis using this ML-based retrieval.

1. The ML-based algorithm approach to expanding the Optimal Estimation-based retrieval for CO and NH_3 in wildfire smoke plumes match qualitatively for smoke plumes during the 2018 wildfire season. We demonstrate this with example smoke plumes from September 13, 2018, and August 3, 2018.

2. The ML-based approach qualitatively matches the OE-based approach for the Pole Creek Fire Plume, UT on September 13, 2018 with respect to plume isolation, plume age, and

the spatial pattern of NEMR per footprint. The NH_3 NEMR calculated using the ML-based approach is overall lower in magnitude than that of the OE-based retrieval.

3. The Cameron Peak Fire plume in Colorado during fall 2020 provides an opportunity to examine this ML-based dataset in the context of a large wildfire plume. We observe clear transport of smoke-enhanced NH_3 far downwind (~280 - ~500 km) of the fire source.

4. Given this product's ability to increase the number of smoke plumes available for analysis, further work on height correction for the Standard CrIS NH_3 product is warranted and should be integrated into the ML processing pipeline.

We demonstrate the capabilities of this novel CrIS ML-based approach in capturing the NH_3 evolution in wildfire smoke plumes. We show the potential to use this dataset to explore variability in the emissions and evolution of NH_3 in individual fire plumes with relation to differences in fire and burning conditions.

CHAPTER 5

SUMMARY, CONCLUSIONS, AND FUTURE WORK

5.1 SUMMARY AND CONCLUSIONS

This dissertation presents novel satellite observations and methods for analyzing the distribution and evolution of trace gas species. We present findings about the variability in intercontinental transport and chemical evolution of trace gas species in biomass burning smoke plumes. Chapter 2 presents global observations of PANs from the CrIS instrument that serve as the first global-scale observations of PANs at this spatiotemporal scale. Chapter 3 presents the chemical evolution of NH_3 in wildfire smoke plumes and develops methods for analyzing chemical enhancements in smoke plumes from space for species with variable background sources. Building upon these methods, Chapter 4 applies a novel machine learning–based retrieval approach for CrIS, serving both to extend the analysis of smoke plume chemistry and to demonstrate a comparison between the new retrieval algorithm and the native CrIS retrievals.

In Chapter 2, we investigated the concentrations of PANs crossing Northern Hemisphere Ocean basins through new CrIS satellite observations. This study presents the first global-scale satellite observations of PANs from 2016 to 2022. PANs exhibit clear seasonal cycles, peaking in spring (MAM; Northern Hemisphere and SON; Southern Hemisphere), with elevated levels persisting through summer months. Spring and summer months are the dominant times for transpacific and transatlantic transport. Interannual variability is linked to multiple drivers, including temperature, atmospheric circulation patterns, biomass burning, and changes in anthropogenic NO_x emissions, especially during the COVID-19 pandemic. Notably, spring of 2020 saw substantial reductions in PANs and NO_2, with the most pronounced changes over the Northwest Pacific. These findings demonstrate the capability of CrIS to detect intercontinental

transport of pollutants, and these observations improve our understanding of the variability in transport.

In Chapter 3, we develop a satellite-based approach to investigate the chemical evolution of NH_3 in wildfire smoke plumes. We focus on summer 2018 in coordination with WE-CAN in situ observations. Despite strong stationary NH_3 sources, CrIS demonstrates the capability to detect smoke-enhanced NH_3 and its downwind evolution. We present a method to estimate wildfire-driven NH_3 enhancements by removing background levels using a "smoke-free" reference grid of NH_3 values, enabling more accurate normalized excess mixing ratio (NEMR) calculations. In the Pole Creek Fire plume, ~78% of smoke-enhanced NH_3 is lost within 3–4 hours, aligning with aircraft-based estimates. Over longer-lived fires like the Carr and Mendocino Complex fires, lower NH_3 NEMRs are associated with higher fire radiative power, suggesting shifts in fire behavior influence NH_3 emissions. Vertical profiling with CALIPSO supports interpretations related to aerosol partitioning. Overall, this work demonstrates that satellite data can effectively capture NH_3 loss in wildfire plumes and offers a framework applicable to other trace gas species with variable background sources.

In Chapter 4, we build on the methods developed in Chapter 3 and we focus on wildfire plumes during the summer of 2020, a time with an unprecedented number of wildfires across the CONUS. This study presents the first application of a ML-based retrieval to expand CrIS observations of NH_3 and CO in wildfire smoke plumes. The ML-based retrieval aligns well with OE-based methods, capturing plume structure, aging, and NH_3 enhancement patterns, as demonstrated with case studies from the 2018 wildfire season. Using this new dataset, we analyze NH_3 evolution in smoke from multiple 2020 fires. Across four distinct fire plumes, we observe NH_3 loss ranging from 50-97% in roughly five hours of aging. Over longer fire

lifecycles, such as the Pine Gulch Fire, we find that higher daily mean fire radiative power correlates with lower NH_3 enhancements. This work highlights the utility of ML-based CrIS retrievals for tracking NH_3 variability in smoke and provides a foundation for future studies of plume chemistry and fire behavior.

Across these three studies, we demonstrate the growing capabilities of satellite observations to track the spatiotemporal evolution of trace gases associated with anthropogenic pollution and wildfire smoke. Each of our studies highlight the complex interplay between emission sources, atmospheric chemistry, and transport dynamics involved in analyzing trace gases from pollution sources. Our studies stress the importance of continuous observations from space-based platforms, as our results would not be possible without the vantage point provided by space. Moreover, the application of machine learning-based algorithms in satellite retrievals opens new pathways for streamlining data processing and enhancing overall data coverage.

Currently, instruments like CrIS provide valuable observations once per day and once per night per location, limiting our ability to capture rapidly evolving pollution events. As satellite capabilities advance, particularly with the emergence of infrared sounders on geostationary platforms, these methods can be extended to provide near-continuous monitoring of reactive trace gases. Near continuous geostationary monitoring would enable important insights into the diurnal evolution, chemical aging, and transport of pollutants, significantly improving our ability to assess air quality and its impacts in near real-time.

The ability to observe trace gases like NH_3 and PANs from space has critical implications for air quality management, climate policy, and environmental equity. These species contribute to secondary pollutant formation, influence atmospheric radiative forcing, and reflect broader shifts in anthropogenic and natural emissions. However, spatiotemporal limitations in

monitoring, especially over oceans, rural regions, and the Global South, can obscure the full extent of pollution exposure and its consequences. By advancing methods to detect and interpret trace gases from satellite platforms, this work contributes to closing observational gaps that disproportionately affect under-monitored regions and populations. As satellite datasets and our analysis tools advance, satellite observations can serve as valuable tools for informing international air quality agreements, improving health impact assessments, and guiding future policy decisions on transboundary pollution.

5.2 Future Work

The following sections explore several possible extensions of the work detailed in this dissertation.

5.2.1 Pollution Transport

The goal of Chapter 2 was to quantify and understand the primary drivers of interannual variability in PANs crossing ocean basins. This work focused on Northern Hemisphere Ocean basins and specifically transport between Asia and North America and between North America and Europe, however, there are other regions around the globe that are major sources of intercontinental transported pollution, like west/central Europe, sub-Saharan Africa and Southern Asia (Stohl et al., 2002, 2004).

South Asia is of particular interest, as the Indian subcontinent is one of the most populous regions in the world and the population is projected to continue to increase (UN/DESA, 2023) as India outranks China for most populated country in 2023 and Delhi is projected to be the most populous city in the world by 2028 (UN/DESA, 2018). The death toll due to air pollution has risen alongside the growth of urban populations and industry in India (Balakrishnan et al., 2019;

Lelieveld et al., 2015). The Indian subcontinent region has some of the most degraded air quality in the world, with 14 out of the 15 most polluted megacities being in India (WHO, 2016). NOx emissions in many Indian megacities continue to increase due to increasing vehicle fleet in urban areas (Gurjar et al., 2016). Export of pollutants from India contribute significantly to the global burden of air pollutants (Babatola, 2018; Lelieveld et al., 2015). In-situ observations of PANs are practically absent from this area, making the use of satellite observations an essential resource for understanding this key reservoir species.

The Indian subcontinent and surrounding regions are heavily influenced by the Indian monsoon. The monsoon typically lasts from June-September with most of the rainfall occurring in July and August (Gurjar et al., 2016). Soluble gases and aerosols in ambient air are efficiently removed by monsoon rains, leaving less soluble species to be lofted into the upper troposphere via deep convection and be transported towards northern Africa and the Mediterranean (Lawrence & Lelieveld, 2010). Convective removal processes leave PANs comprising ~95% of NO_y species (Cooper & Parrish, 2004). The winter monsoon period lasts from October-April and is relatively dry with cooler temperatures, with a predominant northeasterly near-surface flow. Regional pollutants frequently form a thick haze layer during this period that spreads millions of square kilometers between southern Asia and the intertropical convergence zone (ITCZ) (Lawrence & Lelieveld, 2010). During the monsoon transition periods, flow across the Indian ocean is primarily zonal, and pollution plumes originating from both southeastern Asia and Africa spread across the Central Indian Ocean (Lawrence & Lelieveld, 2010). Seasonal biomass burning can further degrade air quality over the region in March-May and October- November and (Sahu et al., 2015; Saxena et al., 2021). In addition to PANs being transported from the polluted boundary layer to the upper troposphere via convection, PANs can also be formed in the

upper troposphere via the production of NOx from lightning (Tie et al., 2007; C. Zhao et al., 2009). Lightning activity over the Indian subcontinent peaks during the monsoon season (Penki & Kamra, 2013; Ranalkar & Chaudhari, 2009).

I hypothesize elevated PANs will be observed during the pre-monsoon and summer monsoon period over urban regions and northern India. I expect biomass burning and lightning to be important contributors to elevated PANs over and outflowing from India during their respective time periods. We expect the monsoon period to be an important time period for elevated PANs in the upper troposphere thus increasing the potential for transport. I hypothesize CrIS will detect elevated PANs within pollution plumes outflowing from the Indian subcontinent during the winter monsoon and transition time periods, however, we expect these time periods to be less important for long-range transport as the potential for lofting into the upper troposphere is decreased. I therefore expect to find lower values of PANs in the upper troposphere at these times.

The Southern Hemisphere remains understudied compared to the Northern Hemisphere. There have been a handful of studies focused on transport between South America and Africa (Edwards, Emmons, et al., 2006; Edwards, Pétron, et al., 2006; Stohl et al., 2002, 2004), however to a much less extent than the NH has gotten attention. Satellite measurements are particularly well suited for analyzing air pollution transport in the southern hemisphere as routine ground-based measurements including PANs are incredibly sparse in the SH. CrIS captures PANs moving between Africa and Australia and between South America and Africa in SON/DJF (Figure 2.1 from Chapter 2) and these transport patterns can be similarly quantified in the ways we have outlined in Chapter 2. During the 2016-2022 period, several significant events affecting the Southern Hemisphere were observed, including extreme air quality deterioration and

extensive smoke transport from the 2019/2020 Australian bushfires (Attiya & Jones, 2022; M. Li et al., 2021), record levels of biomass burning in the Amazon in 2019 (Silva et al., 2021) and in 2020 (Silveira et al., 2022), and air quality changes associated with the COVID-19 pandemic. The methods described in Chapter 2 are broadly applicable to various global regions and can be used to investigate the transport of air pollutants both into and out of continental areas.

5.2.2 Expanding fire-related analysis using ML-based data

The work presented in Chapter 4 demonstrates the first application of newly developed machine learning–based CrIS retrievals of CO and NH_3. This study highlights several potential uses of this novel dataset; however, its full range of applications remains largely unexplored.

Outside of the United States, there are many other regions with active fire seasons and intense agricultural burning activity. Prioritizing data processing in regions where frequent fire activity intersects dense population centers and agricultural productivity is important for understanding air quality and reactive nitrogen distributions. Such regions include northern India (e.g., near New Delhi), Western African nations such as Nigeria, Southeast Asia (both mainland and maritime), and eastern China, as these are all areas where large populations are routinely exposed to smoke from agricultural burning. For example, seasonal burning around New Delhi degrades air quality for tens of millions of residents between April–May and October–November (Cusworth et al., 2018; Lan et al., 2022; Saxena et al., 2021). Satellite observations from CrIS also detect increased concentrations of reactive nitrogen species such as PANs during these periods, further confirming widespread air quality degradation (M. J. Shogrin et al., 2024). Additional regions with active fire seasons include boreal forests (e.g., Canada and Siberia), tropical areas with seasonal burning (e.g., sub-Saharan Africa and the Amazon), and other fire-prone ecosystems such as the Australian bush (Attiya & Jones, 2022; M. Li et al., 2021). CrIS

ML-based data offers a valuable tool for characterizing enhancements and the chemical evolution of reactive nitrogen species in these biomass burning plumes. The following section focuses on NH_3 enhancements associated with agricultural burning in the southeastern United States.

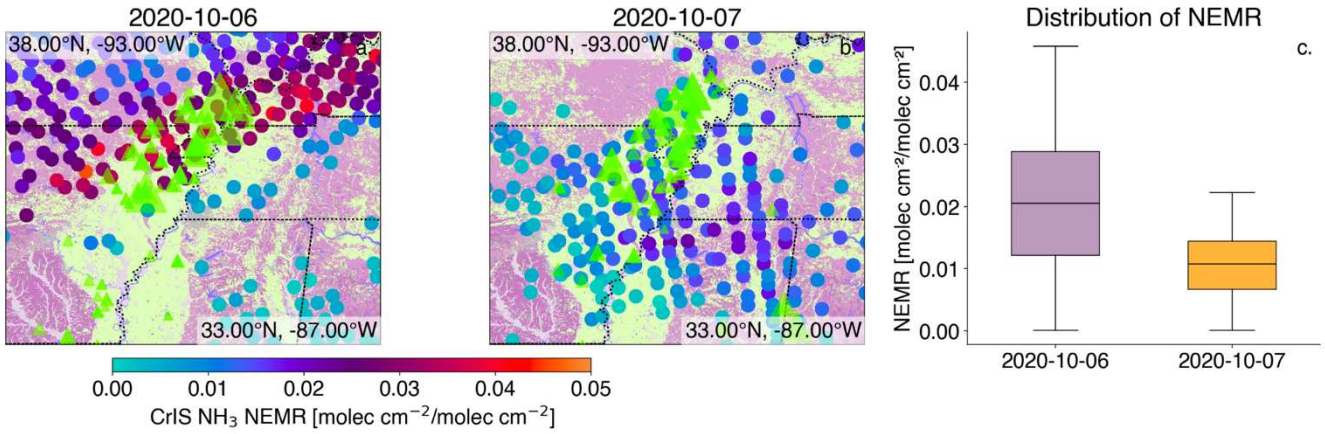

Figure 5.1: CrIS ML-based observations over the Arkansas Delta agricultural region. (a) Spatial distribution of smoke-impacted CrIS retrievals from agricultural burning on October 6, 2020, identified using retrievals where tropospheric CO > 1.9e18 molecules cm^{-2}. CrIS footprints are colored by NH_3 NEMR [molecules cm^{-2}/molecules cm^{-2}]. VIIRS active fire detections are overlaid as green triangles, scaled by relative FRP. The underlying map shows LANDSAT-based land cover classifications (from Chapter 4). (b) same as (a) but for October 7, 2020. (c) distributions of NH_3 NEMR within the respective domains from (a-b).

ML-based retrievals offer a promising avenue for studying NH_3 emissions from agricultural burning from a satellite-based perspective. Unlike wildfires, prescribed agricultural burns are typically smaller in size and can often go undetected by conventional satellite active fire detection algorithms. However, the VIIRS 375 m active fire product is capable of identifying many smaller fire hotspots associated with agricultural burning, particularly in the southeastern United States (F. Li et al., 2018; Vadrevu & Lasko, 2018; Wei et al., 2018; T. Zhang et al., 2017).

Figure 5.1 shows CrIS ML-based retrievals impacted by smoke over the Arkansas Delta agricultural region on two days in October 2020, with data colored by NH_3 NEMR. VIIRS active

fire detections are concentrated within the agricultural zone (denoted by light green on underlying maps), and smoke-impacted retrievals are spatially clustered around the VIIRS active fire detections (green triangles). On October 6 and 7, numerous active fires were detected by VIIRS in this region and smoke is evident in visible satellite imagery.

In contrast to the large-scale wildfires discussed in Chapters 3 and 4, agricultural fires tend to produce less spatially extensive and less visually distinct smoke plumes when observed from space. Instead, these smaller burns result in dense clusters of smoke-enhanced retrievals distributed across the broader burning region, as illustrated in Figures 5.1a and 5.1b. While agricultural prescribed fires typically do not generate long-range, boundary-crossing smoke plumes, they can still have substantial localized impacts, including degraded air quality, reduced visibility (Cusworth et al., 2018; Lan et al., 2022; H. Li et al., 2010; Maji et al., 2024; Pinakana et al., 2024), and adverse health effects in nearby communities (Pullabhotla & Souza, 2022; M. A. Rangel & Vogl, 2019; M. Rangel & Vogl, 2016; Sablan et al., 2024). Moreover, many of these regions lack extensive ground-based air quality monitoring networks, limiting the ability of local communities to assess their exposure to smoke-related pollutants (Sablan et al., 2024). Satellite-based quantification of emissions from these fires helps bridge these observational gaps. Additionally, characterizing the chemical composition and evolution of smoke from agricultural burning is essential for understanding both short- and long-term atmospheric and public health impacts.

REFERENCES

Abadi, M., Agarwal, A., Barham, P., Brevdo, E., Chen, Z., Citro, C., Corrado, G. S., Davis, A., Dean, J., Devin, M., Ghemawat, S., Goodfellow, I., Harp, A., Irving, G., Isard, M., Jia, Y., Jozefowicz, R., Kaiser, L., Kudlur, M., … Zheng, X. (2016). *TensorFlow: Large-Scale Machine Learning on Heterogeneous Distributed Systems* (arXiv:1603.04467). arXiv. https://doi.org/10.48550/arXiv.1603.04467

Adams, C., McLinden, C. A., Shephard, M. W., Dickson, N., Dammers, E., Chen, J., Makar, P., Cady-Pereira, K. E., Tam, N., Kharol, S. K., Lamsal, L. N., & Krotkov, N. A. (2019). Satellite-derived emissions of carbon monoxide, ammonia, and nitrogen dioxide from the 2016 Horse River wildfire in the Fort McMurray area. *Atmos. Chem. Phys.*

Altshuller, A. P. (1978). Assessment of the Contribution of Chemical Species to The Eye Irritation Potential of Photochemical Smog. *Journal of the Air Pollution Control Association*, *28*(6), 594–598. https://doi.org/10.1080/00022470.1978.10470634

Alvarado, M. J., Cady-Pereira, K. E., Xiao, Y., Millet, D. B., & Payne, V. H. (2011). Emission Ratios for Ammonia and Formic Acid and Observations of Peroxy Acetyl Nitrate (PAN) and Ethylene in Biomass Burning Smoke as Seen by the Tropospheric Emission Spectrometer (TES). *Atmosphere*, *2*(4), 633–654. https://doi.org/10.3390/atmos2040633

Ansmann, A., Baars, H., Chudnovsky, A., Mattis, I., Veselovskii, I., Haarig, M., Seifert, P., Engelmann, R., & Wandinger, U. (2018). Extreme levels of Canadian wildfire smoke in the stratosphere over central Europe on 21–22 August 2017. *Atmospheric Chemistry and Physics*, *18*(16), 11831–11845. https://doi.org/10.5194/acp-18-11831-2018

Attiya, A. A., & Jones, B. G. (2022). Impact of Smoke Plumes Transport on Air Quality in Sydney during Extensive Bushfires (2019) in New South Wales, Australia Using Remote Sensing and Ground Data. *Remote Sensing*, *14*(21), 5552. https://doi.org/10.3390/rs14215552

Auvray, M., & Bey, I. (2005). Long-range transport to Europe: Seasonal variations and implications for the European ozone budget. *Journal of Geophysical Research: Atmospheres*, *110*(D11). https://doi.org/10.1029/2004jd005503

Baars, H., Ansmann, A., Althausen, D., Engelmann, R., Artaxo, P., Pauliquevis, T., & Souza, R. (2011). Further evidence for significant smoke transport from Africa to Amazonia: AFRICAN SMOKE IN AMAZONIA. *Geophysical Research Letters*, *38*(20), n/a-n/a. https://doi.org/10.1029/2011GL049200

Babatola, S. S. (2018). Global burden of diseases attributable to air pollution. *Journal of Public Health in Africa*, *9*(3). https://doi.org/10.4081/jphia.2018.813

Balakrishnan, K., Dey, S., Gupta, T., Dhaliwal, R. S., Brauer, M., Cohen, A. J., Stanaway, J. D., Beig, G., Joshi, T. K., Aggarwal, A. N., Sabde, Y., Sadhu, H., Frostad, J., Causey, K., Godwin, W., Shukla, D. K., Kumar, G. A., Varghese, C. M., Muraleedharan, P., … Dandona, L. (2019). The impact of air pollution on deaths, disease burden, and life expectancy across the states of India: The Global Burden of Disease Study 2017. *The Lancet Planetary Health*, *3*(1), e26–e39. https://doi.org/10.1016/S2542-5196(18)30261-4

Bauwens, M., Compernolle, S., Stavrakou, T., Müller, J. -F., Gent, J., Eskes, H., Levelt, P. F., A, R., Veefkind, J. P., Vlietinck, J., Yu, H., & Zehner, C. (2020). Impact of Coronavirus

Outbreak on NO $_2$ Pollution Assessed Using TROPOMI and OMI Observations. *Geophysical Research Letters*, *47*(11). https://doi.org/10.1029/2020GL087978

Bauwens, M., Verreyken, B., Stavrakou, T., Müller, J.-F., & Smedt, I. D. (2022). Spaceborne evidence for significant anthropogenic VOC trends in Asian cities over 2005–2019. *Environmental Research Letters*, *17*(1), 015008. https://doi.org/10.1088/1748-9326/ac46eb

Behera, S. N., & Sharma, M. (2010). Investigating the potential role of ammonia in ion chemistry of fine particulate matter formation for an urban environment. *Science of The Total Environment*, *408*(17), 3569–3575. https://doi.org/10.1016/j.scitotenv.2010.04.017

Benedict, K. B., Chen, X., Sullivan, A. P., Li, Y., Day, D., Prenni, A. J., Levin, E. J. T., Kreidenweis, S. M., Malm, W. C., Schichtel, B. A., & Collett, J. L. (2013). Atmospheric concentrations and deposition of reactive nitrogen in Grand Teton National Park. *Journal of Geophysical Research: Atmospheres*, *118*(20). https://doi.org/10.1002/2013JD020394

Benedict, K. B., Prenni, A. J., Carrico, C. M., Sullivan, A. P., Schichtel, B. A., & Collett, J. L. (2017). Enhanced concentrations of reactive nitrogen species in wildfire smoke. *Atmospheric Environment*, *148*, 8–15. https://doi.org/10.1016/j.atmosenv.2016.10.030

Bey, I., Jacob, D. J., Logan, Jennifer. A., & Yantosca, R. M. (2001). Asian chemical outflow to the Pacific in spring: Origins, pathways, and budgets. *Journal of Geophysical Research: Atmospheres*, *106*(D19), 23097–23113. https://doi.org/10.1029/2001JD000806

Boersma, K. F., Eskes, H. J., Richter, A., De Smedt, I., Lorente, A., Beirle, S., van Geffen, J. H. G. M., Zara, M., Peters, E., Van Roozendael, M., Wagner, T., Maasakkers, J. D., van der A, R. J., Nightingale, J., De Rudder, A., Irie, H., Pinardi, G., Lambert, J.-C., & Compernolle, S. C. (2018). Improving algorithms and uncertainty estimates for satellite NO₂ retrievals: Results from the quality assurance for the essential climate variables (QA4ECV) project. *Atmospheric Measurement Techniques*, *11*(12), 6651–6678. https://doi.org/10.5194/amt-11-6651-2018

Boersma, K. F., Eskes, H., Richter, A., De Smedt, I., Lorente, A., Beirle, S., van Geffen, J. H. G. M., Peters, E., Van Roozendael, M., & Wagner, T. (2017). *QA4ECV NO2 tropospheric and stratospheric vertical column data from OMI (Version 1.1) [L3 Monthly Means]*. Royal Netherlands Meteorological Institute (KNMI). http://doi.org/10.21944/qa4ecv-no2-omi-v1.1

Borbon, A., Gilman, J. B., Kuster, W. C., Grand, N., Chevaillier, S., Colomb, A., Dolgorouky, C., Gros, V., Lopez, M., Sarda-Esteve, R., Holloway, J., Stutz, J., Petetin, H., McKeen, S., Beekmann, M., Warneke, C., Parrish, D. D., & de Gouw, J. A. (2013). Emission ratios of anthropogenic volatile organic compounds in northern mid-latitude megacities: Observations versus emission inventories in Los Angeles and Paris: VOC EMISSION RATIOS IN MODERN MEGACITIES. *Journal of Geophysical Research: Atmospheres*, *118*(4), 2041–2057. https://doi.org/10.1002/jgrd.50059

Bouarar, I., Wang, X., & Brasseur, G. P. (Eds.). (2017). *Air Pollution in Eastern Asia: An Integrated Perspective*. Springer International Publishing. https://doi.org/10.1007/978-3-319-59489-7

Bouwman, A. F., Lee, D. S., Asman, W. A. H., Dentener, F. J., Van Der Hoek, K. W., & Olivier, J. G. J. (1997). A global high-resolution emission inventory for ammonia. *Global Biogeochemical Cycles*, *11*(4), 561–587. https://doi.org/10.1029/97GB02266

Bowman, K. (2021a). *TROPESS CrIS-JPSS1 L2 Ammonia for Forward Processing, Standard Product V1* [Dataset]. NASA Goddard Earth Sciences Data and Information Services Center. https://doi.org/10.5067/7I3KMUCCJNEN

Bowman, K. (2021b). *TROPESS CrIS-SNPP L2 Carbon Monoxide for Forward Stream, Standard Product V1* [Dataset]. NASA Goddard Earth Sciences Data and Information Services Center. https://doi.org/10.5067/EA7G2TTV84RV

Bowman, K. W. (2021a). *TROPESS CrIS-JPSS1 L2 Carbon Monoxide for Forward Stream, Standard Product V1*. Goddard Earth Sciences Data and Information Services Center (GES DISC), Greenbelt, MD, USA. 10.5067/BYIIUV3PR9L6

Bowman, K. W. (2021b). *TROPESS CrIS-SNPP L2 Carbon Monoxide for Forward Stream, Standard Product V1*. Goddard Earth Sciences Data and Information Services Center (GES DISC), Greenbelt, MD, USA. 10.5067/EA7G2TTV84RV

Bowman, K. W. (2023). *TROPESS CrIS-SNPP L2 Peroxyacetyl Nitrate for Reanalysis Stream, Summary Product V1* (Version 1) [Dataset]. Goddard Earth Sciences Data and Information Services Center (GES DISC). https://doi.org/10.5067/VU8MI4QOA4NI

Bowman, K. W., Rodgers, C. D., Kulawik, S. S., Worden, J., Sarkissian, E., Osterman, G., Steck, T., Ming Lou, Eldering, A., Shephard, M., Worden, H., Lampel, M., Clough, S., Brown, P., Rinsland, C., Gunson, M., & Beer, R. (2006). Tropospheric emission spectrometer: Retrieval method and error analysis. *IEEE Transactions on Geoscience and Remote Sensing*, *44*(5), 1297–1307. https://doi.org/10.1109/TGRS.2006.871234

Bray, C. D., Battye, W., Aneja, V. P., Tong, D. Q., Lee, P., & Tang, Y. (2018). Ammonia emissions from biomass burning in the continental United States. *Atmospheric Environment*, *187*, 50–61. https://doi.org/10.1016/j.atmosenv.2018.05.052

Bray, C. D., Battye, W. H., Aneja, V. P., & Schlesinger, W. H. (2021). Global emissions of NH_3 , NO_x , and N_2 O from biomass burning and the impact of climate change. *Journal of the Air & Waste Management Association*, *71*(1), 102–114. https://doi.org/10.1080/10962247.2020.1842822

Brice, K. A., Bottenheim, J. W., Anlauf, K. G., & Wiebe, H. A. (1988). Long-term measurements of atmospheric peroxyacetylnitrate (PAN) at rural sites in Ontario and Nova Scotia; seasonal variations and long-range transport. *Tellus B*, *40B*(5), 408–425. https://doi.org/10.1111/j.1600-0889.1988.tb00113.x

Brown, T., Leach, S., Wachter, B., & Gardunio, B. (2020). The Extreme 2018 Northern California Fire Season. *Bulletin of the American Meteorological Society*, *101*(1), S1–S4. https://doi.org/10.1175/BAMS-D-19-0275.1

Burling, I. R., Yokelson, R. J., Akagi, S. K., Urbanski, S. P., Wold, C. E., Griffith, D. W. T., Johnson, T. J., Reardon, J., & Weise, D. R. (2011). Airborne and ground-based measurements of the trace gases and particles emitted by prescribed fires in the United States. *Atmospheric Chemistry and Physics*, *11*(23), 12197–12216. https://doi.org/10.5194/acp-11-12197-2011

Burling, I. R., Yokelson, R. J., Griffith, D. W. T., Johnson, T. J., Veres, P., Roberts, J. M., Warneke, C., Urbanski, S. P., Reardon, J., Weise, D. R., Hao, W. M., & De Gouw, J. (2010). Laboratory measurements of trace gas emissions from biomass burning of fuel types from the southeastern and southwestern United States. *Atmospheric Chemistry and Physics*, *10*(22), 11115–11130. https://doi.org/10.5194/acp-10-11115-2010

Butler, T. M., & Lawrence, M. G. (2009). The influence of megacities on global atmospheric chemistry: A modelling study. *Environmental Chemistry*, *6*(3), 219. https://doi.org/10.1071/EN08110

Butler, T., Vermeylen, F., Lehmann, C. M., Likens, G. E., & Puchalski, M. (2016). Increasing ammonia concentration trends in large regions of the USA derived from the NADP/AMoN network. *Atmospheric Environment*, *146*, 132–140. https://doi.org/10.1016/j.atmosenv.2016.06.033

Cady-Pereira, K. E., Payne, V. H., Neu, J. L., Bowman, K. W., Miyazaki, K., Marais, E. A., Kulawik, S., Tzompa-Sosa, Z. A., & Hegarty, J. D. (2017). Seasonal and spatial changes in trace gases over megacities from Aura TES observations: Two case studies. *Atmospheric Chemistry and Physics*, *17*(15), 9379–9398. https://doi.org/10.5194/acp-17-9379-2017

Canfield, D. E., Glazer, A. N., & Falkowski, P. G. (2010). The Evolution and Future of Earth's Nitrogen Cycle. *Science*, *330*(6001), 192–196. https://doi.org/10.1126/science.1186120

Cao, H., Henze, D. K., Cady-Pereira, K., McDonald, B. C., Harkins, C., Sun, K., Bowman, K. W., Fu, T.-M., & Nawaz, M. O. (2022). COVID-19 Lockdowns Afford the First Satellite-Based Confirmation That Vehicles Are an Under-recognized Source of Urban NH_3 Pollution in Los Angeles. *Environmental Science & Technology Letters*, *9*(1), 3–9. https://doi.org/10.1021/acs.estlett.1c00730

Casey, J. A., Kioumourtzoglou, M.-A., Elser, H., Walker, D., Taylor, S., Adams, S., Aguilera, R., Benmarhnia, T., & Catalano, R. (2021). Wildfire particulate matter in Shasta County, California and respiratory and circulatory disease-related emergency department visits and mortality, 2013–2018. *Environmental Epidemiology*, *5*(1), e124. https://doi.org/10.1097/EE9.0000000000000124

Chen, L.-W. A., Verburg, P., Shackelford, A., Zhu, D., Susfalk, R., Chow, J. C., & Watson, J. G. (2010). Moisture effects on carbon and nitrogen emission from burning of wildland biomass. *Atmospheric Chemistry and Physics*, *10*(14), 6617–6625. https://doi.org/10.5194/acp-10-6617-2010

Chen, Q., Zhao, Y., Zheng, B., & Zhang, L. (2025). Unexpected High Ammonia Emissions From Boreal Fires in 2021 and 2023. *Geophysical Research Letters*, *52*(4), e2024GL112396. https://doi.org/10.1029/2024GL112396

Chen, X., Day, D., Schichtel, B., Malm, W., Matzoll, A. K., Mojica, J., McDade, C. E., Hardison, E. D., Hardison, D. L., Walters, S., Van De Water, M., & Collett, J. L. (2014). Seasonal ambient ammonia and ammonium concentrations in a pilot IMPROVE NHx monitoring network in the western United States. *Atmospheric Environment*, *91*, 118–126. https://doi.org/10.1016/j.atmosenv.2014.03.058

Chollet, F. (2015). *Keras* [Computer software]. https://keras.io

Clarisse, L., Franco, B., Van Damme, M., Di Gioacchino, T., Hadji-Lazaro, J., Whitburn, S., Noppen, L., Hurtmans, D., Clerbaux, C., & Coheur, P. (2023). The IASI NH_3 version 4 product: Averaging kernels and improved consistency. *Atmospheric Measurement Techniques*, *16*(21), 5009–5028. https://doi.org/10.5194/amt-16-5009-2023

Clarisse, L., R'Honi, Y., Coheur, P.-F., Hurtmans, D., & Clerbaux, C. (2011). Thermal infrared nadir observations of 24 atmospheric gases: TRACE GAS OBSERVATIONS FROM IASI. *Geophysical Research Letters*, *38*(10), n/a-n/a. https://doi.org/10.1029/2011GL047271

Coggon, M. M., Veres, P. R., Yuan, B., Koss, A., Warneke, C., Gilman, J. B., Lerner, B. M., Peischl, J., Aikin, K. C., Stockwell, C. E., Hatch, L. E., Ryerson, T. B., Roberts, J. M., Yokelson, R. J., & De Gouw, J. A. (2016a). Emissions of nitrogen-containing organic compounds from the burning of herbaceous and arboraceous biomass: Fuel composition dependence and the variability of commonly used nitrile tracers. *Geophysical Research Letters*, *43*(18), 9903–9912. https://doi.org/10.1002/2016GL070562

Coggon, M. M., Veres, P. R., Yuan, B., Koss, A., Warneke, C., Gilman, J. B., Lerner, B. M., Peischl, J., Aikin, K. C., Stockwell, C. E., Hatch, L. E., Ryerson, T. B., Roberts, J. M., Yokelson, R. J., & De Gouw, J. A. (2016b). Emissions of nitrogen-containing organic compounds from the burning of herbaceous and arboraceous biomass: Fuel composition dependence and the variability of commonly used nitrile tracers. *Geophysical Research Letters*, *43*(18), 9903–9912. https://doi.org/10.1002/2016GL070562

Commission for Environmental Cooperation (CEC). (2023). *North American Land Cover, 2020 (Landsat, 30 m) – North American Land Change Monitoring System* (Version Edition 2.0) [Raster digital data [30-m]]. https://www.cec.org/north-american-environmental-atlas/land-cover-30m-2020/

Cooper, O. R., Forster, C., Parrish, D., Trainer, M., Dunlea, E., Ryerson, T., Hübler, G., Fehsenfeld, F., Nicks, D., Holloway, J., De Gouw, J., Warneke, C., Roberts, J. M., Flocke, F., & Moody, J. (2004). A case study of transpacific warm conveyor belt transport: Influence of merging airstreams on trace gas import to North America. *Journal of Geophysical Research: Atmospheres*, *109*(D23), 2003JD003624. https://doi.org/10.1029/2003JD003624

Cooper, O. R., & Parrish, D. D. (2004). *Air Pollution Export from and Import to North America: Experimental Evidence. In: Stohl, A. (eds) Air Pollution. 4G*(Springer, Berlin, Heidelberg). https://doi.org/10.1007/b94523

Creilson, J. K., Fishman, J., & Wozniak, A. E. (2003). Intercontinental transport of tropospheric ozone: A study of its seasonal variability across the North Atlantic utilizing tropospheric ozone residuals and its relationship to the North Atlantic Oscillation. *Atmos. Chem. Phys.*

Cusworth, D. H., Mickley, L. J., Sulprizio, M. P., Liu, T., Marlier, M. E., DeFries, R. S., Guttikunda, S. K., & Gupta, P. (2018). Quantifying the influence of agricultural fires in northwest India on urban air pollution in Delhi, India. *Environmental Research Letters*, *13*(4), 044018. https://doi.org/10.1088/1748-9326/aab303

Dammers, E., McLinden, C. A., Griffin, D., Shephard, M. W., Van Der Graaf, S., Lutsch, E., Schaap, M., Gainairu-Matz, Y., Fioletov, V., Van Damme, M., Whitburn, S., Clarisse, L., Cady-Pereira, K., Clerbaux, C., Coheur, P. F., & Erisman, J. W. (2019). NH_3 emissions from large point sources derived from CrIS and IASI satellite observations. *Atmospheric Chemistry and Physics*, *19*(19), 12261–12293. https://doi.org/10.5194/acp-19-12261-2019

Dammers, E., Shephard, M. W., Palm, M., Cady-Pereira, K., Capps, S., Lutsch, E., Strong, K., Hannigan, J. W., Ortega, I., Toon, G. C., Stremme, W., Grutter, M., Jones, N., Smale, D., Siemons, J., Hrpcek, K., Tremblay, D., Schaap, M., Notholt, J., & Erisman, J. W. (2017). Validation of the CrIS fast physical NH_3 retrieval with ground-based FTIR. *Atmospheric Measurement Techniques*, *10*(7), 2645–2667. https://doi.org/10.5194/amt-10-2645-2017

Ding, J., Van Der A, R., Eskes, H., Dammers, E., Shephard, M., Wichink Kruit, R., Guevara, M., & Tarrason, L. (2024). Ammonia emission estimates using CrIS satellite observations

over Europe. *Atmospheric Chemistry and Physics*, *24*(18), 10583–10599. https://doi.org/10.5194/acp-24-10583-2024

Duncan, B. N., Lamsal, L. N., Thompson, A. M., Yoshida, Y., Lu, Z., Streets, D. G., Hurwitz, M. M., & Pickering, K. E. (2016a). A space-based, high-resolution view of notable changes in urban NO_x pollution around the world (2005-2014): NOTABLE CHANGES IN URBAN NO_X POLLUTION. *Journal of Geophysical Research: Atmospheres*, *121*(2), 976–996. https://doi.org/10.1002/2015JD024121

Duncan, B. N., Lamsal, L. N., Thompson, A. M., Yoshida, Y., Lu, Z., Streets, D. G., Hurwitz, M. M., & Pickering, K. E. (2016b). A space-based, high-resolution view of notable changes in urban NO_x pollution around the world (2005–2014). *Journal of Geophysical Research: Atmospheres*, *121*(2), 976–996. https://doi.org/10.1002/2015JD024121

Duncan, B. N., Martin, R. V., Staudt, A. C., Yevich, R., & Logan, J. A. (2003). Interannual and seasonal variability of biomass burning emissions constrained by satellite observations. *Journal of Geophysical Research: Atmospheres*, *108*(D2). https://doi.org/10.1029/2002jd002378

Edwards, D. P., Emmons, L. K., Gille, J. C., Chu, A., Attié, J. -L., Giglio, L., Wood, S. W., Haywood, J., Deeter, M. N., Massie, S. T., Ziskin, D. C., & Drummond, J. R. (2006). Satellite-observed pollution from Southern Hemisphere biomass burning. *Journal of Geophysical Research: Atmospheres*, *111*(D14), 2005JD006655. https://doi.org/10.1029/2005JD006655

Edwards, D. P., Pétron, G., Novelli, P. C., Emmons, L. K., Gille, J. C., & Drummond, J. R. (2006). Southern Hemisphere carbon monoxide interannual variability observed by Terra/Measurement of Pollution in the Troposphere (MOPITT). *Journal of Geophysical Research: Atmospheres*, *111*(D16), 2006JD007079. https://doi.org/10.1029/2006JD007079

Erisman, J. W., Galloway, J., Seitzinger, S., Bleeker, A., & Butterbach-Bahl, K. (2011). Reactive nitrogen in the environment and its effect on climate change. *Current Opinion in Environmental Sustainability*, *3*(5), 281–290. https://doi.org/10.1016/j.cosust.2011.08.012

Feng, J., Liao, H., & Li, J. (2016). The impact of monthly variation of the Pacific–North America (PNA) teleconnection pattern on wintertime surface-layer aerosol concentrations in the United States. *Atmospheric Chemistry and Physics*, *16*(8), 4927–4943. https://doi.org/10.5194/acp-16-4927-2016

Fiore, A. M., Fischer, E. V., Milly, G. P., Pandey Deolal, S., Wild, O., Jaffe, D. A., Staehelin, J., Clifton, O. E., Bergmann, D., Collins, W., Dentener, F., Doherty, R. M., Duncan, B. N., Fischer, B., Gilge, S., Hess, P. G., Horowitz, L. W., Lupu, A., MacKenzie, I. A., … Zeng, G. (2018). Peroxy acetyl nitrate (PAN) measurements at northern midlatitude mountain sites in April: A constraint on continental source–receptor relationships. *Atmospheric Chemistry and Physics*, *18*(20), 15345–15361. https://doi.org/10.5194/acp-18-15345-2018

Fischer, E. V., Jacob, D. J., Yantosca, R. M., Sulprizio, M. P., Millet, D. B., Mao, J., Paulot, F., Singh, H. B., Roiger, A., Ries, L., Talbot, R. W., Dzepina, K., & Pandey Deolal, S. (2014). Atmospheric peroxyacetyl nitrate (PAN): A global budget and source attribution. *Atmospheric Chemistry and Physics*, *14*(5), 2679–2698. https://doi.org/10.5194/acp-14-2679-2014

Fischer, E. V., Jaffe, D. A., Reidmiller, D. R., & Jaeglé, L. (2010). Meteorological controls on observed peroxyacetyl nitrate at Mount Bachelor during the spring of 2008. *Journal of Geophysical Research*, *115*(D3), D03302. https://doi.org/10.1029/2009JD012776

Fischer, E. V., Jaffe, D. A., & Weatherhead, E. C. (2011). Free tropospheric peroxyacetyl nitrate (PAN) and ozone at Mount Bachelor: Potential causes of variability and timescale for trend detection. *Atmospheric Chemistry and Physics*, *11*(12), 5641–5654. https://doi.org/10.5194/acp-11-5641-2011

Fischer, E. V., Zhu, L., Payne, V. H., Worden, J. R., Jiang, Z., Kulawik, S. S., Brey, S., Hecobian, A., Gombos, D., Cady-Pereira, K., & Flocke, F. (2018). Using TES retrievals to investigate PAN in North American biomass burning plumes. *Atmospheric Chemistry and Physics*, *18*(8), 5639–5653. https://doi.org/10.5194/acp-18-5639-2018

Forster, C., Wandinger, U., Wotawa, G., James, P., Mattis, I., Althausen, D., Simmonds, P., O'Doherty, S., Jennings, S. G., Kleefeld, C., Schneider, J., Trickl, T., Kreipl, S., Jäger, H., & Stohl, A. (2001a). Transport of boreal forest fire emissions from Canada to Europe. *Journal of Geophysical Research: Atmospheres*, *106*(D19), 22887–22906. https://doi.org/10.1029/2001JD900115

Forster, C., Wandinger, U., Wotawa, G., James, P., Mattis, I., Althausen, D., Simmonds, P., O'Doherty, S., Jennings, S. G., Kleefeld, C., Schneider, J., Trickl, T., Kreipl, S., Jäger, H., & Stohl, A. (2001b). Transport of boreal forest fire emissions from Canada to Europe. *Journal of Geophysical Research: Atmospheres*, *106*(D19), 22887–22906. https://doi.org/10.1029/2001jd900115

Fowler, D., Pyle, J. A., Raven, J. A., & Sutton, M. A. (2013). The global nitrogen cycle in the twenty-first century: Introduction. *Philosophical Transactions of the Royal Society B: Biological Sciences*, *368*(1621), 20130165. https://doi.org/10.1098/rstb.2013.0165

Franco, B., Clarisse, L., Stavrakou, T., Müller, J. -F, Van Damme, M., Whitburn, S., Hadji-Lazaro, J., Hurtmans, D., Taraborrelli, D., Clerbaux, C., & Coheur, P. -F. (2018). A General Framework for Global Retrievals of Trace Gases From IASI: Application to Methanol, Formic Acid, and PAN. *Journal of Geophysical Research: Atmospheres*, *123*(24). https://doi.org/10.1029/2018JD029633

Fu, D., Bowman, K. W., Worden, H. M., Natraj, V., Worden, J. R., Yu, S., Veefkind, P., Aben, I., Landgraf, J., Strow, L., & Han, Y. (2016a). High-resolution tropospheric carbon monoxide profiles retrieved from CrIS and TROPOMI. *Atmospheric Measurement Techniques*, *9*(6), 2567–2579. https://doi.org/10.5194/amt-9-2567-2016

Fu, D., Bowman, K. W., Worden, H. M., Natraj, V., Worden, J. R., Yu, S., Veefkind, P., Aben, I., Landgraf, J., Strow, L., & Han, Y. (2016b). High-resolution tropospheric carbon monoxide profiles retrieved from CrIS and TROPOMI. *Atmospheric Measurement Techniques*, *9*(6), 2567–2579. https://doi.org/10.5194/amt-9-2567-2016

Fu, D., Kulawik, S. S., Miyazaki, K., Bowman, K. W., Worden, J. R., Eldering, A., Livesey, N. J., Teixeira, J., Irion, F. W., Herman, R. L., Osterman, G. B., Liu, X., Levelt, P. F., Thompson, A. M., & Luo, M. (2018). Retrievals of tropospheric ozone profiles from the synergism of AIRS and OMI: Methodology and validation. *Atmospheric Measurement Techniques*, *11*(10), 5587–5605. https://doi.org/10.5194/amt-11-5587-2018

Fu, D., Millet, D. B., Wells, K. C., Payne, V. H., Yu, S., Guenther, A., & Eldering, A. (2019). Direct retrieval of isoprene from satellite-based infrared measurements. *Nature Communications*, *10*(1), 3811. https://doi.org/10.1038/s41467-019-11835-0

Gaffney, J. S. (1999). Measurements of peroxyacyl nitrates (PANS) in Mexico City: Implications for megacity air quality impacts on regional scales&. *Atmospheric Environment*, 10.

Gaffney, J. S., Marley, N. A., & Drayton, P. J. (1986). *FAST GAS CHROMATOGRAPHY WITH LUMINOL DETECTION FOR MEASUREMENT OF NITROGEN DIOXIDE AND PANs*. 8.

Gaffney, J. S., Marley, N. A., & Prestbo, E. W. (1989). Peroxyacyl Nitrates (PANs): Their Physical and Chemical Properties. In H. Brauer, J. S. Gaffney, R. Harkov, M. A. K. Khalil, F. W. Lipfert, N. A. Marley, E. W. Prestbo, & G. E. Shaw, *Air Pollution: 4 / 4B* (pp. 1–38). Springer Berlin Heidelberg. https://doi.org/10.1007/978-3-540-46113-5_1

Galloway, J. N., Dentener, F. J., Capone, D. G., Boyer, E. W., Howarth, R. W., Seitzinger, S. P., Asner, G. P., Cleveland, C. C., Green, P. A., Holland, E. A., Karl, D. M., Michaels, A. F., Porter, J. H., Townsend, A. R., & V□osmarty, C. J. (2004). Nitrogen Cycles: Past, Present, and Future. *Biogeochemistry*, *70*(2), 153–226. https://doi.org/10.1007/s10533-004-0370-0

Georgoulias, A. K., van der A, R. J., Stammes, P., Boersma, K. F., & Eskes, H. J. (2019). Trends and trend reversal detection in 2 decades of tropospheric NO₂ satellite observations. *Atmospheric Chemistry and Physics*, *19*(9), 6269–6294. https://doi.org/10.5194/acp-19-6269-2019

Gkatzelis, G. I., Coggon, M. M., Stockwell, C. E., Hornbrook, R. S., Allen, H., Apel, E. C., Bela, M. M., Blake, D. R., Bourgeois, I., Brown, S. S., Campuzano-Jost, P., St. Clair, J. M., Crawford, J. H., Crounse, J. D., Day, D. A., DiGangi, J. P., Diskin, G. S., Fried, A., Gilman, J. B., … Warneke, C. (2024). Parameterizations of US wildfire and prescribed fire emission ratios and emission factors based on FIREX-AQ aircraft measurements. *Atmospheric Chemistry and Physics*, *24*(2), 929–956. https://doi.org/10.5194/acp-24-929-2024

Global Modeling and Assimilation Office (GMAO). (2015). *MERRA-2 tavgM_2d_slv_Nx: 2d,Monthly mean,Time-Averaged,Single-Level,Assimilation,Single-Level Diagnostics V5.12.4*. Greenbelt, MD, USA, Goddard Earth Sciences Data and Information Services Center (GES DISC). 10.5067/AP1B0BA5PD2K

Goode, J. G., Yokelson, R. J., Susott, R. A., & Ward, D. E. (1999). Trace gas emissions from laboratory biomass fires measured by open-path Fourier transform infrared spectroscopy: Fires in grass and surface fuels. *Journal of Geophysical Research: Atmospheres*, *104*(D17), 21237–21245. https://doi.org/10.1029/1999JD900360

Griffin, D., Chen, J., Anderson, K., Makar, P., McLinden, C. A., Dammers, E., & Fogal, A. (2024). Biomass burning CO emissions: Exploring insights through TROPOMI-derived emissions and emission coefficients. *Atmospheric Chemistry and Physics*, *24*(17), 10159–10186. https://doi.org/10.5194/acp-24-10159-2024

Guerova, G., Bey, I., Attié, J.-L., Martin, R. V., Cui, J., & Sprenger, M. (2006). Impact of transatlantic transport episodes on summertime ozone in Europe. *Atmospheric Chemistry and Physics*, *6*(8), 2057–2072. https://doi.org/10.5194/acp-6-2057-2006

Gurjar, B. R., Ravindra, K., & Nagpure, A. S. (2016). Air pollution trends over Indian megacities and their local-to-global implications. *Atmospheric Environment*, *142*, 475–495. https://doi.org/10.1016/j.atmosenv.2016.06.030

Haggard, L., & Paul, J. (2020, October 14). Cameron Peak fire explodes into Colorado's largest wildfire, prompting more evacuations as it nears Fort Collins. *The Colorado Sun*. https://coloradosun.com/2020/10/14/cameron-peak-fire-explodes-fort-

collins/#:~:text=The%20Cameron%20Peak%20fire%20smoke,warning%20of%20%E2%80%9Cextreme%E2%80%9D%20behavior.
Hand, J. L., Prenni, A. J., Copeland, S., Schichtel, B. A., & Malm, W. C. (2020). Thirty years of the Clean Air Act Amendments: Impacts on haze in remote regions of the United States (1990–2018). *Atmospheric Environment*, *243*, 117865. https://doi.org/10.1016/j.atmosenv.2020.117865
Heald, C. L., Jacob, D. J., Fiore, A. M., Emmons, L. K., Gille, J. C., Deeter, M. N., Warner, J., Edwards, D. P., Crawford, J. H., Hamlin, A. J., Sachse, G. W., Browell, E. V., Avery, M. A., Vay, S. A., Westberg, D. J., Blake, D. R., Singh, H. B., Sandholm, S. T., Talbot, R. W., & Fuelberg, H. E. (2003). Asian outflow and trans-Pacific transport of carbon monoxide and ozone pollution: An integrated satellite, aircraft, and model perspective. *Journal of Geophysical Research: Atmospheres*, *108*(D24), 2003JD003507. https://doi.org/10.1029/2003JD003507
Hilboll, A., Richter, A., & Burrows, J. P. (2013). Long-term changes of tropospheric NO₂ over megacities derived from multiple satellite instruments. *Atmospheric Chemistry and Physics*, *13*(8), 4145–4169. https://doi.org/10.5194/acp-13-4145-2013
Honrath, R. E., Hamlin, A. J., & Merrill, J. T. (1996). Transport of ozone precursors from the Arctic troposphere to the North Atlantic region. *Journal of Geophysical Research*, *101*(D22), 29335–29351. https://doi.org/10.1029/95JD02673
Hu, M., Chen, Y., Yuan, D., Yu, R., Lu, X., Fung, J. C. H., Chen, W., Huang, Y., & Lau, A. K. H. (2022). Estimation and Spatiotemporal Analysis of NO $_2$ Pollution in East Asia During 2001–2016. *Journal of Geophysical Research: Atmospheres*, *127*(2), e2021JD035129. https://doi.org/10.1029/2021JD035129
Huang, J., Zhou, C., Lee, X., Bao, Y., Zhao, X., Fung, J., Richter, A., Liu, X., & Zheng, Y. (2013). The effects of rapid urbanization on the levels in tropospheric nitrogen dioxide and ozone over East China. *Atmospheric Environment*, *77*, 558–567. https://doi.org/10.1016/j.atmosenv.2013.05.030
Hudman, R. C., Jacob, D. J., Cooper, O. R., Evans, M. J., Heald, C. L., Park, R. J., Fehsenfeld, F., Flocke, F., Holloway, J., Hübler, G., Kita, K., Koike, M., Kondo, Y., Neuman, A., Nowak, J., Oltmans, S., Parrish, D., Roberts, J. M., & Ryerson, T. (2004). Ozone production in transpacific Asian pollution plumes and implications for ozone air quality in California. *Journal of Geophysical Research: Atmospheres*, *109*(D23). https://doi.org/10.1029/2004jd004974
Hudman, R. C., Jacob, D. J., Turquety, S., Leibensperger, E. M., Murray, L. T., Wu, S., Gilliland, A. B., Avery, M., Bertram, T. H., Brune, W., Cohen, R. C., Dibb, J. E., Flocke, F. M., Fried, A., Holloway, J., Neuman, J. A., Orville, R., Perring, A., Ren, X., … Wooldridge, P. J. (2007). Surface and lightning sources of nitrogen oxides over the United States: Magnitudes, chemical evolution, and outflow. *Journal of Geophysical Research: Atmospheres*, *112*(D12). https://doi.org/10.1029/2006jd007912
Huntrieser, H., Heland, J., Schlager, H., Forster, C., Stohl, A., Aufmhoff, H., Arnold, F., Scheel, H. E., Campana, M., Gilge, S., Eixmann, R., & Cooper, O. (2005). Intercontinental air pollution transport from North America to Europe: Experimental evidence from airborne measurements and surface observations. *Journal of Geophysical Research: Atmospheres*, *110*(D1). https://doi.org/10.1029/2004jd005045

Ichoku, C., & Kaufman, Y. J. (2005). A method to derive smoke emission rates from MODIS fire radiative energy measurements. *IEEE Transactions on Geoscience and Remote Sensing*, *43*(11), 2636–2649. https://doi.org/10.1109/TGRS.2005.857328

Itahashi, S., Irie, H., Shimadera, H., & Chatani, S. (2022). Fifteen-Year Trends (2005–2019) in the Satellite-Derived Ozone-Sensitive Regime in East Asia: A Gradual Shift from VOC-Sensitive to NOx-Sensitive. *Remote Sensing*, *14*(18), 4512. https://doi.org/10.3390/rs14184512

Jaffe, D. (2004). Long-range transport of Siberian biomass burning emissions and impact on surface ozone in western North America. *Geophysical Research Letters*, *31*(16), L16106. https://doi.org/10.1029/2004GL020093

Jaffe, D. A., & Wigder, N. L. (2012). Ozone production from wildfires: A critical review. *Atmospheric Environment*, *51*, 1–10. https://doi.org/10.1016/j.atmosenv.2011.11.063

Jiang, Z., Worden, J. R., Payne, V. H., Zhu, L., Fischer, E., Walker, T., & Jones, D. B. A. (2016). Ozone export from East Asia: The role of PAN. *Journal of Geophysical Research: Atmospheres*, *121*(11), 6555–6563. https://doi.org/10.1002/2016JD024952

Jiang, Z., Zhu, R., Miyazaki, K., McDonald, B. C., Klimont, Z., Zheng, B., Boersma, K. F., Zhang, Q., Worden, H., Worden, J. R., Henze, D. K., Jones, D. B. A., Denier Van Der Gon, H. A. C., & Eskes, H. (2022). Decadal Variabilities in Tropospheric Nitrogen Oxides Over United States, Europe, and China. *Journal of Geophysical Research: Atmospheres*, *127*(3). https://doi.org/10.1029/2021jd035872

Johnson, M. S., Strawbridge, K., Knowland, K. E., Keller, C., & Travis, M. (2021). Long-range transport of Siberian biomass burning emissions to North America during FIREX-AQ. *Atmospheric Environment*, *252*, 118241. https://doi.org/10.1016/j.atmosenv.2021.118241

Jones, D. B. A., Bowman, K. W., Palmer, P. I., Worden, J. R., Jacob, D. J., Hoffman, R. N., Bey, I., & Yantosca, R. M. (2003). Potential of observations from the Tropospheric Emission Spectrometer to constrain continental sources of carbon monoxide. *Journal of Geophysical Research: Atmospheres*, *108*(D24), 2003JD003702. https://doi.org/10.1029/2003JD003702

Juncosa Calahorrano, J. F., Lindaas, J., O'Dell, K., Palm, B. B., Peng, Q., Flocke, F., Pollack, I. B., Garofalo, L. A., Farmer, D. K., Pierce, J. R., Collett, J. L., Weinheimer, A., Campos, T., Hornbrook, R. S., Hall, S. R., Ullmann, K., Pothier, M. A., Apel, E. C., Permar, W., … Fischer, E. V. (2021a). Daytime Oxidized Reactive Nitrogen Partitioning in Western U.S. Wildfire Smoke Plumes. *Journal of Geophysical Research: Atmospheres*, *126*(4), e2020JD033484. https://doi.org/10.1029/2020JD033484

Juncosa Calahorrano, J. F., Lindaas, J., O'Dell, K., Palm, B. B., Peng, Q., Flocke, F., Pollack, I. B., Garofalo, L. A., Farmer, D. K., Pierce, J. R., Collett, J. L., Weinheimer, A., Campos, T., Hornbrook, R. S., Hall, S. R., Ullmann, K., Pothier, M. A., Apel, E. C., Permar, W., … Fischer, E. V. (2021b). Daytime Oxidized Reactive Nitrogen Partitioning in Western U.S. Wildfire Smoke Plumes. *Journal of Geophysical Research: Atmospheres*, *126*(4), e2020JD033484. https://doi.org/10.1029/2020JD033484

Juncosa Calahorrano, J. F., Payne, V. H., Kulawik, S., Ford, B., Flocke, F., Campos, T., & Fischer, E. V. (2021). Evolution of Acyl Peroxynitrates (PANs) in Wildfire Smoke Plumes Detected by the Cross-Track Infrared Sounder (CrIS) Over the Western U.S. During Summer 2018. *Geophysical Research Letters*, *48*(23). https://doi.org/10.1029/2021GL093405

Juncosa Calahorrano, J., Millet, D. B., Wells, K. C., Hu, C., Brewer, J. F., Payne, V. H., Permar, W., Hu, L., Sullivan, A. P., Ku, I., Fischer, E. V., Selimovic, V., Sekimoto, K., Lamplugh, A., Gkatzelis, G. I., Gilman, J. B., Coggon, M. M., & Warneke, C. (2026). Tracking organic compounds in smoke plumes using infrared satellite-based measurements. *Atmospheric Chemistry and Physics*.

Kaneyasu, N., Takeuchi, K., Hayashi, M., Fujita, S., Uno, I., & Sasaki, H. (2000). Outflow patterns of pollutants from East Asia to the North Pacific in the winter monsoon. *Journal of Geophysical Research: Atmospheres*, *105*(D13), 17361–17377. https://doi.org/10.1029/2000JD900138

Karlsson, P. E., Ferm, M., Tømmervik, H., Hole, L. R., Pihl Karlsson, G., Ruoho-Airola, T., Aas, W., Hellsten, S., Akselsson, C., Mikkelsen, T. N., & Nihlgård, B. (2013). Biomass burning in eastern Europe during spring 2006 caused high deposition of ammonium in northern Fennoscandia. *Environmental Pollution*, *176*, 71–79. https://doi.org/10.1016/j.envpol.2012.12.006

Kaufman, Y. J., Justice, C. O., Flynn, L. P., Kendall, J. D., Prins, E. M., Giglio, L., Ward, D. E., Menzel, W. P., & Setzer, A. W. (1998). Potential global fire monitoring from EOS-MODIS. *Journal of Geophysical Research: Atmospheres*, *103*(D24), 32215–32238. https://doi.org/10.1029/98JD01644

Koike, M. (2003). Export of anthropogenic reactive nitrogen and sulfur compounds from the East Asia region in spring. *Journal of Geophysical Research*, *108*(D20), 8789. https://doi.org/10.1029/2002JD003284

Kopáček, J., & Posch, M. (2011). Anthropogenic nitrogen emissions during the Holocene and their possible effects on remote ecosystems: ANTHROPOGENIC N EMISSIONS IN HOLOCENE. *Global Biogeochemical Cycles*, *25*(2), n/a-n/a. https://doi.org/10.1029/2010GB003779

Kotchenruther, R. A., Jaffe, D. A., & Jaeglé, L. (2001). Ozone photochemistry and the role of peroxyacetyl nitrate in the springtime northeastern Pacific troposphere: Results from the Photochemical Ozone Budget of the Eastern North Pacific Atmosphere (PHOBEA) campaign. *Journal of Geophysical Research: Atmospheres*, *106*(D22), 28731–28742. https://doi.org/10.1029/2000jd000060

Kuhlbusch, T. A., Lobert, J. M., Crutzen, P. J., & Warneck, P. (1991). Molecular nitrogen emissions from denitrification during biomass burning. *Nature*, *351*(6322), 135–137. https://doi.org/10.1038/351135a0

Kulawik, S., & Payne, V. (2025). *TROPESS WE-CAN CrIS-Suomi-NPP observations of PAN, CO, NH3, O3, CH3OH, Tatm, H2O, HDO, CH4 for Summer, 2018 over western USA* (Versions 2025-09) [Dataset]. Zenodo. https://doi.org/10.5281/ZENODO.17065859

Lamsal, L. N., Duncan, B. N., Yoshida, Y., Krotkov, N. A., Pickering, K. E., Streets, D. G., & Lu, Z. (2015a). U.S. NO2 trends (2005–2013): EPA Air Quality System (AQS) data versus improved observations from the Ozone Monitoring Instrument (OMI). *Atmospheric Environment*, *110*, 130–143. https://doi.org/10.1016/j.atmosenv.2015.03.055

Lamsal, L. N., Duncan, B. N., Yoshida, Y., Krotkov, N. A., Pickering, K. E., Streets, D. G., & Lu, Z. (2015b). U.S. NO2 trends (2005–2013): EPA Air Quality System (AQS) data versus improved observations from the Ozone Monitoring Instrument (OMI). *Atmospheric Environment*, *110*, 130–143. https://doi.org/10.1016/j.atmosenv.2015.03.055

Lamsal, L. N., Martin, R. V., Parrish, D. D., & Krotkov, N. A. (2013). Scaling Relationship for NO_2 Pollution and Urban Population Size: A Satellite Perspective. *Environmental Science & Technology*, *47*(14), 7855–7861. https://doi.org/10.1021/es400744g

Lan, R., Eastham, S. D., Liu, T., Norford, L. K., & Barrett, S. R. H. (2022). Air quality impacts of crop residue burning in India and mitigation alternatives. *Nature Communications*, *13*(1), 6537. https://doi.org/10.1038/s41467-022-34093-z

Lang, C., Tao, S., Liu, W., Zhang, Y., & Simonich, S. (2008). Atmospheric Transport and Outflow of Polycyclic Aromatic Hydrocarbons from China. *Environmental Science & Technology*, *42*(14), 5196–5201. https://doi.org/10.1021/es800453n

Lawrence, M. G., Butler, T. M., Steinkamp, J., Gurjar, B. R., & Lelieveld, J. (2007). *Regional pollution potentials of megacities and other major population centers*. *7*, 3969–3987. https://doi.org/www.atmos-chem-phys.net/7/3969/2007/

Lawrence, M. G., & Lelieveld, J. (2010). Atmospheric pollutant outflow from southern Asia: A review. *Atmospheric Chemistry and Physics*, *10*(22), 11017–11096. https://doi.org/10.5194/acp-10-11017-2010

Lee, G., Jang, Y., Lee, H., Han, J.-S., Kim, K.-R., & Lee, M. (2008). Characteristic behavior of peroxyacetyl nitrate (PAN) in Seoul megacity, Korea. *Chemosphere*, *73*(4), 619–628. https://doi.org/10.1016/j.chemosphere.2008.05.060

Lee, J.-B., Yoon, J.-S., Jung, K., Eom, S.-W., Chae, Y.-Z., Cho, S.-J., Kim, S.-D., Sohn, J. R., & Kim, K.-H. (2013). Peroxyacetyl nitrate (PAN) in the urban atmosphere. *Chemosphere*, *93*(9), 1796–1803. https://doi.org/10.1016/j.chemosphere.2013.06.019

Lee, Y., Huey, L. G., Wang, Y., Qu, H., Zhang, R., Ji, Y., Tanner, D. J., Wang, X., Tang, J., Song, W., Hu, W., & Zhang, Y. (2021). Photochemistry of Volatile Organic Compounds in the Yellow River Delta, China: Formation of O_3 and Peroxyacyl Nitrates. *Journal of Geophysical Research: Atmospheres*, *126*(23). https://doi.org/10.1029/2021JD035296

Lelieveld, J., Evans, J. S., Fnais, M., Giannadaki, D., & Pozzer, A. (2015). The contribution of outdoor air pollution sources to premature mortality on a global scale. *Nature*, *525*(7569), 367–371. https://doi.org/10.1038/nature15371

Li, E., Pierce, J. R., Juncosa Calahorrano, J. F., Sullivan, A. P., Pollack, I. B., Roscioli, J. R., Caulton, D. R., McCabe, M. E., Jathar, S. H., & Fischer, E. V. (2024). Inorganic Nitrogen Gas-Aerosol Partitioning in and Around Animal Feeding Operations in Northeastern Colorado in Late Summer 2021. *Journal of Geophysical Research: Atmospheres*, *129*(12), e2023JD040507. https://doi.org/10.1029/2023JD040507

Li, F., Zhang, X., Kondragunta, S., & Csiszar, I. (2018). Comparison of Fire Radiative Power Estimates From VIIRS and MODIS Observations. *Journal of Geophysical Research: Atmospheres*, *123*(9), 4545–4563. https://doi.org/10.1029/2017JD027823

Li, H., Han, Z., Cheng, T., Du, H., Kong, L., Chen, J., Zhang, R., & Wang, W. (2010). Agricultural Fire Impacts on the Air Quality of Shanghai during Summer Harvesttime. *Aerosol and Air Quality Research*, *10*(2), 95–101. https://doi.org/10.4209/aaqr.2009.08.0049

Li, M., Shen, F., & Sun, X. (2021). 2019–2020 Australian bushfire air particulate pollution and impact on the South Pacific Ocean. *Scientific Reports*, *11*(1), 12288. https://doi.org/10.1038/s41598-021-91547-y

Li, Q., Jacob, D. J., Bey, I., Palmer, P. I., Duncan, B. N., Field, B. D., Martin, R. V., Fiore, A. M., Yantosca, R. M., Parrish, D. D., Simmonds, P. G., & Oltmans, S. J. (2002). Transatlantic transport of pollution and its effects on surface ozone in Europe and North

America. *Journal of Geophysical Research: Atmospheres*, *107*(D13). https://doi.org/10.1029/2001jd001422

Lin, M., Fiore, A. M., Horowitz, L. W., Cooper, O. R., Naik, V., Holloway, J., Johnson, B. J., Middlebrook, A. M., Oltmans, S. J., Pollack, I. B., Ryerson, T. B., Warner, J. X., Wiedinmyer, C., Wilson, J., & Wyman, B. (2012). Transport of Asian ozone pollution into surface air over the western United States in spring. *Journal of Geophysical Research: Atmospheres*, *117*(D21). https://doi.org/10.1029/2011jd016961

Lin, P., Aiona, P. K., Li, Y., Shiraiwa, M., Laskin, J., Nizkorodov, S. A., & Laskin, A. (2016). Molecular Characterization of Brown Carbon in Biomass Burning Aerosol Particles. *Environmental Science & Technology*, *50*(21), 11815–11824. https://doi.org/10.1021/acs.est.6b03024

Lindaas, J., Farmer, D. K., Pollack, I. B., Abeleira, A., Flocke, F., & Fischer, E. V. (2019). Acyl Peroxy Nitrates Link Oil and Natural Gas Emissions to High Ozone Abundances in the Colorado Front Range During Summer 2015. *Journal of Geophysical Research: Atmospheres*, *124*(4), 2336–2350. https://doi.org/10.1029/2018JD028825

Lindaas, J., Pollack, I. B., Calahorrano, J. J., O'Dell, K., Garofalo, L. A., Pothier, M. A., Farmer, D. K., Kreidenweis, S. M., Campos, T., Flocke, F., Weinheimer, A. J., Montzka, D. D., Tyndall, G. S., Apel, E. C., Hills, A. J., Hornbrook, R. S., Palm, B. B., Peng, Q., Thornton, J. A., … Fischer, E. V. (2021a). Empirical Insights Into the Fate of Ammonia in Western U.S. Wildfire Smoke Plumes. *Journal of Geophysical Research: Atmospheres*, *126*(11), e2020JD033730. https://doi.org/10.1029/2020JD033730

Lindaas, J., Pollack, I. B., Calahorrano, J. J., O'Dell, K., Garofalo, L. A., Pothier, M. A., Farmer, D. K., Kreidenweis, S. M., Campos, T., Flocke, F., Weinheimer, A. J., Montzka, D. D., Tyndall, G. S., Apel, E. C., Hills, A. J., Hornbrook, R. S., Palm, B. B., Peng, Q., Thornton, J. A., … Fischer, E. V. (2021b). Empirical Insights Into the Fate of Ammonia in Western U.S. Wildfire Smoke Plumes. *Journal of Geophysical Research: Atmospheres*, *126*(11), e2020JD033730. https://doi.org/10.1029/2020JD033730

Lindaas, J., Pollack, I. B., Garofalo, L. A., Pothier, M. A., Farmer, D. K., Kreidenweis, S. M., Campos, T. L., Flocke, F., Weinheimer, A. J., Montzka, D. D., Tyndall, G. S., Palm, B. B., Peng, Q., Thornton, J. A., Permar, W., Wielgasz, C., Hu, L., Ottmar, R. D., Restaino, J. C., … Fischer, E. V. (2021a). Emissions of Reactive Nitrogen From Western U.S. Wildfires During Summer 2018. *Journal of Geophysical Research: Atmospheres*, *126*(2), e2020JD032657. https://doi.org/10.1029/2020JD032657

Lindaas, J., Pollack, I. B., Garofalo, L. A., Pothier, M. A., Farmer, D. K., Kreidenweis, S. M., Campos, T. L., Flocke, F., Weinheimer, A. J., Montzka, D. D., Tyndall, G. S., Palm, B. B., Peng, Q., Thornton, J. A., Permar, W., Wielgasz, C., Hu, L., Ottmar, R. D., Restaino, J. C., … Fischer, E. V. (2021b). Emissions of Reactive Nitrogen From Western U.S. Wildfires During Summer 2018. *Journal of Geophysical Research: Atmospheres*, *126*(2), e2020JD032657. https://doi.org/10.1029/2020JD032657

Liu, Y., Stanturf, J., & Goodrick, S. (2010). Trends in global wildfire potential in a changing climate. *Forest Ecology and Management*, *259*(4), 685–697. https://doi.org/10.1016/j.foreco.2009.09.002

Luo, Z., Zhang, Y., Chen, W., Van Damme, M., Coheur, P.-F., & Clarisse, L. (2022). Estimating global ammonia (NH_3) emissions based on IASI observations from 2008 to 2018. *Atmospheric Chemistry and Physics*, *22*(15), 10375–10388. https://doi.org/10.5194/acp-22-10375-2022

Mahieu, E., Fischer, E. V., Franco, B., Palm, M., Wizenberg, T., Smale, D., Clarisse, L., Clerbaux, C., Coheur, P.-F., Hannigan, J. W., Lutsch, E., Notholt, J., Cantos, I. P., Prignon, M., Servais, C., & Strong, K. (2021). First retrievals of peroxyacetyl nitrate (PAN) from ground-based FTIR solar spectra recorded at remote sites, comparison with model and satellite data. *Elementa: Science of the Anthropocene*, *9*(1), 00027. https://doi.org/10.1525/elementa.2021.00027

Maji, K. J., Li, Z., Hu, Y., Vaidyanathan, A., Stowell, J. D., Milando, C., Wellenius, G., Kinney, P. L., Russell, A. G., & Talat Odman, M. (2024). Prescribed burn related increases of population exposure to PM2.5 and O3 pollution in the southeastern US over 2013–2020. *Environment International*, *193*, 109101. https://doi.org/10.1016/j.envint.2024.109101

McAllister, S. (2019). The Role of Fuel Bed Geometry and Wind on the Burning Rate of Porous Fuels. *Frontiers in Mechanical Engineering*, *5*, 11. https://doi.org/10.3389/fmech.2019.00011

McKee, S. (2020, August 13). *Pine Gulch Fire grows 16,000 acres, now 5th largest in Colorado history*. The Gazette. https://gazette.com/2020/08/13/pine-gulch-fire-grows-16000-acres-now-5th-largest-in-colorado-history-484c639e-dd77-11ea-ae68-9b9a5504381c/

McMeeking, G. R., Kreidenweis, S. M., Baker, S., Carrico, C. M., Chow, J. C., Collett, J. L., Hao, W. M., Holden, A. S., Kirchstetter, T. W., Malm, W. C., Moosmüller, H., Sullivan, A. P., & Wold, C. E. (2009). Emissions of trace gases and aerosols during the open combustion of biomass in the laboratory. *Journal of Geophysical Research: Atmospheres*, *114*(D19), 2009JD011836. https://doi.org/10.1029/2009JD011836

Mena-Carrasco, M., Carmichael, G. R., Campbell, J. E., Zimmerman, D., Tang, Y., Adhikary, B., D'allura, A., Molina, L. T., Zavala, M., Garcıa, A., Flocke, F., Campos, T., Weinheimer, A. J., Shetter, R., Apel, E., Montzka, D. D., Knapp, D. J., & Zheng, W. (2009). Assessing the regional impacts of Mexico City emissions on air quality and chemistry. *Atmos. Chem. Phys.*, 13.

Mesa County. (n.d.). *Pine Gulch Fire*. Retrieved https://www.mesacounty.us/departments-and-services/sheriff/divisions/emergency-services/wildland-fire-management/pine-gulch-fire

Miyazaki, K., Bowman, K., Sekiya, T., Eskes, H., Boersma, F., Worden, H., Livesey, N., Payne, V. H., Sudo, K., Kanaya, Y., Takigawa, M., & Ogochi, K. (2020). Updated tropospheric chemistry reanalysis and emission estimates, TCR-2, for 2005–2018. *Earth System Science Data*, *12*(3), 2223–2259. https://doi.org/10.5194/essd-12-2223-2020

Miyazaki, K., Bowman, K., Sekiya, T., Jiang, Z., Chen, X., Eskes, H., Ru, M., Zhang, Y., & Shindell, D. (2020). Air Quality Response in China Linked to the 2019 Novel Coronavirus (COVID-19) Lockdown. *Geophysical Research Letters*, *47*(19). https://doi.org/10.1029/2020GL089252

Miyazaki, K., Bowman, K., Sekiya, T., Takigawa, M., Neu, J. L., Sudo, K., Osterman, G., & Eskes, H. (2021). Global tropospheric ozone responses to reduced NOx emissions linked to the COVID-19 worldwide lockdowns. *SCIENCE ADVANCES*, 15.

Miyazaki, K., Eskes, H. J., & Sudo, K. (2015). A tropospheric chemistry reanalysis for the years 2005–2012 based on an assimilation of OMI, MLS, TES, and MOPITT satellite data. *Atmospheric Chemistry and Physics*, *15*(14), 8315–8348. https://doi.org/10.5194/acp-15-8315-2015

Moore, D. P., & Remedios, J. J. (2010). Seasonality of Peroxyacetyl nitrate (PAN) in the upper troposphere and lower stratosphere using the MIPAS-E instrument. *Atmospheric Chemistry and Physics*, *10*(13), 6117–6128. https://doi.org/10.5194/acp-10-6117-2010

Moxim, W. J., & Levy, H. (2000). A model analysis of the tropical South Atlantic Ocean tropospheric ozone maximum: The interaction of transport and chemistry. *Journal of Geophysical Research: Atmospheres*, *105*(D13), 17393–17415. https://doi.org/10.1029/2000jd900175

Moxim, W. J., Levy, H., & Kasibhatla, P. S. (1996). Simulated global tropospheric PAN: Its transport and impact on NO_x. *Journal of Geophysical Research: Atmospheres*, *101*(D7), 12621–12638. https://doi.org/10.1029/96jd00338

Mueller, S., Tarnay, L., O'Neill, S., & Raffuse, S. (2020). Apportioning Smoke Impacts of 2018 Wildfires on Eastern Sierra Nevada Sites. *Atmosphere*, *11*(9), 970. https://doi.org/10.3390/atmos11090970

Myhre, G., Shindell, D., Bréon, F.-M., Collins, W. J., Fuglestvedt, J., Huang, J., Koch, D., Lamarque, J.-F., Lee, D., Mendoza, B., Nakajima, T., Robock, A., Stephens, G., Takemura, T., & Zhang, H. (2013). *Climate Change 2013: The Physical Science Basis. Contribution of Working Group I to the Fifth Assessment Report of the Intergovernmental Panel on Climate Change*. Cambridge University Press. pp. 659-740

NASA. (2025, June 11). *CALIPSO – Cloud-Aerosol Lidar and Infrared Pathfinder Satellite*. https://science.nasa.gov/mission/calipso/

National Weather Service, Flagstaff AZ. (2020, June 30). *Mangum Fire 2020*. https://www.weather.gov/fgz/MangumFire2020

Odekanle, E. L., Fakinle, B. S., Odejobi, O. J., Akangbe, O. E., Sonibare, J. A., Akeredolu, F. A., & Oladoja, O. M. (2022). COVID-19 induced restriction in developing countries and its impacts on pollution load: Case study of Lagos mega city. *Heliyon*, *8*(8), e10402. https://doi.org/10.1016/j.heliyon.2022.e10402

Pan, D., Benedict, K. B., Golston, L. M., Wang, R., Collett, J. L., Tao, L., Sun, K., Guo, X., Ham, J., Prenni, A. J., Schichtel, B. A., Mikoviny, T., Müller, M., Wisthaler, A., & Zondlo, M. A. (2021). Ammonia Dry Deposition in an Alpine Ecosystem Traced to Agricultural Emission Hotpots. *Environmental Science & Technology*, *55*(12), 7776–7785. https://doi.org/10.1021/acs.est.0c05749

Pan, D., Mauzerall, D. L., Wang, R., Guo, X., Puchalski, M., Guo, Y., Song, S., Tong, D., Sullivan, A. P., Schichtel, B. A., Collett, J. L., & Zondlo, M. A. (2024). Regime shift in secondary inorganic aerosol formation and nitrogen deposition in the rural United States. *Nature Geoscience*, *17*(7), 617–623. https://doi.org/10.1038/s41561-024-01455-9

Pandey Deolal, S., Staehelin, J., Brunner, D., Cui, J., Steinbacher, M., Zellweger, C., Henne, S., & Vollmer, M. K. (2013). Transport of PAN and NOy from different source regions to the Swiss high alpine site Jungfraujoch. *Atmospheric Environment*, *64*, 103–115. https://doi.org/10.1016/j.atmosenv.2012.08.021

Paulot, F., Jacob, D. J., Pinder, R. W., Bash, J. O., Travis, K., & Henze, D. K. (2014). Ammonia emissions in the United States, European Union, and China derived by high-resolution inversion of ammonium wet deposition data: Interpretation with a new agricultural emissions inventory (MASAGE_NH3). *Journal of Geophysical Research: Atmospheres*, *119*(7), 4343–4364. https://doi.org/10.1002/2013JD021130

Paulot, F., Paynter, D., Ginoux, P., Naik, V., Whitburn, S., Van Damme, M., Clarisse, L., Coheur, P. -F., & Horowitz, L. W. (2017). Gas-aerosol partitioning of ammonia in biomass burning plumes: Implications for the interpretation of spaceborne observations of ammonia and the radiative forcing of ammonium nitrate. *Geophysical Research Letters*, *44*(15), 8084–8093. https://doi.org/10.1002/2017GL074215

Payne, V. H., Alvarado, M. J., Cady-Pereira, K. E., Worden, J. R., Kulawik, S. S., & Fischer, E. V. (2014). Satellite observations of peroxyacetyl nitrate from the Aura Tropospheric Emission Spectrometer. *Atmospheric Measurement Techniques*, *7*(11), 3737–3749. https://doi.org/10.5194/amt-7-3737-2014

Payne, V. H., Fischer, E. V., Worden, J. R., Jiang, Z., Zhu, L., Kurosu, T. P., & Kulawik, S. S. (2017). Spatial variability in tropospheric peroxyacetyl nitrate in the tropics from infrared satellite observations in 2005 and 2006. *Atmospheric Chemistry and Physics*, *17*(10), 6341–6351. https://doi.org/10.5194/acp-17-6341-2017

Payne, V. H., Kulawik, S. S., Fischer, E. V., Brewer, J. F., Huey, L. G., Miyazaki, K., Worden, J. R., Bowman, K. W., Hintsa, E. J., Moore, F., Elkins, J. W., & Juncosa Calahorrano, J. (2022). *Satellite measurements of peroxyacetyl nitrate from the Cross-Track Infrared Sounder: Comparison with ATom aircraft measurements*. Gases/Remote Sensing/Validation and Intercomparisons. https://doi.org/10.5194/amt-15-3497-2022

Penkett, S. A., & Brice, K. A. (1986). The spring maximum in photo-oxidants in the Northern Hemisphere troposphere. *Nature*, *319*(6055), 655–657. https://doi.org/10.1038/319655a0

Penki, R. K., & Kamra, A. K. (2013). Lightning distribution with respect to the monsoon trough position during the Indian summer monsoon season: LIGHTNING OVER THE MONSOON TROUGH. *Journal of Geophysical Research: Atmospheres*, *118*(10), 4780–4787. https://doi.org/10.1002/jgrd.50382

Pinakana, S. D., Raysoni, A. U., Sayeed, A., Gonzalez, J. L., Temby, O., Wladyka, D., Sepielak, K., & Gupta, P. (2024). Review of agricultural biomass burning and its impact on air quality in the continental United States of America. *Environmental Advances*, *16*, 100546. https://doi.org/10.1016/j.envadv.2024.100546

Pochanart, P., Wild, O., & Akimoto, H. (2004). Air Pollution Import to and Export from East Asia. In A. Stohl (Ed.), *Air Pollution: Intercontinental Transport of Air Pollution* (pp. 99–130). Springer Berlin Heidelberg. https://doi.org/10.1007/b94525

Pollack, I. B., Ryerson, T. B., Trainer, M., Neuman, J. A., Roberts, J. M., & Parrish, D. D. (2013). Trends in ozone, its precursors, and related secondary oxidation products in Los Angeles, California: A synthesis of measurements from 1960 to 2010: OZONE TRENDS IN LA FROM 1960 TO 2010. *Journal of Geophysical Research: Atmospheres*, *118*(11), 5893–5911. https://doi.org/10.1002/jgrd.50472

Pope, C. A., Ezzati, M., & Dockery, D. W. (2009). Fine-Particulate Air Pollution and Life Expectancy in the United States. *New England Journal of Medicine*, *360*(4), 376–386. https://doi.org/10.1056/NEJMsa0805646

Prenni, A. J., Levin, E. J. T., Benedict, K. B., Sullivan, A. P., Schurman, M. I., Gebhart, K. A., Day, D. E., Carrico, C. M., Malm, W. C., Schichtel, B. A., Collett, J. L., & Kreidenweis, S. M. (2014). Gas-phase reactive nitrogen near Grand Teton National Park: Impacts of transport, anthropogenic emissions, and biomass burning. *Atmospheric Environment*, *89*, 749–756. https://doi.org/10.1016/j.atmosenv.2014.03.017

Puchalski, M., Schwede, D., Walker, J. T., Foley, K., Lear, G., Beachley, G., & Haeuber, R. (2016). *Improved reduced nitrogen deposition estimates in the United States: Spatial variability of ammonia*.

Pullabhotla, H. K., & Souza, M. (2022). Air pollution from agricultural fires increases hypertension risk. *Journal of Environmental Economics and Management*, *115*, 102723. https://doi.org/10.1016/j.jeem.2022.102723

Qiu, Y., Ma, Z., & Li, K. (2019). A modeling study of the peroxyacetyl nitrate (PAN) during a wintertime haze event in Beijing, China. *Science of The Total Environment*, *650*, 1944–1953. https://doi.org/10.1016/j.scitotenv.2018.09.253

Qiu, Y., Ma, Z., Li, K., Huang, M., Sheng, J., Tian, P., Zhu, J., Pu, W., Tang, Y., Han, T., Zhou, H., & Liao, H. (2021). *Measurement report: Fast photochemical production of peroxyacetyl nitrate (PAN) over the rural North China Plain during cold-season haze events* [Preprint]. Gases/Field Measurements/Troposphere/Chemistry (chemical composition and reactions). https://doi.org/10.5194/acp-2021-359

Qiu, Y., Ma, Z., Li, K., Lin, W., Tang, Y., Dong, F., & Liao, H. (2020). Markedly Enhanced Levels of Peroxyacetyl Nitrate (PAN) During COVID-19 in Beijing. *Geophysical Research Letters*, *47*(19). https://doi.org/10.1029/2020GL089623

Ranalkar, M. R., & Chaudhari, H. S. (2009). Seasonal variation of lightning activity over the Indian subcontinent. *Meteorology and Atmospheric Physics*, *104*(1–2), 125–134. https://doi.org/10.1007/s00703-009-0026-7

Rangel, M. A., & Vogl, T. S. (2019). Agricultural Fires and Health at Birth. *The Review of Economics and Statistics*, *101*(4), 616–630. https://doi.org/10.1162/rest_a_00806

Rangel, M., & Vogl, T. (2016). *Agricultural Fires and Infant Health* (No. W22955; p. w22955). National Bureau of Economic Research. https://doi.org/10.3386/w22955

Rappenglück, B., Melas, D., & Fabian, P. (2003). Evidence of the impact of urban plumes on remote sites in the Eastern Mediterranean. *Atmospheric Environment*, *37*(13), 1853–1864. https://doi.org/10.1016/S1352-2310(03)00065-7

Rastigejev, Y., Park, R., Brenner, M. P., & Jacob, D. J. (2010). Resolving intercontinental pollution plumes in global models of atmospheric transport. *Journal of Geophysical Research: Atmospheres*, *115*(D2). https://doi.org/10.1029/2009jd012568

Reis, S., Pinder, R. W., Zhang, M., Lijie, G., & Sutton, M. A. (2009). Reactive nitrogen in atmospheric emission inventories. *Atmospheric Chemistry and Physics*, *9*(19), 7657–7677. https://doi.org/10.5194/acp-9-7657-2009

Revercomb, H., & Strow, L. (2018). *Suomi NPP CrIS Level 1B Full Spectral Resolution V2* [Dataset]. Goddard Earth Sciences Data and Information Services Center (GES DISC). https://doi.org/10.5067/9NPOTPIPLMAW

Ridley, B. A., Shetter, J. D., Gandrud, B. W., Salas, L. J., Singh, H. B., Carroll, M. A., Hübler, G., Albritton, D. L., Hastie, D. R., Schiff, H. I., Mackay, G. I., Karechi, D. R., Davis, D. D., Bradshaw, J. D., Rodgers, M. O., Sandholm, S. T., Torres, A. L., Condon, E. P., Gregory, G. L., & Beck, S. M. (1990). Ratios of peroxyacetyl nitrate to active nitrogen observed during aircraft flights over the eastern Pacific Oceans and continental United States. *Journal of Geophysical Research: Atmospheres*, *95*(D7), 10179–10192. https://doi.org/10.1029/jd095id07p10179

Roberts, J. M. (2007). PAN and Related Compounds. In R. Koppmann (Ed.), *Volatile Organic Compounds in the Atmosphere* (pp. 221–268). Blackwell Publishing Ltd. https://doi.org/10.1002/9780470988657.ch6

Roberts, J. M., Flocke, F., Chen, G., De Gouw, J., Holloway, J. S., Hübler, G., Neuman, J. A., Nicks, D. K., Nowak, J. B., Parrish, D. D., Ryerson, T. B., Sueper, D. T., Warneke, C., & Fehsenfeld, F. C. (2004). Measurement of peroxycarboxylic nitric anhydrides (PANs) during the ITCT 2K2 aircraft intensive experiment. *Journal of Geophysical Research: Atmospheres*, *109*(D23). https://doi.org/10.1029/2004jd004960

Roberts, J. M., Marchewka, M., Bertman, S. B., Sommariva, R., Warneke, C., De Gouw, J., Kuster, W., Goldan, P., Williams, E., Lerner, B. M., Murphy, P., & Fehsenfeld, F. C. (2007). Measurements of PANs during the New England Air Quality Study 2002. *Journal of Geophysical Research: Atmospheres*, *112*(D20), 2007JD008667. https://doi.org/10.1029/2007JD008667

Roberts, J. M., Stockwell, C. E., Yokelson, R. J., De Gouw, J., Liu, Y., Selimovic, V., Koss, A. R., Sekimoto, K., Coggon, M. M., Yuan, B., Zarzana, K. J., Brown, S. S., Santin, C., Doerr, S. H., & Warneke, C. (2020). The nitrogen budget of laboratory-simulated western US wildfires during the FIREX 2016 Fire Lab study. *Atmospheric Chemistry and Physics*, *20*(14), 8807–8826. https://doi.org/10.5194/acp-20-8807-2020

Roberts, J. M., Veres, P., Warneke, C., Neuman, J. A., Washenfelder, R. A., Brown, S. S., Baasandorj, M., Burkholder, J. B., Burling, I. R., Johnson, T. J., Yokelson, R. J., & De Gouw, J. (2010). Measurement of HONO, HNCO, and other inorganic acids by negative-ion proton-transfer chemical-ionization mass spectrometry (NI-PT-CIMS): Application to biomass burning emissions. *Atmospheric Measurement Techniques*, *3*(4), 981–990. https://doi.org/10.5194/amt-3-981-2010

Rodgers, C. D. (2000). *Inverse Methods for Atmospheric Sounding*. World Scientific Publishing Co.

Sablan, O., Ford, B., Gargulinski, E., Hammer, M. S., Henery, G., Kondragunta, S., Martin, R. V., Rosen, Z., Slater, K., Van Donkelaar, A., Zhang, H., Soja, A. J., Magzamen, S., Pierce, J. R., & Fischer, E. V. (2024). Quantifying Prescribed-Fire Smoke Exposure Using Low-Cost Sensors and Satellites: Springtime Burning in Eastern Kansas. *GeoHealth*, *8*(4), e2023GH000982. https://doi.org/10.1029/2023GH000982

Saxena, P., Sonwani, S., Srivastava, A., Jain, M., Srivastava, A., Bharti, A., Rangra, D., Mongia, N., Tejan, S., & Bhardwaj, S. (2021). Impact of crop residue burning in Haryana on the air quality of Delhi, India. *Heliyon*, *7*(5), e06973. https://doi.org/10.1016/j.heliyon.2021.e06973

Schlesinger, WilliamH., & Hartley, AnneE. (1992). A global budget for atmospheric NH3. *Biogeochemistry*, *15*(3). https://doi.org/10.1007/BF00002936

Schneider, P., Lahoz, W. A., & van der A, R. (2015). Recent satellite-based trends of tropospheric nitrogen dioxide over large urban agglomerations worldwide. *Atmospheric Chemistry and Physics*, *15*(3), 1205–1220. https://doi.org/10.5194/acp-15-1205-2015

Seinfeld, J. H. (2016). *Atmospheric Chemistry and Physics: From Air Pollution to Climate Change* (1st ed). John Wiley & Sons, Incorporated.

Sekiya, T., Miyazaki, K., Ogochi, K., Sudo, K., & Takigawa, M. (2018). Global high-resolution simulations of tropospheric nitrogen dioxide using CHASER V4.0. *Geoscientific Model Development*, *11*(3), 959–988. https://doi.org/10.5194/gmd-11-959-2018

Selimovic, V., Yokelson, R. J., Warneke, C., Roberts, J. M., De Gouw, J., Reardon, J., & Griffith, D. W. T. (2018). Aerosol optical properties and trace gas emissions by PAX and OP-FTIR for laboratory-simulated western US wildfires during FIREX. *Atmospheric Chemistry and Physics*, *18*(4), 2929–2948. https://doi.org/10.5194/acp-18-2929-2018

Shephard, M. W., & Cady-Pereira, K. E. (2015). Cross-track Infrared Sounder (CrIS) satellite observations of tropospheric ammonia. *Atmospheric Measurement Techniques*, *8*(3), 1323–1336. https://doi.org/10.5194/amt-8-1323-2015

Shephard, M. W., Cady-Pereira, K. E., Luo, M., Henze, D. K., Pinder, R. W., Walker, J. T., Rinsland, C. P., Bash, J. O., Zhu, L., Payne, V. H., & Clarisse, L. (2011). *TES ammonia*

retrieval strategy and global observations of the spatial and seasonal variability of ammonia. Gases/Remote Sensing/Troposphere/Chemistry (chemical composition and reactions). https://doi.org/10.5194/acpd-11-16023-2011

Shogrin, M. J., Payne, V. H., Kulawik, S. S., Miyazaki, K., & Fischer, E. V. (2023). Measurement report: Spatiotemporal variability of peroxy acyl nitrates (PANs) over Mexico City from TES and CrIS satellite measurements. *Atmospheric Chemistry and Physics*, *23*(4), 2667–2682. https://doi.org/10.5194/acp-23-2667-2023

Shogrin, M. J., Payne, V. H., Kulawik, S. S., Miyazaki, K., & Fischer, E. V. (2024). Changes to Peroxyacyl Nitrates (PANs) Over Megacities in Response to COVID-19 Tropospheric NO_2 Reductions Observed by the Cross-Track Infrared Sounder (CrIS). *Geophysical Research Letters*, *51*(6). https://doi.org/10.1029/2023gl104854

Shogrin, M., Payne, V. H., Kulawik, S. S., Miyazaki, K., & Fischer, E. V. (2026). Transport of Peroxyacyl Nitrates (PANs) Across Northern Hemisphere Ocean Basins From Satellite Observations. *Journal of Geophysical Research: Atmospheres*, *131*(6), e2025JD044872. https://doi.org/10.1029/2025JD044872

Sillman, S., & West, J. J. (2009). Reactive nitrogen in Mexico City and its relation to ozone-precursor sensitivity: Results from photochemical models. *Atmos. Chem. Phys.*, 13.

Silva, S. S. D., Oliveira, I., Morello, T. F., Anderson, L. O., Karlokoski, A., Brando, P. M., Melo, A. W. F. D., Costa, J. G. D., Souza, F. S. C. D., Silva, I. S. D., Nascimento, E. D. S., Pereira, M. P., Almeida, M. R. N. D., Alencar, A., Aragão, L. E. O. E. C. D., Brown, I. F., Graça, P. M. L. D. A., & Fearnside, P. M. (2021). Burning in southwestern Brazilian Amazonia, 2016–2019. *Journal of Environmental Management*, *286*, 112189. https://doi.org/10.1016/j.jenvman.2021.112189

Silveira, M. V. F., Silva-Junior, C. H. L., Anderson, L. O., & Aragão, L. E. O. C. (2022). Amazon fires in the 21st century: The year of 2020 in evidence. *Global Ecology and Biogeography*, *31*(10), 2026–2040. https://doi.org/10.1111/geb.13577

Singh, H. B., & Hanst, P. L. (1981). Peroxyacetyl nitrate (PAN) in the unpolluted atmosphere: An important reservoir for nitrogen oxides. *Geophysical Research Letters*, *8*(8), 941–944. https://doi.org/10.1029/GL008i008p00941

Singh, H. B., & Salas, L. J. (1983). Peroxyacetyl nitrate in the free troposphere. *Nature*, *302*(5906), 326–328. https://doi.org/10.1038/302326a0

Singh, H. B., Salas, L. J., & Viezee, W. (1986). Global distribution of peroxyacetyl nitrate. *Nature*, *321*(6070), 588–591. https://doi.org/10.1038/321588a0

Smith, L. E. (1965). Inhalation of the Photochemical Smog Compound Peroxyacetyl Nitrate. *American Journal of Public Health and the Nations Health*, *55*(9), 1460–1468. https://doi.org/10.2105/AJPH.55.9.1460

Stavrakou, T., Müller, J.-F., Bauwens, M., Doumbia, T., Elguindi, N., Darras, S., Granier, C., Smedt, I. D., Lerot, C., Van Roozendael, M., Franco, B., Clarisse, L., Clerbaux, C., Coheur, P.-F., Liu, Y., Wang, T., Shi, X., Gaubert, B., Tilmes, S., & Brasseur, G. (2021). Atmospheric Impacts of COVID-19 on NOx and VOC Levels over China Based on TROPOMI and IASI Satellite Data and Modeling. *Atmosphere*, *12*(8), 946. https://doi.org/10.3390/atmos12080946

Stein, A. F., Draxler, R. R., Rolph, G. D., Stunder, B. J. B., Cohen, M. D., & Ngan, F. (2015). NOAA's HYSPLIT Atmospheric Transport and Dispersion Modeling System. *Bulletin of the American Meteorological Society*, *96*(12), 2059–2077. https://doi.org/10.1175/BAMS-D-14-00110.1

Stein, L. Y., & Klotz, M. G. (2016). The nitrogen cycle. *Current Biology*, *26*(3), R94–R98. https://doi.org/10.1016/j.cub.2015.12.021

Steiner, A. L., Davis, A. J., Sillman, S., Owen, R. C., Michalak, A. M., & Fiore, A. M. (2010). Observed suppression of ozone formation at extremely high temperatures due to chemical and biophysical feedbacks. *Proceedings of the National Academy of Sciences*, *107*(46), 19685–19690. https://doi.org/10.1073/pnas.1008336107

Stock, Z. S., Russo, M. R., Butler, T. M., Archibald, A. T., Lawrence, M. G., Telford, P. J., Abraham, N. L., & Pyle, J. A. (2013). Modelling the impact of megacities on local, regional and global tropospheric ozone and the deposition of nitrogen species. *Atmospheric Chemistry and Physics*, *13*(24), 12215–12231. https://doi.org/10.5194/acp-13-12215-2013

Stockwell, C. E., Yokelson, R. J., Kreidenweis, S. M., Robinson, A. L., DeMott, P. J., Sullivan, R. C., Reardon, J., Ryan, K. C., Griffith, D. W. T., & Stevens, L. (2014). Trace gas emissions from combustion of peat, crop residue, domestic biofuels, grasses, and other fuels: Configuration and Fourier transform infrared (FTIR) component of the fourth Fire Lab at Missoula Experiment (FLAME-4). *Atmospheric Chemistry and Physics*, *14*(18), 9727–9754. https://doi.org/10.5194/acp-14-9727-2014

Stohl, A. (2001). A 1-year Lagrangian "climatology" of airstreams in the northern hemisphere troposphere and lowermost stratosphere. *Journal of Geophysical Research: Atmospheres*, *106*(D7), 7263–7279. https://doi.org/10.1029/2000JD900570

Stohl, A., Akimoto, H., & Hutzinger, O. (Eds.). (2004). *Intercontinental transport of air pollution*. Springer.

Stohl, A., Eckhardt, S., Forster, C., James, P., & Spichtinger, N. (2002). On the pathways and timescales of intercontinental air pollution transport. *Journal of Geophysical Research: Atmospheres*, *107*(D23). https://doi.org/10.1029/2001JD001396

Sudo, K., Takahashi, M., Kurokawa, J., & Akimoto, H. (2002). CHASER: A global chemical model of the troposphere 1. Model description: CHASER 1. MODEL DESCRIPTION. *Journal of Geophysical Research: Atmospheres*, *107*(D17), ACH 7-1-ACH 7-20. https://doi.org/10.1029/2001JD001113

Talbot, R. W., Dibb, J. E., Scheuer, E. M., Kondo, Y., Koike, M., Singh, H. B., Salas, L. B., Fukui, Y., Ballenthin, J. O., Meads, R. F., Miller, T. M., Hunton, D. E., Viggiano, A. A., Blake, D. R., Blake, N. J., Atlas, E., Flocke, F., Jacob, D. J., & Jaegle, L. (1999). Reactive nitrogen budget during the NASA SONEX Mission. *Geophysical Research Letters*, *26*(20), 3057–3060. https://doi.org/10.1029/1999GL900589

Thompson, C. R., Wofsy, S. C., Prather, M. J., Newman, P. A., Hanisco, T. F., Ryerson, T. B., Fahey, D. W., Apel, E. C., Brock, C. A., Brune, W. H., Froyd, K., Katich, J. M., Nicely, J. M., Peischl, J., Ray, E., Veres, P. R., Wang, S., Allen, H. M., Asher, E., … Zeng, L. (2022). The NASA Atmospheric Tomography (ATom) Mission: Imaging the Chemistry of the Global Atmosphere. *Bulletin of the American Meteorological Society*, *103*(3), E761–E790. https://doi.org/10.1175/bams-d-20-0315.1

Tie, X., Madronich, S., Li, G., Ying, Z., Zhang, R., Garcia, A. R., Lee-Taylor, J., & Liu, Y. (2007). Characterizations of chemical oxidants in Mexico City: A regional chemical dynamical model (WRF-Chem) study. *Atmospheric Environment*, *41*(9), 1989–2008. https://doi.org/10.1016/j.atmosenv.2006.10.053

Tomsche, L., Piel, F., Mikoviny, T., Nielsen, C. J., Guo, H., Campuzano-Jost, P., Nault, B. A., Schueneman, M. K., Jimenez, J. L., Halliday, H., Diskin, G., DiGangi, J. P., Nowak, J.

B., Wiggins, E. B., Gargulinski, E., Soja, A. J., & Wisthaler, A. (2023). Measurement report: Emission factors of NH_3 and NH_x for wildfires and agricultural fires in the United States. *Atmospheric Chemistry and Physics*, *23*(4), 2331–2343. https://doi.org/10.5194/acp-23-2331-2023

Trentmann, J., Yokelson, R. J., Hobbs, P. V., Winterrath, T., Christian, T. J., Andreae, M. O., & Mason, S. A. (2005). An analysis of the chemical processes in the smoke plume from a savanna fire. *Journal of Geophysical Research: Atmospheres*, *110*(D12), 2004JD005628. https://doi.org/10.1029/2004JD005628

Tyralis, H., & Papacharalampous, G. (2024). A review of predictive uncertainty estimation with machine learning. *Artificial Intelligence Review*, *57*(4), 94. https://doi.org/10.1007/s10462-023-10698-8

UN/DESA. (2018). *The World's Cities in 2018.* (World Urbanization Prospects: The 2018 Revision, 34). https://www.flickr.com/photos/thisisin%0Ahttps://www.un.org/en/events/citiesday/assets/pdf/the_worlds_cities_in_20 18_data_booklet.pdf

UN/DESA. (2023). *UN DESA Policy Brief No. 153: India overtakes China as the world's most populous country*. https://www.un.org/development/desa/dpad/publication/un-desa-policy-brief-no-153-india-overtakes-china-as-the-worlds-most-populous-country/#:~:text=Together%2C%20China%20and%20India%20are,(United%20Nations%2C%202022c).

University of Washington. (n.d.). *Smoke Emissions Reference Application (SERA)*. Retrieved https://depts.washington.edu/nwfire/sera/

Vadrevu, K., & Lasko, K. (2018). Intercomparison of MODIS AQUA and VIIRS I-Band Fires and Emissions in an Agricultural Landscape—Implications for Air Pollution Research. *Remote Sensing*, *10*(7), 978. https://doi.org/10.3390/rs10070978

Val Martin, M., Honrath, R. E., Owen, R. C., & Li, Q. B. (2008). Seasonal variation of nitrogen oxides in the central North Atlantic lower free troposphere. *Journal of Geophysical Research: Atmospheres*, *113*(D17). https://doi.org/10.1029/2007jd009688

Van Damme, M., Clarisse, L., Dammers, E., Liu, X., Nowak, J. B., Clerbaux, C., Flechard, C. R., Galy-Lacaux, C., Xu, W., Neuman, J. A., Tang, Y. S., Sutton, M. A., Erisman, J. W., & Coheur, P. F. (2015). Towards validation of ammonia (NH_3) measurements from the IASI satellite. *Atmospheric Measurement Techniques*, *8*(3), 1575–1591. https://doi.org/10.5194/amt-8-1575-2015

Van Der A, R. J., Eskes, H. J., Boersma, K. F., Van Noije, T. P. C., Van Roozendael, M., De Smedt, I., Peters, D. H. M. U., & Meijer, E. W. (2008). Trends, seasonal variability and dominant NO_x source derived from a ten year record of NO_2 measured from space. *Journal of Geophysical Research: Atmospheres*, *113*(D4), 2007JD009021. https://doi.org/10.1029/2007JD009021

Van Geffen, J., Eskes, H., Compernolle, S., Pinardi, G., Verhoelst, T., Lambert, J.-C., Sneep, M., Ter Linden, M., Ludewig, A., Boersma, K. F., & Veefkind, J. P. (2022). Sentinel-5P TROPOMI NO_2 retrieval: Impact of version v2.2 improvements and comparisons with OMI and ground-based data. *Atmospheric Measurement Techniques*, *15*(7), 2037–2060. https://doi.org/10.5194/amt-15-2037-2022

Vaughan, G., Draude, A. P., Ricketts, H. M. A., Schultz, D. M., Adam, M., Sugier, J., & Wareing, D. P. (2018). Transport of Canadian forest fire smoke over the UK as observed

by lidar. *Atmospheric Chemistry and Physics*, *18*(15), 11375–11388. https://doi.org/10.5194/acp-18-11375-2018

Venter, Z. S., Aunan, K., Chowdhury, S., & Lelieveld, J. (2020). COVID-19 lockdowns cause global air pollution declines. *Proceedings of the National Academy of Sciences*, *117*(32), 18984–18990. https://doi.org/10.1073/pnas.2006853117

Vyskocil, A., Viau, C., & Lamy, S. (1998). *Peroxyacetyl nitrate: Review of toxicity*. 212–220. https://doi.org/10.1177/096032719801700403

Walker, T. W., Martin, R. V., Van Donkelaar, A., Leaitch, W. R., MacDonald, A. M., Anlauf, K. G., Cohen, R. C., Bertram, T. H., Huey, L. G., Avery, M. A., Weinheimer, A. J., Flocke, F. M., Tarasick, D. W., Thompson, A. M., Streets, D. G., & Liu, X. (2010). Trans-Pacific transport of reactive nitrogen and ozone to Canada during spring. *Atmospheric Chemistry and Physics*, *10*(17), 8353–8372. https://doi.org/10.5194/acp-10-8353-2010

Wang, R., Guo, X., Pan, D., Kelly, J. T., Bash, J. O., Sun, K., Paulot, F., Clarisse, L., Van Damme, M., Whitburn, S., Coheur, P., Clerbaux, C., & Zondlo, M. A. (2021). Monthly Patterns of Ammonia Over the Contiguous United States at 2-km Resolution. *Geophysical Research Letters*, *48*(5), e2020GL090579. https://doi.org/10.1029/2020GL090579

Wang, S. X., Zhao, B., Cai, S. Y., Klimont, Z., Nielsen, C. P., Morikawa, T., Woo, J. H., Kim, Y., Fu, X., Xu, J. Y., Hao, J. M., & He, K. B. (2014). Emission trends and mitigation options for air pollutants in East Asia. *Atmospheric Chemistry and Physics*, *14*(13), 6571–6603. https://doi.org/10.5194/acp-14-6571-2014

Warneke, C., De Gouw, J. A., Holloway, J. S., Peischl, J., Ryerson, T. B., Atlas, E., Blake, D., Trainer, M., & Parrish, D. D. (2012). Multiyear trends in volatile organic compounds in Los Angeles, California: Five decades of decreasing emissions. *Journal of Geophysical Research: Atmospheres*, *117*(D21), 2012JD017899. https://doi.org/10.1029/2012JD017899

Watanabe, S., Hajima, T., Sudo, K., Nagashima, T., Takemura, T., Okajima, H., Nozawa, T., Kawase, H., Abe, M., Yokohata, T., Ise, T., Sato, H., Kato, E., Takata, K., Emori, S., & Kawamiya, M. (2011). MIROC-ESM 2010: Model description and basic results of CMIP5-20c3m experiments. *Geoscientific Model Development*, *4*(4), 845–872. https://doi.org/10.5194/gmd-4-845-2011

Wei, J., Sun, L., Huang, B., Bilal, M., Zhang, Z., & Wang, L. (2018). Verification, improvement and application of aerosol optical depths in China Part 1: Inter-comparison of NPP-VIIRS and Aqua-MODIS. *Atmospheric Environment*, *175*, 221–233. https://doi.org/10.1016/j.atmosenv.2017.11.048

Werner, F., Bowman, K. W., Lee, S., Laughner, J. L., Payne, V. H., & McDuffie, J. L. (2025). *A hybrid optimal estimation and machine learning approach to predict atmospheric composition*. Gases/Remote Sensing/Data Processing and Information Retrieval. https://doi.org/10.5194/egusphere-2025-4864

Werner, F., Livesey, N. J., Millán, L. F., Read, W. G., Schwartz, M. J., Wagner, P. A., Daffer, W. H., Lambert, A., Tolstoff, S. N., & Santee, M. L. (2023). Applying machine learning to improve the near-real-time products of the Aura Microwave Limb Sounder. *Atmospheric Measurement Techniques*, *16*(11), 2733–2751. https://doi.org/10.5194/amt-16-2733-2023

Werner, F., Livesey, N. J., Schwartz, M. J., Read, W. G., Santee, M. L., & Wind, G. (2021). Improved cloud detection for the Aura Microwave Limb Sounder (MLS): Training an

artificial neural network on colocated MLS and Aqua MODIS data. *Atmospheric Measurement Techniques*, *14*(12), 7749–7773. https://doi.org/10.5194/amt-14-7749-2021

WHO. (2016). *WHO Global Urban Ambient Air Pollution: A Global Assessment of Exposure and Burdon of Disease*. https://iris.who.int/bitstream/handle/10665/250141/?sequence=1

Wikipedia. (n.d.-a). *Carr Fire* [Dataset]. Retrieved https://en.wikipedia.org/wiki/Carr_Fire

Wikipedia. (n.d.-b). *Mendocino Complex Fire* [Dataset]. Retrieved https://en.wikipedia.org/wiki/Mendocino_Complex_Fire

Wikipedia. (n.d.-c). *Pine Gulch Fire*. Retrieved https://en.wikipedia.org/wiki/Pine_Gulch_Fire

Winker, D. (2023). *CALIPSO Lidar Level 2 Vertical Feature Mask (VFM), V4-51* [Dataset]. NASA Langley Atmospheric Science Data Center Distributed Active Archive Center. https://doi.org/10.5067/CALIOP/CALIPSO/CAL_LID_L2_VFM-STANDARD-V4-51

Wolfe, G. M., Thornton, J. A., McNeill, V. F., Jaffe, D. A., Reidmiller, D., Chand, D., Smith, J., Swartzendruber, P., Flocke, F., & Zheng, W. (2007). Influence of trans-Pacific pollution transport on acyl peroxy nitrate abundances and speciation at Mount Bachelor Observatory during INTEX-B. *Atmos. Chem. Phys.*

Worden, H. M., Francis, G. L., Kulawik, S. S., Bowman, K. W., Cady-Pereira, K., Fu, D., Hegarty, J. D., Kantchev, V., Luo, M., Payne, V. H., Worden, J. R., Commane, R., & McKain, K. (2022). *TROPESS/CrIS carbon monoxide profile validation with NOAA GML and ATom in situ aircraft observations* [Preprint]. Gases/Remote Sensing/Validation and Intercomparisons. https://doi.org/10.5194/amt-2022-128

Xian, P., Reid, J. S., Atwood, S. A., Johnson, R. S., Hyer, E. J., Westphal, D. L., & Sessions, W. (2013). Smoke aerosol transport patterns over the Maritime Continent. *Atmospheric Research*, *122*, 469–485. https://doi.org/10.1016/j.atmosres.2012.05.006

Yokelson, R. J., Andreae, M. O., & Akagi, S. K. (2013). Pitfalls with the use of enhancement ratios or normalized excess mixing ratios measured in plumes to characterize pollution sources and aging. *Atmospheric Measurement Techniques*, *6*(8), 2155–2158. https://doi.org/10.5194/amt-6-2155-2013

Yokelson, R. J., Crounse, J. D., DeCarlo, P. F., Karl, T., Urbanski, S., Atlas, E., Campos, T., Shinozuka, Y., Kapustin, V., Clarke, A. D., Weinheimer, A., Knapp, D. J., Montzka, D. D., Holloway, J., Weibring, P., Flocke, F., Zheng, W., Toohey, D., Wennberg, P. O., … Shetter, R. (2009). Emissions from biomass burning in the Yucatan. *Atmos. Chem. Phys.*, 28.

Yokelson, R. J., Griffith, D. W. T., & Ward, D. E. (1996). Open-path Fourier transform infrared studies of large-scale laboratory biomass fires. *Journal of Geophysical Research: Atmospheres*, *101*(D15), 21067–21080. https://doi.org/10.1029/96JD01800

Yokelson, R. J., Susott, R., Ward, D. E., Reardon, J., & Griffith, D. W. T. (1997). Emissions from smoldering combustion of biomass measured by open-path Fourier transform infrared spectroscopy. *Journal of Geophysical Research: Atmospheres*, *102*(D15), 18865–18877. https://doi.org/10.1029/97JD00852

Zaveri, R. A. (2003). Ozone production efficiency and NO_x depletion in an urban plume: Interpretation of field observations and implications for evaluating O_3-NO_x-VOC sensitivity. *Journal of Geophysical Research*, *108*(D14), 4436. https://doi.org/10.1029/2002JD003144

Zavyalov, V., Esplin, M., Scott, D., Esplin, B., Bingham, G., Hoffman, E., Lietzke, C., Predina, J., Frain, R., Suwinski, L., Han, Y., Major, C., Graham, B., & Phillips, L. (2013). Noise

performance of the CrIS instrument. *Journal of Geophysical Research: Atmospheres*, *118*(23). https://doi.org/10.1002/2013JD020457

Zhai, S., Jacob, D. J., Franco, B., Clarisse, L., Coheur, P., Shah, V., Bates, K. H., Lin, H., Dang, R., Sulprizio, M. P., Huey, L. G., Moore, F. L., Jaffe, D. A., & Liao, H. (2024). Transpacific Transport of Asian Peroxyacetyl Nitrate (PAN) Observed from Satellite: Implications for Ozone. *Environmental Science & Technology*, *58*(22), 9760–9769. https://doi.org/10.1021/acs.est.4c01980

Zhang, G., Mu, Y., Zhou, L., Zhang, C., Zhang, Y., Liu, J., Fang, S., & Yao, B. (2015). Summertime distributions of peroxyacetyl nitrate (PAN) and peroxypropionyl nitrate (PPN) in Beijing: Understanding the sources and major sink of PAN. *Atmospheric Environment*, *103*, 289–296. https://doi.org/10.1016/j.atmosenv.2014.12.035

Zhang, H., Xu, X., Lin, W., & Wang, Y. (2014). Wintertime peroxyacetyl nitrate (PAN) in the megacity Beijing: Role of photochemical and meteorological processes. *Journal of Environmental Sciences*, *26*(1), 83–96. https://doi.org/10.1016/S1001-0742(13)60384-8

Zhang, L., Jacob, D. J., Boersma, K. F., Jaffe, D. A., Olson, J. R., Bowman, K. W., Worden, J. R., Thompson, A. M., Avery, M. A., Cohen, R. C., Dibb, J. E., Flock, F. M., Fuelberg, H. E., Huey, L. G., McMillan, W. W., Singh, H. B., & Weinheimer, A. J. (2008). Transpacific transport of ozone pollution and the effect of recent Asian emission increases on air quality in North America: An integrated analysis using satellite, aircraft, ozonesonde, and surface observations. *Atmos. Chem. Phys.*

Zhang, Q., Wang, Y., Xiao, Q., Geng, G., Davis, S. J., Liu, X., Yang, J., Liu, J., Huang, W., He, C., Luo, B., Martin, R. V., Brauer, M., Randerson, J. T., & He, K. (2025). Long-range PM2.5 pollution and health impacts from the 2023 Canadian wildfires. *Nature*, *645*(8081), 672–678. https://doi.org/10.1038/s41586-025-09482-1

Zhang, T., Wooster, M. J., & Xu, W. (2017). Approaches for synergistically exploiting VIIRS I- and M-Band data in regional active fire detection and FRP assessment: A demonstration with respect to agricultural residue burning in Eastern China. *Remote Sensing of Environment*, *198*, 407–424. https://doi.org/10.1016/j.rse.2017.06.028

Zhao, B., Wang, S. X., Liu, H., Xu, J. Y., Fu, K., Klimont, Z., Hao, J. M., He, K. B., Cofala, J., & Amann, M. (2013). NO_x emissions in China: Historical trends and future perspectives. *Atmospheric Chemistry and Physics*, *13*(19), 9869–9897. https://doi.org/10.5194/acp-13-9869-2013

Zhao, C., Wang, Y., Choi, Y., & Zeng, T. (2009). Summertime impact of convective transport and lightning NO_x production over North America: Modeling dependence on meteorological simulations. *Atmospheric Chemistry and Physics*, *9*(13), 4315–4327. https://doi.org/10.5194/acp-9-4315-2009

Zheng, B., Tong, D., Li, M., Liu, F., Hong, C., Geng, G., Li, H., Li, X., Peng, L., Qi, J., Yan, L., Zhang, Y., Zhao, H., Zheng, Y., He, K., & Zhang, Q. (2018). Trends in China's anthropogenic emissions since 2010 as the consequence of clean air actions. *Atmospheric Chemistry and Physics*, *18*(19), 14095–14111. https://doi.org/10.5194/acp-18-14095-2018

Zhu, L., Fischer, E. V., Payne, V. H., Worden, J. R., & Jiang, Z. (2015a). TES observations of the interannual variability of PAN over Northern Eurasia and the relationship to springtime fires. *Geophysical Research Letters*, *42*(17), 7230–7237. https://doi.org/10.1002/2015GL065328

Zhu, L., Fischer, E. V., Payne, V. H., Worden, J. R., & Jiang, Z. (2015b). TES observations of the interannual variability of PAN over Northern Eurasia and the relationship to springtime fires. *Geophysical Research Letters*, *42*(17), 7230–7237. https://doi.org/10.1002/2015GL065328

Zhu, L., Payne, V. H., Walker, T. W., Worden, J. R., Jiang, Z., Kulawik, S. S., & Fischer, E. V. (2017). PAN in the eastern Pacific free troposphere: A satellite view of the sources, seasonality, interannual variability, and timeline for trend detection. *Journal of Geophysical Research: Atmospheres*, *122*(6), 3614–3629. https://doi.org/10.1002/2016JD025868

Ziemke, J. R., Kramarova, N. A., Frith, S. M., Huang, L., Haffner, D. P., Wargan, K., Lamsal, L. N., Labow, G. J., McPeters, R. D., & Bhartia, P. K. (2022). NASA Satellite Measurements Show Global-Scale Reductions in Free Tropospheric Ozone in 2020 and Again in 2021 During COVID-19. *Geophysical Research Letters*, *49*(15). https://doi.org/10.1029/2022gl098712

APPENDIX A1

SUPPLEMENTAL INFORMATION FOR CHAPTER 2

Introduction

This Appendix provides additional figures and statistical results referenced in Chapter 2. Included are extended visualizations of carbon monoxide (CO) distributions and North Atlantic Oscillation (NAO) Index values for selected time periods discussed in Chapter 2.

To evaluate interannual differences in CrIS observations of PANs, we conducted a one-way ANOVA with post-hoc pairwise comparisons across three defined periods: “pre-COVID”, “COVID”, “post-COVID”. This analysis assesses whether the distributions of PANs values differ significantly between defined time periods and individual years independent of each temporal grouping.

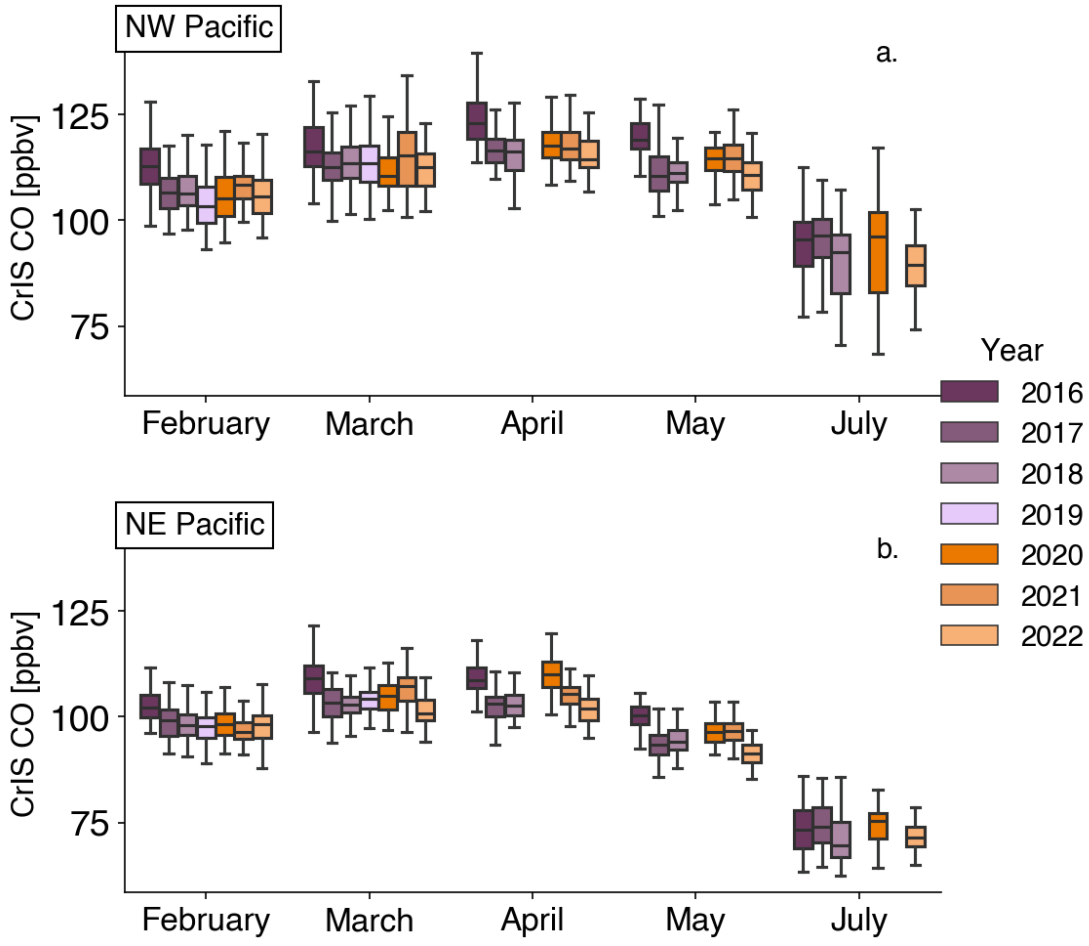

Figure A1.1: CrIS CO gridded monthly mean distribution within the respective boxes denoted in Figure 1. The months shown are the months with interannual variability over the Pacific Ocean

basin boxes, with the addition of July. Hue difference represents pre-COVID and post-COVID time periods. The extent of the boxes represents the 25th and 75th percentile, the median is shown by the line in the center, and the extents of the whiskers represent the 5th and 95th percentile. Outliers in data are not shown.

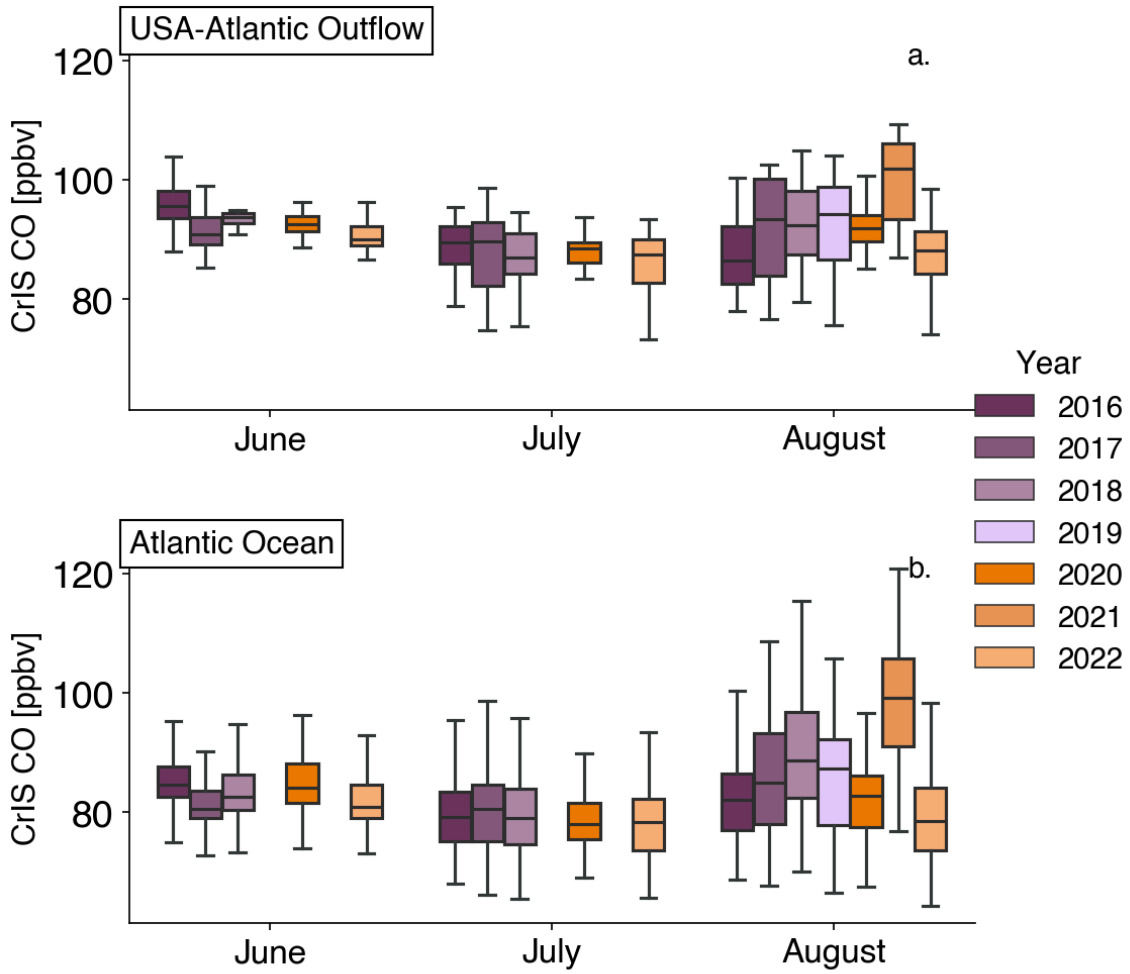

Figure A1.2: CrIS CO gridded monthly mean distribution within the respective boxes denoted in Figure 1. The months shown are the months with interannual variability over the Atlantic Ocean basin boxes. Hue difference represents pre-COVID and post-COVID time periods. The extent of the boxes represents the 25th and 75th percentile, the median is shown by the line in the center, and the extents of the whiskers represent the 5th and 95th percentile. Outliers in data are not

shown.

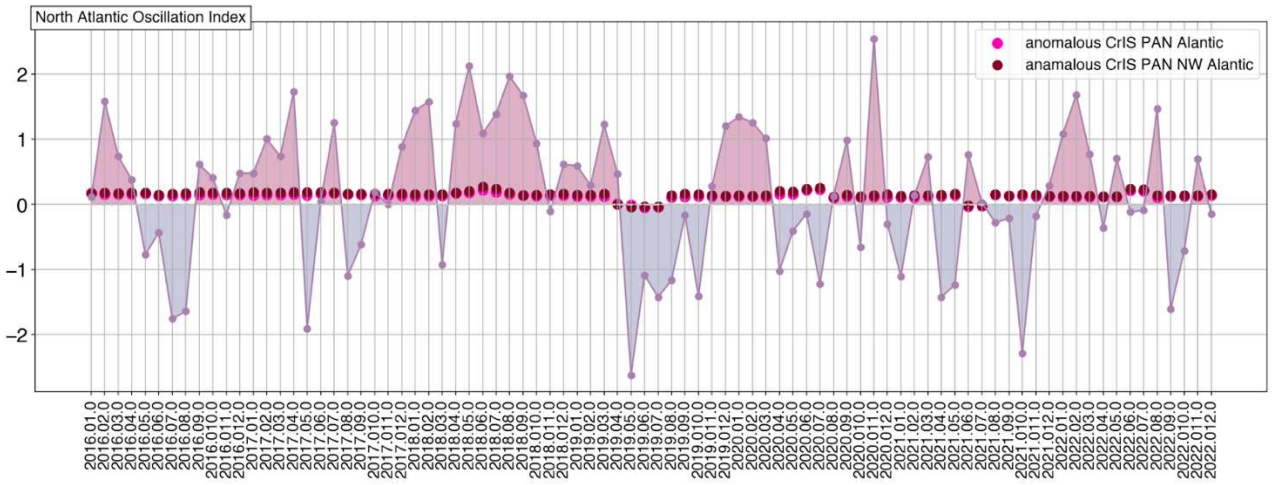

Figure A1.3: Values of the North Atlantic Oscillation Index from January 2016 to December 2022 (purple line), shading indicates phase (positive: red; negative: blue). "Anomalous" values of CrIS PAN are shown as burgundy and pink dots and represents deseasonalized values. Deseasonalization was performed using STL (Seasonal-Trend decomposition using Loess), which separates the time series into trend, seasonal, and residual components; the deseasonalized series is the sum of the trend and residual, without the seasonal component.

NW Pacific pairwise ANOVA

Year 1	Year 2	P-value
2016.0	2017.0	0.023047
2016.0	2018.0	0.232854
2016.0	2019.0	0.0
2016.0	2020.0	0.0
2016.0	2021.0	0.000132
2016.0	2022.0	3.7e-05
2017.0	2018.0	0.245501
2017.0	2019.0	0.0
2017.0	2020.0	0.003688
2017.0	2021.0	0.114129
2017.0	2022.0	0.060441
2018.0	2019.0	0.0
2018.0	2020.0	3.4e-05
2018.0	2021.0	0.005323
2018.0	2022.0	0.001926
2019.0	2020.0	0.000923
2019.0	2021.0	1.4e-05
2019.0	2022.0	3.1e-05
2020.0	2021.0	0.183947
2020.0	2022.0	0.293566
2021.0	2022.0	0.773424

Table A1.1: P-values for the NW Pacific from a pairwise ANOVA test. Years that are statistically different ($p < 0.05$) are highlighted in purple.

NE Pacific pairwise ANOVA

Year 1	Year 2	P-value
2016.0	2017.0	0.068151
2016.0	2018.0	0.002738
2016.0	2019.0	0.0
2016.0	2020.0	9.2e-05
2016.0	2021.0	0.000321
2016.0	2022.0	0.0
2017.0	2018.0	0.175074
2017.0	2019.0	0.0
2017.0	2020.0	0.02473
2017.0	2021.0	0.046604
2017.0	2022.0	0.000454
2018.0	2019.0	0.000105
2018.0	2020.0	0.438602
2018.0	2021.0	0.549043
2018.0	2022.0	0.06018
2019.0	2020.0	0.000615
2019.0	2021.0	0.000791
2019.0	2022.0	0.006954
2020.0	2021.0	0.880743
2020.0	2022.0	0.26189
2021.0	2022.0	0.220027

Table A1.2: P-values for the NE Pacific from a pairwise ANOVA test. Years that are statistically different ($p < 0.05$) are highlighted in purple.

NW Atlantic pairwise ANOVA

Year 1	Year 2	P-value
2016.0	2017.0	0.973061
2016.0	2018.0	0.008258
2016.0	2019.0	0.140688
2016.0	2020.0	0.003837
2016.0	2021.0	0.109584
2016.0	2022.0	0.000419
2017.0	2018.0	0.009751
2017.0	2019.0	0.173593
2017.0	2020.0	0.005963
2017.0	2021.0	0.137909
2017.0	2022.0	0.000813
2018.0	2019.0	0.001634
2018.0	2020.0	0.0
2018.0	2021.0	0.001216
2018.0	2022.0	0.0
2019.0	2020.0	0.485582
2019.0	2021.0	0.88365
2019.0	2022.0	0.251596
2020.0	2021.0	0.596613
2020.0	2022.0	0.62855
2021.0	2022.0	0.341696

Table A1.3: P-values for the USA-Atlantic outflow region (NW Atlantic) from a pairwise ANOVA test. Years that are statistically different ($p < 0.05$) are highlighted in purple for months

June, July and August.

JUNE Atlantic pairwise ANOVA

Year 1	Year 2	P-value
2016.0	2017.0	0.049433
2016.0	2018.0	0.0
2016.0	2019.0	nan
2016.0	2020.0	0.719745
2016.0	2021.0	nan
2016.0	2022.0	0.694107
2017.0	2018.0	1e-06
2017.0	2019.0	nan
2017.0	2020.0	0.022988
2017.0	2021.0	nan
2017.0	2022.0	0.015475
2018.0	2019.0	nan
2018.0	2020.0	0.0
2018.0	2021.0	nan
2018.0	2022.0	0.0
2019.0	2020.0	nan
2019.0	2021.0	nan
2019.0	2022.0	nan
2020.0	2021.0	nan
2020.0	2022.0	0.991826
2021.0	2022.0	nan

Table A1.4: P-values for the USA-Atlantic outflow region (NW Atlantic) from a pairwise ANOVA test. Years that are statistically different ($p < 0.05$) are highlighted in purple for June.

JULY Atlantic pairwise ANOVA

Year 1	Year 2	P-value
2016.0	2017.0	0.223998
2016.0	2018.0	0.227231
2016.0	2019.0	nan
2016.0	2020.0	0.000276
2016.0	2021.0	nan
2016.0	2022.0	0.0
2017.0	2018.0	0.015331
2017.0	2019.0	nan
2017.0	2020.0	1e-06
2017.0	2021.0	nan
2017.0	2022.0	0.0
2018.0	2019.0	nan
2018.0	2020.0	0.017199
2018.0	2021.0	nan
2018.0	2022.0	3e-06
2019.0	2020.0	nan
2019.0	2021.0	nan
2019.0	2022.0	nan
2020.0	2021.0	nan
2020.0	2022.0	0.015709
2021.0	2022.0	nan

Table A1.5: P-values for the USA-Atlantic outflow region (NW Atlantic) from a pairwise ANOVA test. Years that are statistically different ($p < 0.05$) are highlighted in purple for July.

AUGUST Atlantic pairwise ANOVA

Year 1	Year 2	P-value
2016.0	2017.0	0.001454
2016.0	2018.0	1e-06
2016.0	2019.0	0.075685
2016.0	2020.0	2e-06
2016.0	2021.0	0.000446
2016.0	2022.0	0.0
2017.0	2018.0	0.162205
2017.0	2019.0	3.1e-05
2017.0	2020.0	0.0
2017.0	2021.0	0.860898
2017.0	2022.0	0.0
2018.0	2019.0	0.0
2018.0	2020.0	0.0
2018.0	2021.0	0.083208
2018.0	2022.0	0.0
2019.0	2020.0	0.023308
2019.0	2021.0	7e-06
2019.0	2022.0	5e-06
2020.0	2021.0	0.0
2020.0	2022.0	0.005145
2021.0	2022.0	0.0

Table A1.6: P-values for the USA-Atlantic outflow region (NW Atlantic) from a pairwise ANOVA test. Years that are statistically different ($p < 0.05$) are highlighted in purple for August.

APPENDIX A2

SUPPLEMENTAL INFORMATION FOR CHAPTER 3

This Appendix provides additional figures and HYSPLIT model runs referenced in Chapter 3.

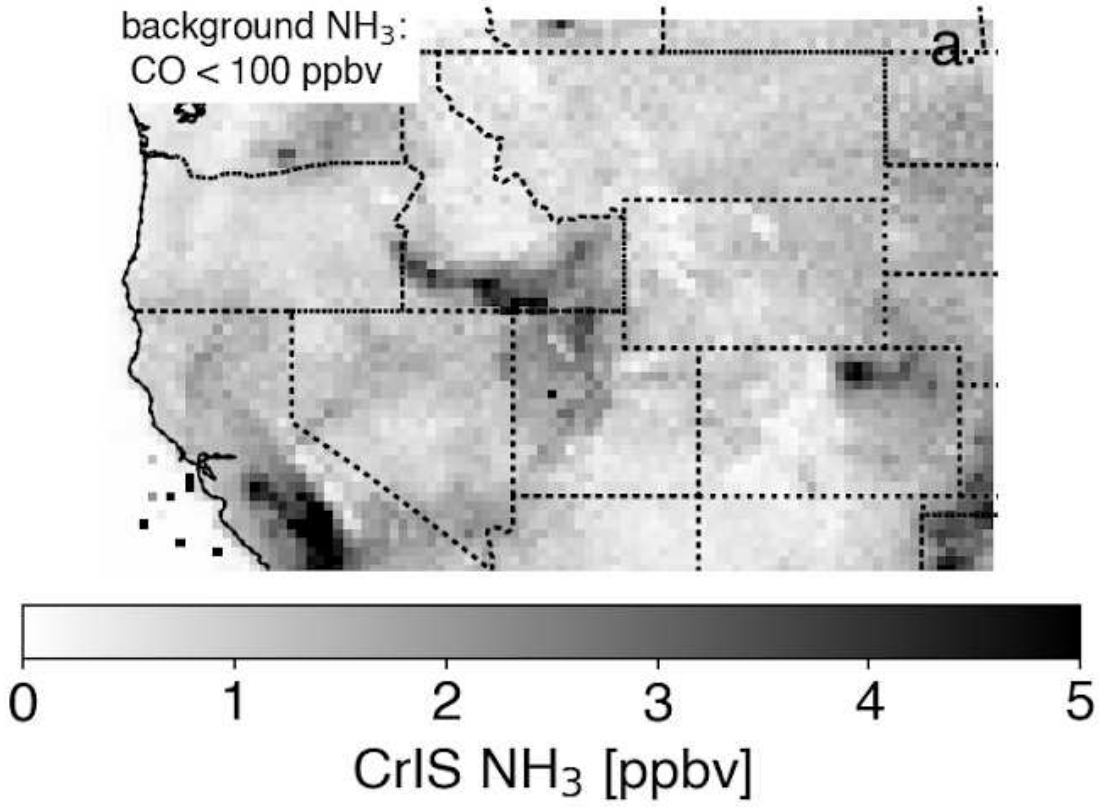

Figure A2.1: Estimated non-smoke background NH_3 from July 24 to September 13, 2018, calculated using retrievals where tropospheric CO < 100 ppbv, gridded at 0.25° × 0.25° for the entire domain, (-125°, -100°, 35°, 50°).

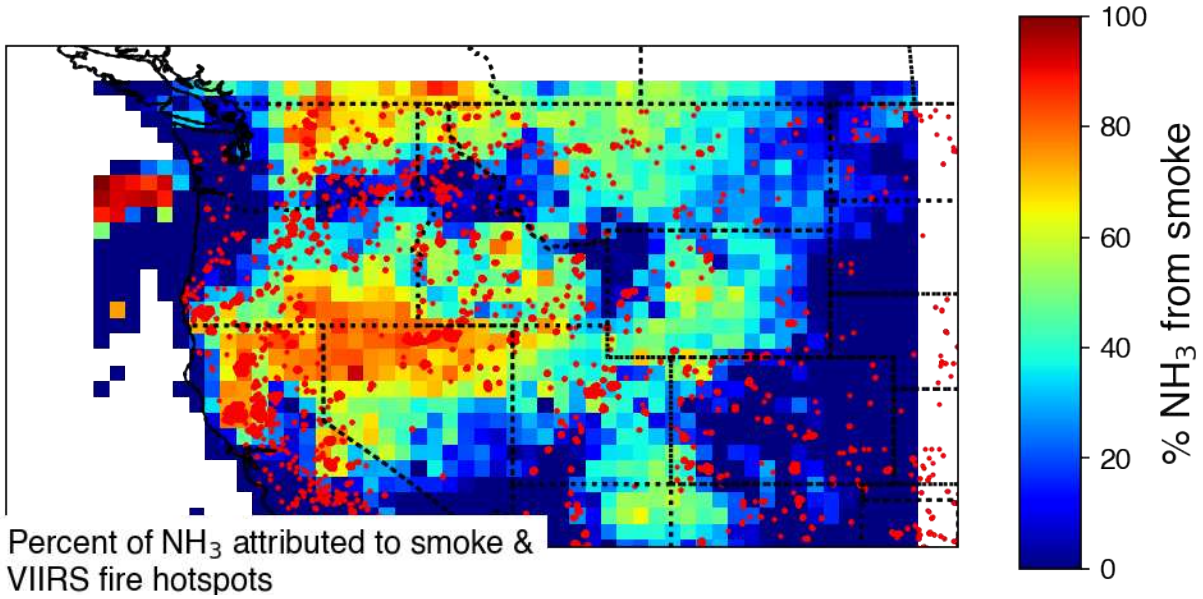

Figure A2.2: Estimate of the percent of NH_3 that can be attributed to smoke from CrIS observations from July 24, 2018 through September 13, 2018 following methods from Juncosa Calahorrano et al., 2021. Red circles denote VIIRS active fire detections.

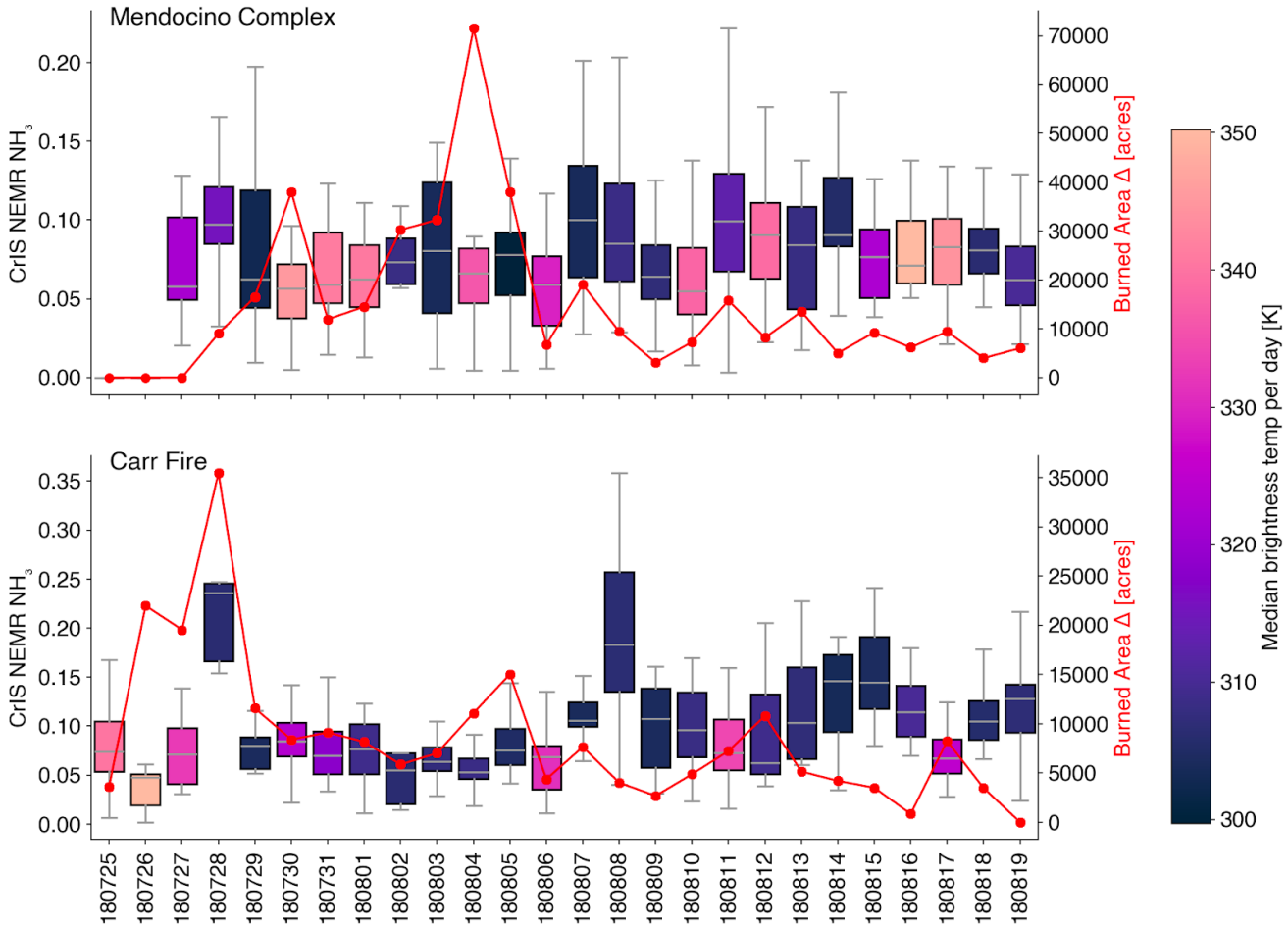

Figure A2.3: Distributions of CrIS NH_3 NEMR [ppbv/ppbv] values for Mendocino Complex fires (a; 38.24°N, 40.25°N, -123.9°W, -121.9°W) and Carr Fires (b; 40.6°N, 41.6°N; -122.6°W, -121.6°W) colored by the median VIIRS I-5 channel brightness temperature of fire pixel [K] value per day [using only high confidence retrievals]. The silver line represents the median value. The red lines represent the respective burned area difference from the previous day (Wikipedia, n.d.-a, n.d.-b)

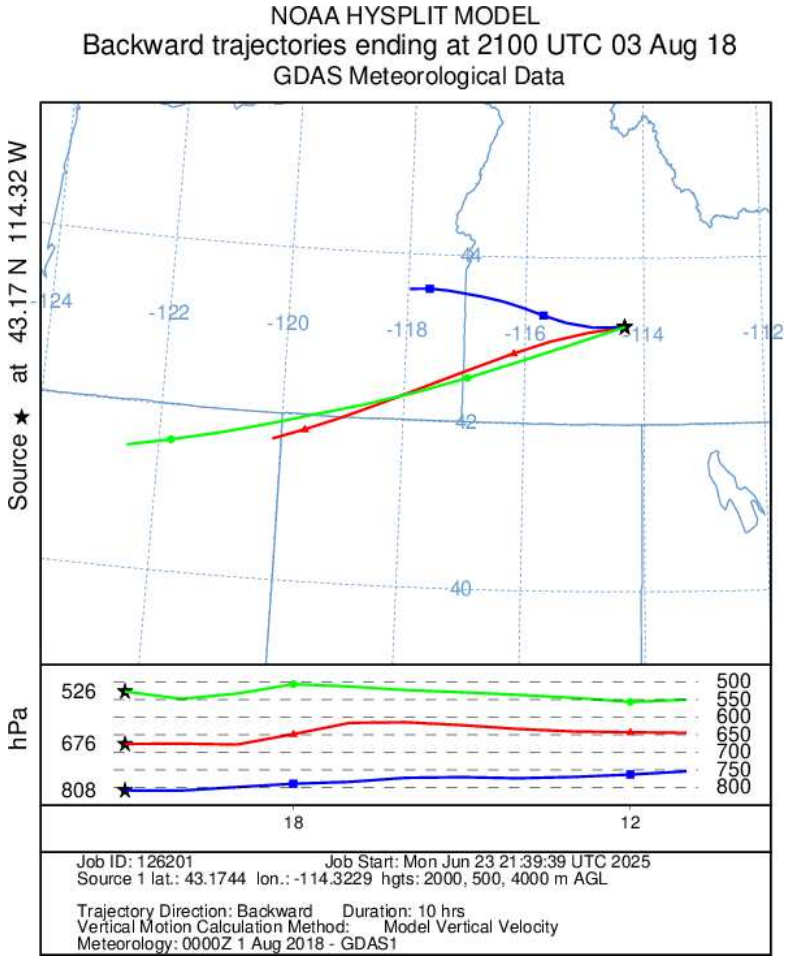

Figure A2.4: HYSPLIT back trajectory for August 3, 2018 initialized at three levels (A. F. Stein et al., 2015)

APPENDIX A3

SUPPLEMENTAL INFORMATION FOR CHAPTER 4

This section contains the supplemental information for Chapter 4. The three figures presented here show the mean NH_3 by land surface type for June, July and August. Colors in figures correspond to the land surface types in the map in Figure 4.1.

Section A3.1 presents an application of the machine learning-based CrIS product in four different wildfire smoke plumes over different terrain types. This section has been removed from the main chapter because the CrIS data the ML predictions were trained on contains a height-bias in the NH_3 product, making the NH_3 values an overestimate within concentrated smoke plumes. See Chapter 3 for more details about this height-bias and our attempts to correct it.

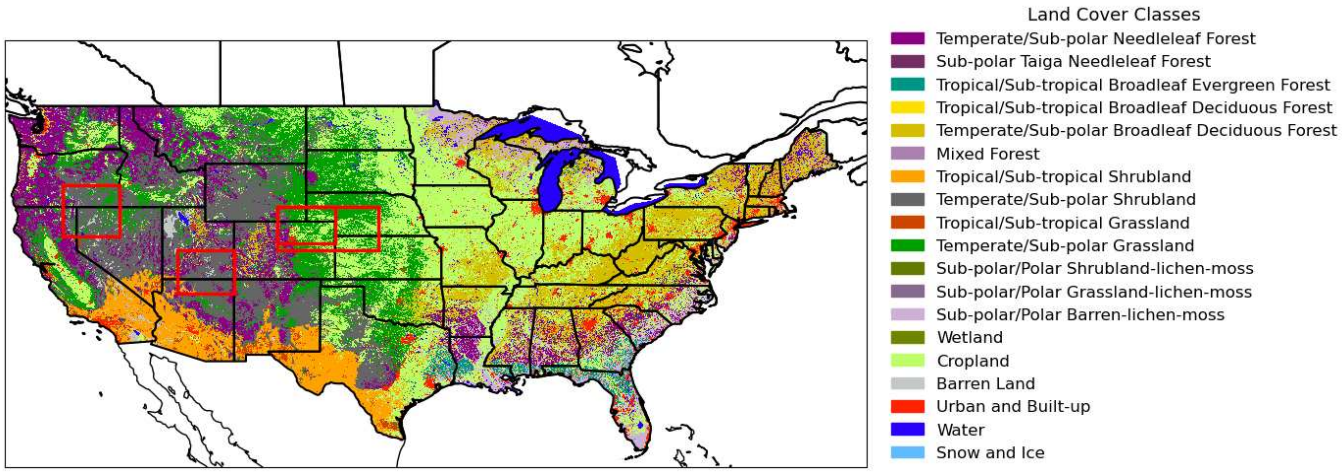

Figure A3.1: Map of USA colored by land cover class from LANDSAT NALCMS data (Commission for Environmental Cooperation (CEC), 2023). Red boxes correspond to extents in Figures A.5-4.7.

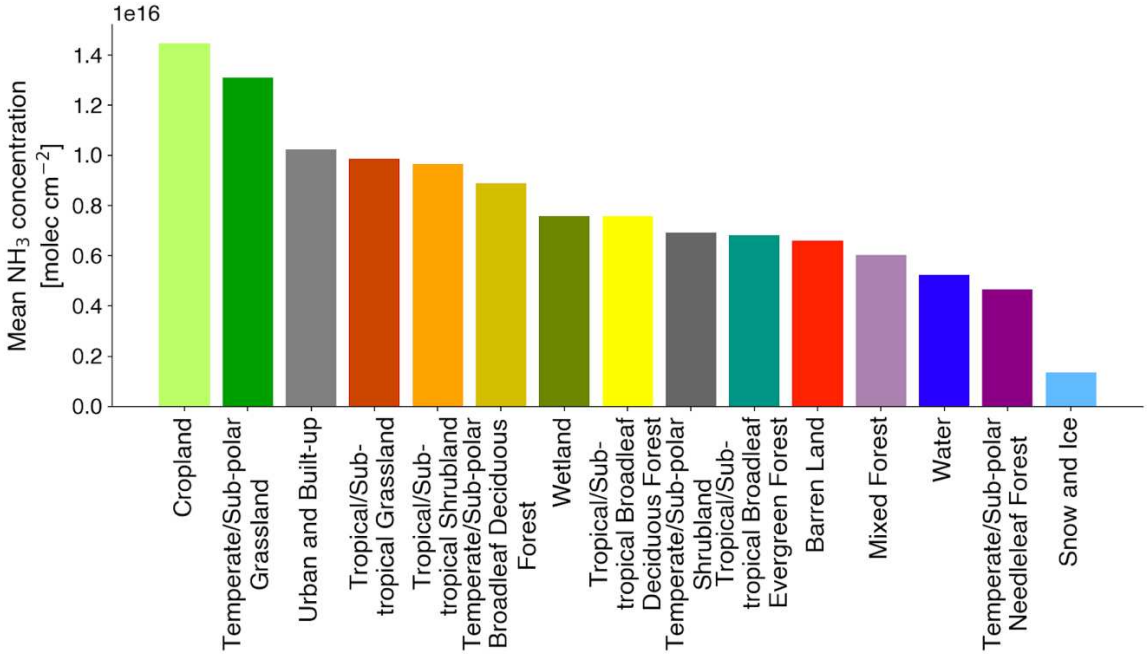

Figure A3.2: Mean NH_3 by land surface type for June. Colors correspond to the LANDSAT land surface classification map in Figure 4.1.

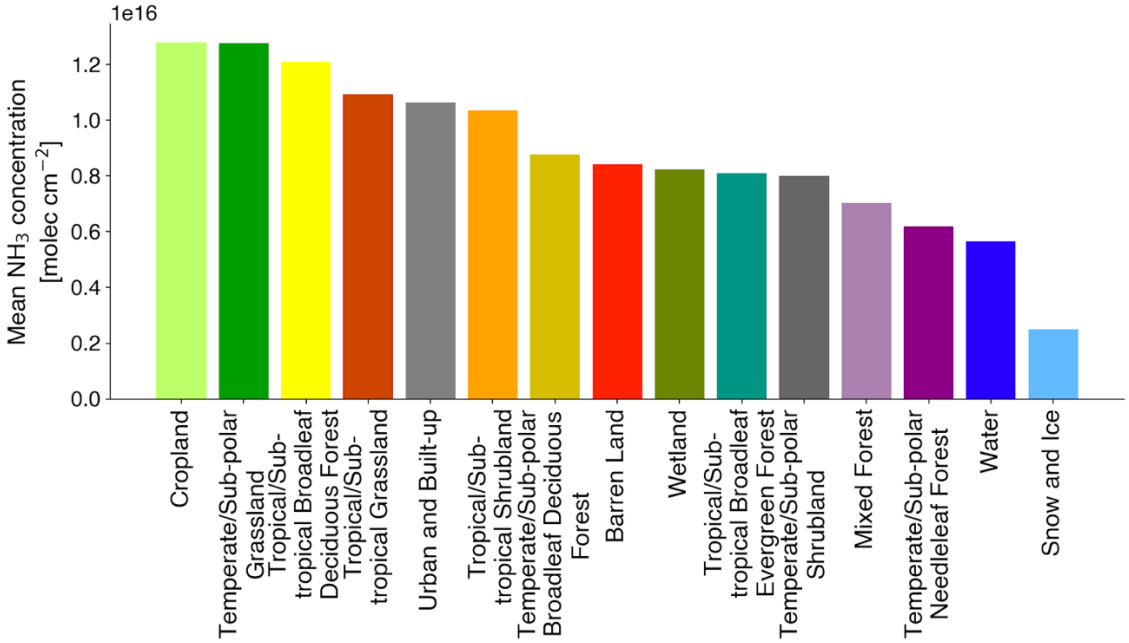

Figure A3.3: Mean NH_3 by land surface type for July.

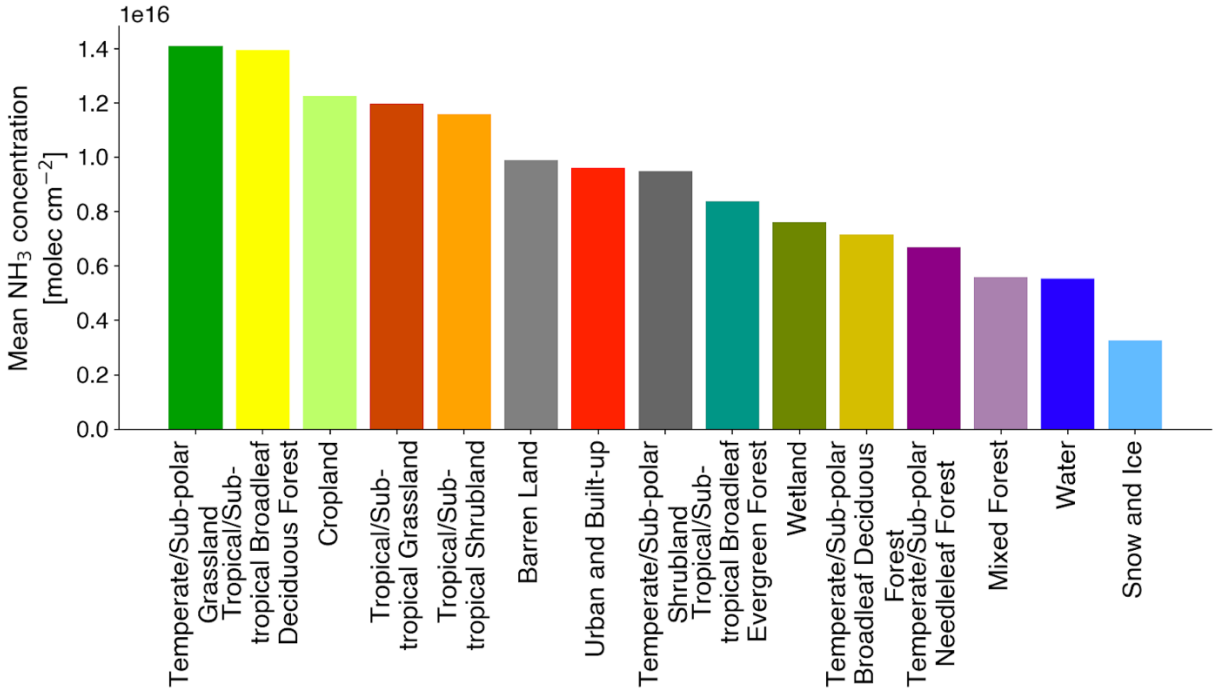

Figure A3.4: Mean NH_3 by land surface type for August.

4.3.2 Machine Learning-based Plume Evolution in Individual Smoke Plumes

The following section aims to use this ML-based data to evaluate the chemical evolution of NH_3 in four different wildfire smoke plumes in a similar way to how we used the OE-based data in Chapter 3. This section has been removed from the main text due to a height bias in the NH_3 data in smoke plumes that causes an overestimate of NH_3 values.

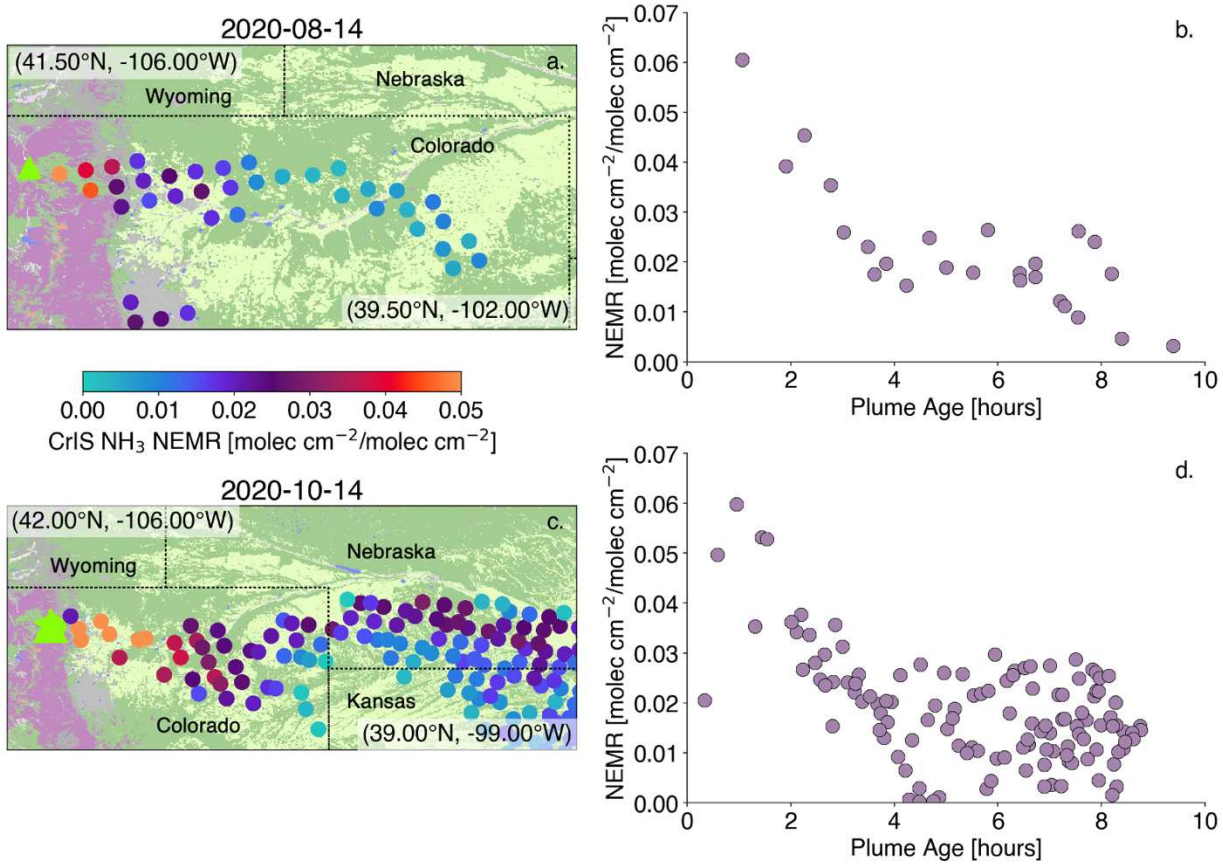

Figure A3.5: CrIS NH_3 smoke enhancements for the Cameron Peak Fire in Colorado. (a) Spatial distribution for the isolated Cameron Peak Fire plume on August 14, 2020, identified using retrievals where tropospheric column CO > 2e18 molecules cm^{-2}. CrIS footprints are colored by NH_3 NEMR [molecules cm^{-2}/molecules cm^{-2}]. VIIRS active fire detections are overlaid as green triangles, scaled by relative FRP. The underlying map shows LANDSAT-based land cover classifications (from Figure 4.1). (b) NH_3 NEMR values from panel (a) plotted as a function of estimated plume age. (c-d) Same as panels (a) and (b), respectively, but for October 14, 2020.

The Cameron Peak Fire provides a valuable case study for analyzing the CrIS ML-based observations of smoke-enhanced NH_3, as its prolonged duration and multiple days of well-defined plumes offer favorable conditions for satellite-based analysis. The Cameron Peak Fire is, to date, the largest wildfire in Colorado history. Cameron Peak began on August 13, 2020, and burned for 112 days until it reached full containment on December 2, 2020. The fire burned 208,663 acres through Arapaho and Roosevelt National forests in Larimer and Jackson Counties and through Rocky Mountain National Park. The fire exhibited rapid and sustained growth over its duration, driven by high temperatures, low humidity, and persistent high winds, with gusts

reaching up to 80 mph during September and October. These conditions, combined with the presence of extensive drought-stricken vegetation and thousands of acres of dense beetle-kill forest, created highly flammable fuel beds.

Figure A3.5 presents two days of burning of the Cameron Peak fire, August 14 and October 14, 2020. These days were both characterized by extensive fire growth and visible smoke plumes from visible satellite imagery (VIIRS). Both smoke plumes have been isolated using only "smoke-impacted" retrievals defined as retrievals where tropospheric column CO > 2e18 molecules cm^{-2}. We compare plumes from the same fire on two different days over similar time scales; however, stronger 700 hPa winds on October 14 resulted in more efficient plume transport and a greater spatial extent (Figure A3.5c), whereas weaker 700 hPa winds on August 14 kept the plume largely confined within Colorado (Figure A3.5a). August 14, 2020, marked the first full day of active burning for the Cameron Peak Fire and was characterized by rapid expansion, with the fire growing from ~ 2,200 to 4,600 acres by 19:00. Figure A3.5a shows the CrIS ML-based retrieval of the fire plume on this date, with each CrIS footprint colored by NH_3 NEMR.

A clear decrease in NH_3 NEMR with increasing distance from the fire centroid is evident in Figure A3.5a and is further quantified in Figure A3.5b, which illustrates NH_3 NEMR as a function of estimated plume age. Plume age was estimated here using wind speeds from NOAA meteorological reanalysis daily mean data at 700 hPa and the fire centroid location from VIIRS active fire hotspots following methodology described in Chapter 3. Figure A3.5b shows the NH_3 NEMR decreasing from ~0.061 to ~0.02 molecules cm^{-2}/molecules cm^{-2} in roughly 5 hours of aging (67% decrease) and from ~0.061 to ~0.005 molecules cm^{-2}/molecules cm^{-2} in roughly 10 hours of aging (97% decrease).

The interaction between plume transport and underlying land cover plays a critical role in shaping observed NH_3 enhancements and their interpretation through NEMR analysis. For plumes older than 5 hours, greater uncertainty arises due to evolving fire dynamics in time and more heterogeneous background NH_3 concentrations in agricultural regions. The plume in Figure A3.5a is overlaid on the LANDSAT-based land cover classification from Figure A3.1. The Cameron Peak Fire primarily burned through coniferous forest dominated by Ponderosa pine, Engelmann spruce, and mixed conifer species. As the plume dispersed, it advected over regions classified mainly as grasslands, croplands, and some shrublands. Notably, croplands (light green) are associated with higher and more variable background NH_3 levels—particularly in August (Figure 4.2), which underscores the importance of accounting for spatially varying background NH_3 in the NEMR calculation. In Figure A3.5b, increased variability in the relationship between NEMR and plume age is observed at ~5 hours of plume age, which may reflect both changing burning conditions and the transition of the plume over cropland areas.

Figures A3.4c and A3.4d similarly present the NH_3 NEMR analysis as a function of distance from the fire centroid and estimated plume age, respectively, for October 14, 2020. On this date, after 62 days of burning, the Cameron Peak Fire became the largest wildfire in Colorado history (Haggard & Paul, 2020). Rapid fire growth occurred throughout the day, with an overnight expansion of 30,000 acres, the most significant increase since early September (not shown), where the fire grew by 70,000 acres in 2 days. Easterly winds and rapid fire growth produced expansive smoke plumes visible across northern Colorado and in satellite imagery. As in Figure A3.5a, Figure A3.5c shows a pronounced decrease in NH_3 NEMR with increasing distance from the fire source. Figure A3.5d quantifies this decline as a function of approximate plume age. October 14 had substantially more “smoke-impacted” retrievals downwind than

August 14, reflecting generally smokier conditions and broader plume extent. Higher average 700 hPa wind speeds on October 14 facilitated more efficient eastward transport, contributing to a greater number of smoke-impacted retrievals eastward over eastern Colorado, Nebraska, and Kansas. While the NH_3 NEMR calculation method accounts for spatial variability in non-fire NH_3 emissions, the CrIS instrument lacks vertical profile information, with peak sensitivity in the lower to mid-troposphere. As a result, in regions with elevated surface NH_3 this NEMR calculation method can still induce some error. This limitation may contribute to the increased noise observed in Figure A3.5d beyond ~5 hours of aging. A similar, though less pronounced, pattern is seen in Figure A3.5b. On October 14, the NH_3 NEMR decreased from ~0.06 to ~0.015 molecules cm^{-2}/molecules cm^{-2} (~75% decrease) in about 5 hours of aging. This is a steeper decline than observed on August 14, consistent with the higher daily mean 700 hPa wind speed and more efficient smoke transport.

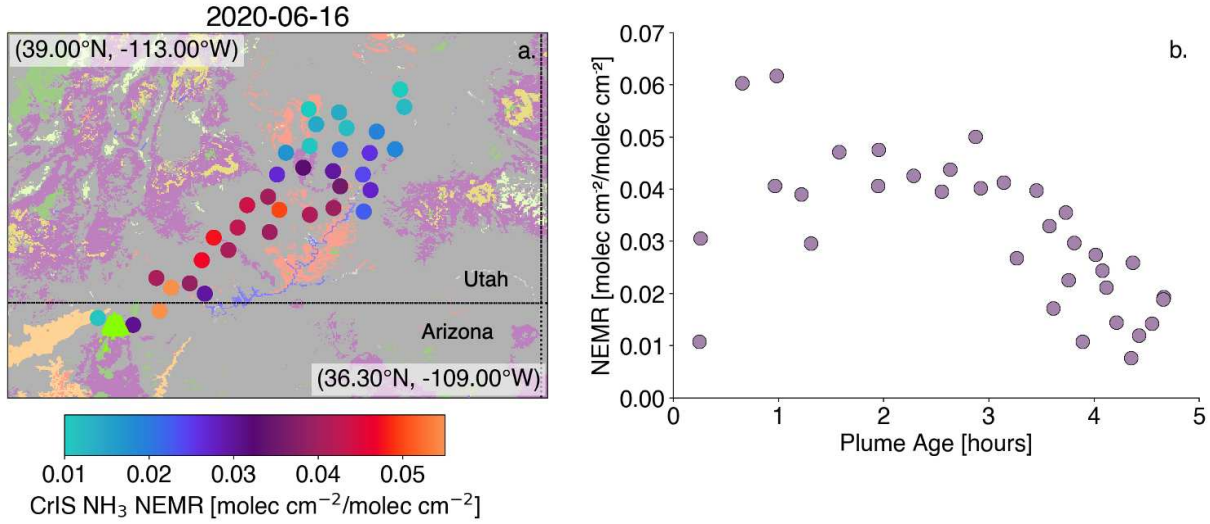

Figure A3.6: CrIS NH_3 smoke enhancements for the Mangum Fire in Arizona. (a) Spatial distribution for the isolated Mangum Fire plume on June 16, 2020, identified using retrievals where tropospheric column CO > 2e18 molecules cm^{-2}. CrIS footprints are colored by NH_3 NEMR [molecules cm^{-2}/molecules cm^{-2}]. VIIRS active fire detections are overlaid as green triangles, scaled by relative FRP. The underlying map shows LANDSAT-based land cover

classifications (from Figure A3.1). (b) NH_3 NEMR values from panel (a) plotted as a function of estimated plume age.

Applying the same analytical framework used for the above Cameron Peak Fire analysis, we investigate another fire event with a distinct fuel type. Figure A3.6 presents the CrIS ML-approach retrieval NH_3 NEMR for the Mangum Fire in Arizona on June 16, 2020. The Mangum fire started June 8 and reached containment on June 27, 2020, and burned through 71,450 acres. June 16th marked the most significant single-day growth with 17,824 acres burned, bringing the cumulative total to 47,481 acres by day's end (National Weather Service, Flagstaff AZ, 2020). Strong southwesterly winds and low relative humidity enabled extreme growth and hampered firefighting efforts and resulted in the clearly-defined, narrow plume heading to the northeast visible in satellite imagery (National Weather Service, Flagstaff AZ, 2020).

Figure A3.6a displays the spatial extent of the isolated smoke plume overlaid on the LANDSAT land cover classification map. A distinct decrease in NH_3 NEMR is observed with increasing distance from the fire centroid, consistent with prior cases. Figure A3.6b shows this decline as a function of estimated plume age, calculated using daily mean 700 hPa wind speeds (~14 m/s)—a higher value than observed for either Cameron Peak Fire case. Over approximately 5 hours of aging, NH_3 NEMR decreases from ~0.061 to ~0.003 molecules cm^{-2}/molecules cm^{-2} (~95% decrease).

The fire burned primarily through sagebrush grassland and pinyon-juniper shrubland. As the plume advected into Utah, it passed over regions dominated by shrubland, which, unlike croplands, are not associated with elevated background surface NH_3 (see Figure 4.2). According to the Smoke Emissions Reference Application (SERA; (University of Washington, n.d.); database (Burling et al., 2011; Gkatzelis et al., 2024; Lindaas, Pollack, Calahorrano, et al., 2021a; Selimovic et al., 2018)) shrubland fuels have high NH_3 emission factors (3.9 g NH_3/kg

fuel and 1.22 g NH_3/kg fuel for smoldering and flaming combustion, respectively), compared to coniferous forests (1.77 g NH_3/kg fuel and 0.89 g NH_3/kg fuel burned for smoldering and flaming combustion, respectively). The expected emission factors would be highest under smoldering combustion conditions, which consistently are associated with higher emissions factors of NH_3 relative to flaming combustion across all fuel types.

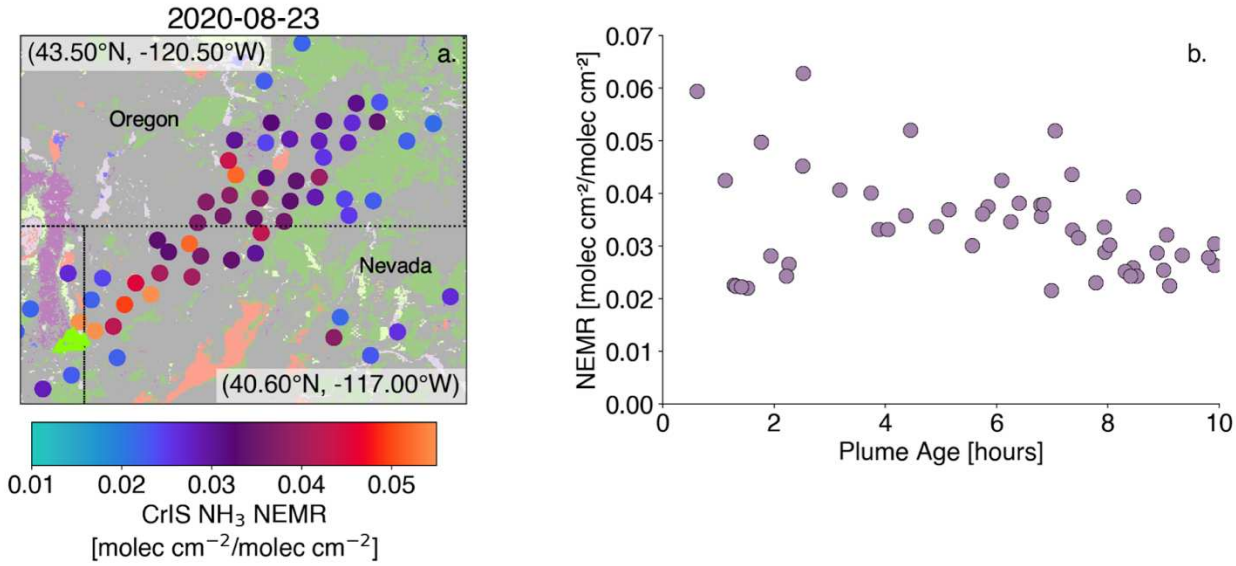

Figure A3.7: CrIS NH_3 smoke enhancements for the W-5 Cold Springs Fire in Northern California, part of the August 2020 California Lightning fires. (a) Spatial distribution for the isolated W-5 Cold Springs Fire plume on August 23, 2020, identified using retrievals where tropospheric column CO > 2e18 molecules cm^{-2} and where the NH_3 NEMR > 0.02. CrIS footprints are colored by NH_3 NEMR [molecules cm^{-2}/molecules cm^{-2}]. VIIRS active fire detections are overlaid as green triangles, scaled by relative FRP. The underlying map shows LANDSAT-based land cover classifications (from Figure 4.1). (b) NH_3 NEMR values from panel (a) plotted as a function of estimated plume age.

A similar analytical framework is applied to investigate a fresh plume from a third fire event in August 2020 with distinct burning conditions surrounded by more aged smoke. Figure A3.7 presents the CrIS-ML approach retrieval for NH_3 NEMR for the W-5 Cold Springs Fire in Northern California on August 23, 2020. This fire was a part of the August 2020 California Lightning Fires, which consisted of a series of 650 wildfires that ignited across Northern California in mid-August 2020 due to a siege of dry lightning from a rare set of massive summer

thunderstorms. The fires burned ~1,000,000 acres within a 2-3 week period (source) and created many large, well-defined smoke plumes visible from space.

Figure A3.7 presents one of the more defined plumes from the space perspective. Figure A3.7a displays the spatial extent of the isolated plume overlaid on the LANDSAT land cover classification map. Similar to the Cameron Peak and Mangum fires, the plume has been isolated using only retrievals where CO > 2e18 molecules cm^{-2}, however, the August 2020 California Lighting Fires were burning in many locations at this time, creating a lot of "background smoke" over the area, so this filtering did not successfully isolate the plume. There were many CrIS footprints surrounding this plume with very low NEMR values (ranging from ~0.0 to ~0.018 molecules cm^{-2}/molecules cm^{-2}), denoting aged smoke surrounding the fresher plume. We therefore apply additional filtering to use retrievals where the NH_3 NEMR > 0.018 molecules cm^{-2}/molecules cm^{-2} to ensure we are sampling the freshest smoke. Using this NEMR threshold does not impact the interpretation of the plume, as the most aged in-plume points for this domain are above this threshold. Some erroneous points were not filtered out, however, and appear as lower NEMR values in the lower right of Figure A3.7a. Focusing on the plume, a distinct decrease in NH_3 NEMR with increasing distance is observed in Figure A3.7a, consistent with the prior cases. Figure A3.7b shows this decline as a function of approximate plume age using the same analysis methods from Figures A3.5 and A3.6. Erroneous points not filtered out contribute to the noise in Figure A3.7b observed between 1.8 and 7 hours of aging. Over approximately 5 hours of aging, the NH_3 NEMR decreases from ~0.060 to ~0.032 molecules cm^{-2}/molecules cm^{-2} (~47% decrease).

We identified several distinct fire plumes from the 2020 wildfire season, representing a range of fuel types, from forests to shrublands, using space-based observations. These plumes

demonstrate that our ability to quantify and track the evolution of NH_3 enhancements within a plume using satellite measurements is influenced by the underlying land surface type, which determines the background NH_3 levels encountered by the plume. For the four cases analyzed, the reduction in smoke-enhanced NH_3 relative to CO ranges from 47% to 95% over approximately five hours. This loss appears to be relatively consistent across the plumes, potentially reflecting similarities in fire behavior during this time of day (~13:30 local time) and at the observed altitudes.

4.3.3 Near-Field Evolution of Fire Centroid from Machine Learning

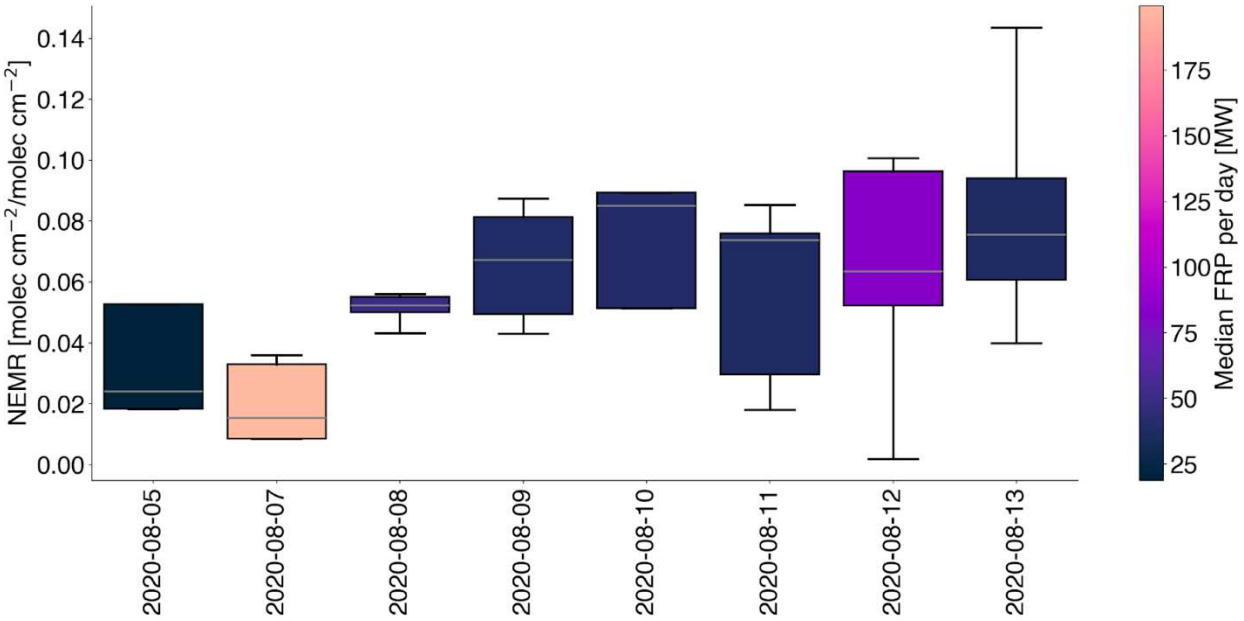

Figure A3.8: Distributions of CrIS NH_3 NEMR [molecules cm^{-2}/molecules cm^{-2}] for the Pine Gulch Fire in Colorado (38.3°N, 40.2°N, 109.5°W, 107.5°W) colored by the median VIIRS FRP value per day (using high and nominal confidence retrievals). The silver line denotes the median NEMR value.

To better understand the emission characteristics of the Pine Gulch Fire, we analyze the evolution of NH_3 enhancements near the fire source during its most active burning period. The Pine Gulch Fire in western Colorado ignited from a lightning strike on July 31, 2020, and burned

through 139,007 acres until it reached full containment on September 23, 2020. Pine Gulch was the largest wildfire in Colorado history for only seven weeks until it was surpassed by the Cameron Peak Fire on October 14, 2020 (Mesa County, n.d.; Wikipedia, n.d.-c). The fire was intensified by hot and dry weather, steep terrain and drought-stricken fuel sources, including grasslands, sagebrush, pinyon pine, and firs. Similarly to the Cameron Peak Fire, firefighting efforts were hampered by steep terrain and high wind speeds.

The temporal evolution of wildfire-driven NH_3 enhancements offers insight into the emission dynamics near the fire centroid during active burning. To characterize this near-source region, we define a rectangular domain extending from the fire centroid and oriented with the prevailing downwind direction of the smoke plumes. This domain is intended to capture freshly emitted smoke in close proximity to the fire centroid. There is some spread expected within this near-source region, but patterns exist within the distributions of NEMRs. Figure A3.8 illustrates the distributions of NH_3 NEMR values within this near-source box for the Pine Gulch Fire during the dates with the most extreme fire growth, August 5-13. The Pine Gulch fire grew from approximately 6,000 acres to over 69,000 acres during these 9 days (McKee, 2020).

Figure A3.8 shows higher values of median daily FRP are associated with the lower distributions of NH_3 NEMR. This pattern is particularly evident on August 7, 2020, where the NEMR distribution is the lowest and the FRP value reaches nearly 200 MW, the highest daily median FRP out of the 9 days. Extreme fire growth occurred on August 7th, enabled by low humidity, high temperatures, and strong winds, where the fire went from 11,846 acres on August 5th to over 20,000 acres by the evening of August 7th. Similarly, the NEMR distribution on August 12th reaches a global minimum (~0.01 molecules cm^{-2}/molecules cm^{-2}) and the daily median FRP is the 2nd highest in this sample (~80 MW). Other dates (August 8-11) experience

lower daily median FRP values (>70 MW) and display higher distributions of NH_3 NEMR values (medians range ~0.055-0.075 molecules cm^{-2}/molecules cm^{-2}). The overall trend of the NH_3 NEMR distributions is increasing with time while the trend of the distributions of FRP values (not shown) for the same period suggests a decrease in time, as the fire shifts from fresher, flaming combustion, to more aged smoldering combustion. These relationships qualitatively align with what is reported in Chapter 3, where a similar relationship exists between NH_3 NEMR distribution and FRP with time from the Mendocino Complex Fires and Carr Fire in Northern California. Chapter 3 reported days with the largest burned area difference in the Mendocino Complex fires were associated with some of the lowest NEMR distributions and highest median FRP values, a pattern also present in Figure A3.8.

In conclusion of this brief application section, we find:

1. ML-based CrIS data is used to analyze NH_3 enhancements in wildfire smoke plumes from 3 different fires between June and October 2020. We find NH_3 NEMRs decrease 47%-95% with roughly 5 hours of aging for these plumes. The interaction between plume transport and underlying land cover plays a critical role in shaping observed NH3 enhancements and their interpretation through NEMR analysis.

2. As western wildfires burn for days to weeks, over their lifecycle burning conditions often shift. We examine how the NH_3 NEMR over the Pine Gulch Fire in western Colorado shifts over the ~1.5 weeks of largest growth in August 2020. We find a relationship between the distribution of near-fire-centroid NEMRs and daily mean FRPs, where higher daily mean FRPs are associated with lower NH_3 NEMR values.